

UC San Diego

UC San Diego Electronic Theses and Dissertations

Title

Biomechanics of Articular Cartilage: Osteoarthritis and Tissue Engineering

Permalink

<https://escholarship.org/uc/item/86p1c8pp>

Author

Jafari, Somaye

Publication Date

2018

Peer reviewed|Thesis/dissertation

UNIVERSITY OF CALIFORNIA SAN DIEGO

**BIOMECHANICS OF ARTICULAR CARTILAGE:
OSTEOARTHRITIS AND TISSUE ENGINEERING**

A dissertation submitted in partial satisfaction of the
requirements for the degree Doctor of Philosophy

in

Engineering Sciences (Mechanical Engineering)

by

Somaye Jafari

Committee in charge:

Professor Shengqiang Cai, Chair
Professor Robert L.Sah, Co-Chair
Professor Renkun Chen
Professor Koichi Masuda
Professor Padmini Rangamani

2018

Copyright

Somaye Jafari, 2018

All rights reserved

The dissertation of Somaye Jafari is approved, and it is acceptable in quality and form for publication on microfilm and electronically:

Co-Chair

Chair

University of California San Diego

2018

DEDICATION

This thesis is dedicated to:

My God, my greatest teacher and supporter,

My dear husband, Hossein for all supports and helps,

My beloved kids, Ali and Hannah,

My kind brothers, Vahid, Hamid, Hamed, and Davood,

My mother for her support, encouragement, and constant love throughout my life,

And the memory of my father, Javad. I miss him every day, but I am glad to know he sees this process through to its completion, offering the support to make it possible, as well as plenty of friendly encouragement.

EPIGRAPH

چپ میخور و راست میخور و بیچ کو

ای رفتہ بہ چو کان تھنا، بچون کو

اوداند و اوداند و اوداند و او

کانکس کہ تورا اکنندہ در تک و پ

God is a polo player, and I am the ball I suppose,

Whichever way I'm hit, I can't oppose,

Since he is the power and glory,

He knows, he knows and he knows...

Khayyam 1131, Nishapur, Iran

TABLE OF CONTENTS

SIGNATURE PAGE	iii
DEDICATION	iv
EPIGRAPH	v
LIST OF FIGURES	ix
LIST OF TABLES	xi
ACKNOWLEDGMENTS	xiv
VITA	xvii
ABSTRACT OF THE DISSERTATION	xviii
CHAPTER 1: INTRODUCTION	1
1.1 Background and Outline of the Thesis.....	1
1.2 Synovial Joint, Composition and, Structure.....	4
1.2.1 Synovial joint.....	4
1.2.2 Uncalcified articular cartilage, structure, and composition	4
1.2.3 Calcified cartilage	5
1.2.4 Subchondral bone plate.....	6
1.2.5 Tidemark and cement line interfaces	6
1.3 Cartilage Degeneration Due to Osteoarthritis and Trauma.....	7
1.3.1 Cartilage degeneration due to osteoarthritis	7
1.3.2 Cartilage degeneration due to trauma	8
1.4 Articular Cartilage and Subchondral Plate 3-D Visualization Methods	10
1.5 Articular Cartilage as a Poroelastic Material	11
1.5.1 Stress relaxation in unconfined compression.....	12
1.5.2 Creep in confined compression.....	12
1.6 Reference.....	24
CHAPTER 2: 3-D HISTOPATHOLOGICAL VISUALIZATION OF VASCULAR CANALS IN OSTEOARTHRITIS	29
2.1 Abstract	29
2.2 Introduction	31
2.3 Materials and Methods.....	33

2.3.1	Study design.....	33
2.3.2	Sample preparation and imaging	34
2.3.3	Image processing	34
2.3.4	Assumptions.....	35
2.3.5	Classification of the canals	36
2.3.6	Determination of coordinate of vascular canal center	36
2.3.7	Determination of canal diameter.....	38
2.3.8	Determination of canal spacing	38
2.3.9	Canal diameter and spacing statistics	39
2.4	Results	40
2.4.1	Appearance and classifications of canals.....	40
2.4.2	Coordinate and diameter of the canal	41
2.4.3	Canal spacing.....	42
2.4.4	“Small”, “mean” and “large” diameters and spacing.....	42
2.5	Discussion	43
2.6	Acknowledgment	47
2.7	Reference.....	78

CHAPTER 3: EFFECTS OF OPEN VASCULAR CANALS ON THE BIOMECHANICS OF THE DEEP ZONE OF ARTICULAR CARTILAGE. 80

3.1	Abstract	80
3.2	Introduction	82
3.3	Materials and Methods.....	86
3.3.1	Study design.....	86
3.3.2	Assumptions.....	86
3.3.3	Schematics of confined compression test	87
3.3.4	Material properties	88
3.3.5	Initial and boundary conditions	89
3.3.6	Equations used in ABAQUS.....	91
3.3.7	Define the contact between cartilage and bone in ABAQUS.....	92
3.4	Results	93
3.4.1	Effect of diameter of vascular canal on the biomechanics of articular cartilage	93

3.4.2	Effect of the spacing between vascular canals on the biomechanics of articular cartilage	94
3.4.3	Temporal variation of the total vertical fluid flux	95
3.5	Discussion	96
3.6	Acknowledgment	101
3.7	Reference.....	119
CHAPTER 4: BENDING OF A POROELASTIC SHEET: IMPLICATIONS FOR CARTILAGE SHAPING AND GRAFTING.....		124
4.1	Abstract	124
4.2	Introduction	126
4.3	Materials and Methods.....	129
4.3.1	Results.....	133
4.3.2	Instantaneous bending ($t=0+$)	133
4.3.3	Moment relaxation with maintaining the cylindrical contour ($0+ < t < \infty$)	135
4.3.4	Instantaneous unloading ($t' = 0 +$)	138
4.3.5	Creep recovery ($0+ < t' \leq \infty$).....	139
4.4	Discussion	142
4.5	Acknowledgment	145
4.6	References	157
CHAPTER 5: CONCLUSION.....		161

LIST OF FIGURES

Figure 1.1: Representation of a synovial joint including cartilage degeneration.	13
Figure 1.2: Structure of a synovial joint.	14
Figure 1.3: Zone variation of cartilage components as well as compressive modulus (H_A and hydraulic permeability)	15
Figure 1.4: Comparison of composition and cellular organization of normal and osteoarthritis (OA) adult human cartilage.....	16
Figure 1.5: Canal invasion through the synovial joint.....	17
Figure 1.6: Histological findings of the subchondral plate with HE staining.....	18
Figure 1.7: Process of osteochondral grafting.	19
Figure 1.8: Stress relaxation and creep test.	20
Figure 2.1: Schematics of the assumptions to simplify the interface of cartilage and bone.	48
Figure 2.2: Classification of canals according to their bony cap and the degree of penetration.....	49
Figure 2.3: Method of determination of vascular canals center coordinate and diameter.	50
Figure 2.4: Schematics representing the method of determination of small, mean and large spacing between the canals.	51
Figure 2.5: Method of simplification of the canal for three different categories of canal appearance.....	52
Figure 2.6: Representation of the open canals in the horizontal section for NL sample PPG414-002n and OA sample WDB414.....	53
Figure 3.1: Two schematics representing types of simplified vascular channels.....	102
Figure 3.2: Various structural assumptions made through the joint in order to simulate the problem.	103
Figure 3.3: Schematics of confined compression test done on OA osteochondral join.	104
Figure 3.4: Schematics of the axisymmetric model in ABAQUS.	105

Figure 3.5: effect of diameter change on the special variation of pore pressure along r direction at $z= 4\mu\text{m}$	106
Figure 3.6: Effect of diameter change on the special variation of max and min principal strains (ϵ_{max} and ϵ_{min}) along r direction at $z= 4\mu\text{m}$	107
Figure 3.7: Effect of spacing on the special variation of pore pressure (P) and min principal stress applied on a solid phase (σ_{min}) along r direction at $z= 4\mu\text{m}$	108
Figure 3.8: Temporal variation of vertical flux along the free surface of cartilage at the top of the vascular canal (red line on the schematics).	109
Figure 3.9: Contour plot of the effect of change of diameter on fluid pressure and max principal strain.	110
Figure 3.10: Contour plot of the effect of change of spacing on fluid pressure and min principal strain.	111
Figure 4.1: Schematics of stress relaxation and creep of a poroelastic sheet submerged in a solvent.	146
Figure 4.2: Temporal and spatial variation of the vertical flux of the solvent in a poroelastic sheet	147
Figure 4.3: Temporal and spatial variation of the chemical potential of solvent in the poroelastic sheet.....	148
Figure 4.4: Temporal and spatial variation of ϵ_x in the poroelastic sheet.	149
Figure 4.5: Temporal and spatial variation of ϵ_y in the poroelastic sheet.....	150
Figure 4.6: Temporal and spatial variation of the change of solvent concentration in the poroelastic sheet.....	151
Figure 4.7: Temporal and spatial variation of σ_x in the poroelastic sheet.....	152
Figure 4.8: Temporal variation of moment and curvature of the neutral plane of the poroelastic sheet.....	153

LIST OF TABLES

Table 1.1: Definition of different parts of the synovial Joint.....	21
Table 1.2: Geometrical and material parameters and definitions.....	22
Table 1.3: Characteristic time, τ based on the definition obtained by different studies...23	
Table 2.1: Clinical details of normal (NL) and osteoarthritis (OA) samples analyzed in this study.....	54
Table 2.2: Sample IDs and the google paths of NL and OA samples	55
Table 2.3: Classification of vascular canals according to their caps and the degree of penetration.....	56
Table 2.4: Quantification of vascular canal types in NL samples	57
Table 2.5: Quantification of vascular canal types in OA samples.....	58
Table 2.6: Quantification of vascular canals according to two simplified closed and open canals in NL samples	59
Table 2.7: Quantification of vascular canals according to two simplified closed and open canals in OA samples.....	60
Table 2.8: Quantification of number of closed and open vascular canals per 1mm^2 of the NL sample.....	61
Table 2.9: Quantification of the number of closed and open vascular canals per 1mm^2 of the OA sample.....	62
Table 2.10: Representation of the classification of the open canals, their coordinates, diameter, and total numbers for each NL sample	63
Table 2.11: Representation of the classification of the open canals, their coordinates, diameter, and total numbers for each OA sample.....	64
Table 2.12: Determination of three small, mean and large diameters of open vascular canals in NL samples. The calculation was based on the first 10 and 25%, mean and last 10 and 25 % of the diameters for each sample	65
Table 2.13: Determination of three small, mean and large diameters of open vascular canals in OA samples.....	66

Table 2.14: Diameter (small, mean, large) measurements based on Means of means from Table 2.10 and 2.11. Data are Mean±SD.....	67
Table 2.15: Number of channels used for spacing analysis for each sample	68
Table 2.16: Color-coded spacing measurements between NL vascular channels..	69
Table 2.17: Color-coded spacing measurements between OA vascular channels.....	70
Table 2.18: Distribution of vascular canal diameter pairings based on the small, mean and large size of diameter in NL samples.....	71
Table 2.19: Distribution of vascular canal diameter pairings based on the small, mean and large size of diameter in OA samples	72
Table 2.20: Spacing measurement based on lower and upper 10% values of nearest neighbors for individual samples, overall samples, and mean of means in NL samples..	73
Table 2.21: Spacing measurement based on lower and upper 10% values of nearest neighbors for individual samples, overall samples, and mean of means in OA samples .	74
Table 2.22: Spacing values to be used for simulations based on means of means from Tables 2.18 and 2.19	75
Table 2.23: Values for parameters of interest for diameters and spacing in NL samples.	76
Table 2.24: Values for parameters of interest for diameters and spacing in OA samples	77
Table 3.1: Representation of critical magnitudes of Mechanical criteria affecting cell viability.	112
Table 3.2: Different group of geometries for simulation.....	113
Table 3.3: Material properties of articular cartilage for simulation.....	114
Table 3.4: Material property inputs in ABAQUS based on data from Table 3.3	115
Table 3.5: Half of diameter and spacing and the corresponded characteristic times based on half sizes.....	116
Table 3.6: Three-time courses of the simulation	117
Table 3.7: Variables to define the equations of the problem in ABAQUS.....	118

Table 4.1: Constant parameters of the poroelastic sheet and the solvent applied in this study.....	154
Table 4.2: Process of mechanical loading and unloading of a poroelastic sheet submerged in a solvent including conditions, knowns, and unknowns.....	155
Table 4.3: Normalized symbols in terms of the constant parameters.....	156

ACKNOWLEDGMENTS

I would like to thank all those who gave me the possibility to complete this thesis.

My sincere gratitude to my advisor Prof. Shengqiang Cai and co-adviser Prof. Robert L.Sah for the continuous support of my PhD study and related research, for their patience, motivation, and immense knowledge. Their guidance helped me in all the time of research and writing of this thesis. I could not have imagined having better mentors for my PhD study.

I would like to thank my thesis committee members: Prof. Renkun Chen, Prof. Koichi Masuda, and Prof. Padmini Rangamani, for their insightful comments and encouragement. Thanks to Prof. Joanna M. McKittrick for being my committee member during my senate exam and giving advices and insightful comments before my dissertation.

Besides my dissertation advisors, there are many I need to thank for directing and helping me to obtain a Ph.D. My special thanks to Dr. Albert C. Chen for all his support. He was as a great teacher for me in the cartilage biomechanics area. He helped me accelerate various study projects to the end. This dissertation would not have been possible without his intellectual contribution.

Thanks to the staff of the Mechanical & Aerospace Engineering Department for helping me through the administrative process. I especially would like to thank Joana Halnez for her continual efforts in making the entire process go smoothly and for having an answer for every question I gave her.

I am very thankful to the entire Soft Material group, for making a friendly and supportive environment. I am very thankful to Xudong Liang for all guidance he did. I would also like to thank my other lab mates that include Zhijian Wang, Chi Hyung Ahn, Yue Zheng, Zhaoqiang Song, Yang Wang, and Qiguang He.

To the entire Cartilage Tissue Engineering Lab, I am especially grateful for all guidance and advice. Thanks to Van Wong for his organizations and supportive help.

Thanks to the contributors of my studies. Thanks to Dr. William D Bugbee , Matthew K Wang, Alborz Jelvani and Nasim Eshragh Nia. Thanks to Neil Chang for being as a teacher for me in the area of 3D histopathological imaging. He always tried his best to answer my questions even after his graduation.

Thanks to My other fellow graduate students of CTE lab. Thanks to Felix Hsu for helping and answering my questions. Thanks to Jason P. Caffrey for the advice in his many areas of expertise, especially MATLAB programming. Thanks to Rebecca Drace, Erica Gacasan, Sydnee Hyman, Ismael Munoz, and Aimee Raleigh.

My special gratitude goes to my husband, children, parents, and brothers for their unconditional love and support during every step in my life through the years.

Chapter 2 is being prepared for submission to JBiomechanics. The dissertation author is the co-author and thanks author Dr. Neil Chang and other co-authors Jason P. Caffrey, Matthew K Wang, Alborz Jelvani, Nasim Eshragh Nia, Van W Wong, Dr. William D Bugbee, Dr. Albert C. Chen, Prof. Shengqiang Cai, Dr. Koichi Masuda and Prof. Robert L. Sah for their contributions.

Chapter 3 is being prepared for submission to *JBiomechanics*. The dissertation author is the primary investigator and thanks co-authors Dr. Albert C. Chen, Prof. Shengqiang Cai, and Prof. Robert L. Sah.

Chapter 4 is being prepared for submission to *JBiomechanics*. The dissertation author is the primary investigator and thanks co-authors Prof. Shengqiang Cai and Prof. Robert L. Sah.

VITA

- 2008 B.S., Mechanical Engineering
University of Yazd,
Isfahan University of Technology, Iran
- 2011-2013 M.S., Mechanical Engineering
University of California San Diego
- 2014-2018 Ph.D., Engineering Sciences (Mechanical Engineering)
University of California San Diego

Journal Articles

Hu, J., S. Jafari, Y. Han, A. J. Grodzinsky, S. Cai and M. Guo (2017). "Size- and speed-dependent mechanical behavior in living mammalian cytoplasm." Proc Natl Acad Sci U S A **114**(36): 9529-9534.

ABSTRACT OF THE DISSERTATION

BIOMECHANICS OF ARTICULAR CARTILAGE:
OSTEOARTHRITIS AND TISSUE ENGINEERING

By

Somaye Jafari

Doctor of Philosophy in Engineering Sciences (Mechanical Engineering)

University of California San Diego, 2018

Professor Shengqiang Cai Chair

Professor Robert L. Sah, Co-Chair

In the normal adult synovial articular joint, articular cartilage (AC) as an avascular tissue, is attached to the calcified cartilage (CC). Calcified cartilage is a thin tissue layer, separated from AC by tidemark (TM), and subchondral bone (ScB) by cement line (CL). Calcified cartilage and subchondral bone plate together form subchondral plate (ScP). ScP merges into a porous network called trabecular bone (TB). Cartilage degeneration and loss

may be caused by different diseases such as osteoarthritis (OA) or trauma. There are many vascular canals embedded within subchondral plate which carry various types of cells and blood vessels. In OA, the structure of the cartilage and subchondral plate underneath, the geometry of the canals as well as the spacing between them may change. The effect of ScP changes on the biomechanics of articular cartilage is unclear. Furthermore, after cartilage is lost due to OA or trauma, current efforts are underway to resurface the joint. While methods for bending cartilage have been introduced, the mechanics of such bending are unclear. Thus, this dissertation aims to (1) analyze images of normal (NL) and OA samples in order to clarify the structure of the ScP vascular canals, (2) investigate the effect of such vascular canals on the biomechanics of the deep zone of cartilage and (3) evaluate the mechanics of articular cartilage sheet as a poroelastic material under pure bending.

In (1) Digital Volumetric Images were used to obtain 2-D cross sections of cartilage and subchondral plate of 5 OA and 6 NL samples. Vascular canal were found as 12 different types associated with the presence/absence of a cap and the degree of canal penetration of the ScP and AC. In NL samples, there were no invaded open canal through tidemark, while from 37 open canals were found in OA samples, 11 of which penetrated the tidemark. The diameter of canals was smaller ($27\ \mu\text{m}$) in NL samples than ($67\ \mu\text{m}$) in OA samples. The spacing between the open canals was smaller ($135\ \mu\text{m}$) in OA samples than ($809\ \mu\text{m}$) in NL.

In (2), using three small, mean and large diameters and spacing, a confined compression test was analyzed with ABAQUS software to analyze the effect of change of size and spacing of those canals on the spatial and temporal distribution of fluid pressure as well as strain-stress through articular cartilage. With the increase of the diameters of the

canals and decrease of the spacing between them, fluid pressure (pore pressure) within cartilage, especially at the deep zone, decays. Furthermore, with the increase of the spacing between canals, the mechanical response of the sample becomes close to that of NL sample

In (3), poroelastic theory was applied to evaluate the biomechanics of cartilage under pure bending. Under pure bending, axial strain varies linearly between compression and tension (concave to convex). In the bent state, the bending moment relaxes as strain redistributes axially, and fluid is exuded from the compressed region and imbibed in the stretched region. At equilibrium, the bending moment and strain stabilize as fluid ceases to flow. After the bending is suddenly released, creep recovery occurs as fluid flow into and out of the sheet reverses and also redistributes within the sheet.

These studies developed models to describe the biomechanics of articular cartilage as a poroelastic material when subjected to various loading and boundary conditions. The prediction of loading effects on the deep zone of OA cartilage may be involved in progressive cartilage degeneration. The understanding of time-dependent mechanical behavior of poroelastic sheet under bending may help develop loading strategies to achieve an appropriately contoured shape before implantation

CHAPTER 1:

INTRODUCTION

1.1 Background and Outline of the Thesis

Synovial joints are the most common and most movable types of joint in a mammal's body [44]. The ends of the bone are covered by articular cartilage (AC) (**Fig. 1.1a**). Articular cartilage is a smooth tissue at the ends of bones where they come together to form joints. It provides lubrication and stability to the joint [44]. Cartilage damage may be caused by different diseases such as OA (**Fig. 1.1b,c**) or injury (**Fig. 1.1c,d**)[9]. In these cases the joint may undergo degeneration or, cartilage loss happens. Localized defects in cartilage or bone underneath can cause pain, swelling, and dysfunction. Regarding OA, there is a variety of Articular Cartilage (AC) degeneration especially at the interface of cartilage and subchondral bone (ScB) [29, 47, 51, 53, 57]. To investigate cartilage remodeling and its potential implications under OA or injury, it is necessary to study the effect of these degenerations on the mechanics of AC under different loading boundary conditions.

The overall motivation of this study was to investigate the structure and composition of AC, some geometrical quantifications based on degeneration occurred at the synovial joint interface due to OA progression. The poroelastic behavior of AC under various loading boundary conditions as a study of the effect of different degenerating issues

on Mechanics of AC. The objectives of the studies in the dissertation are: (1) develop 3-D data set and image processing to precisely visualize the interface structure, (2) use these methods to classify interface structure according to its grade as well as degree of degeneration, (3) obtain geometrical dimensions as well as distributions of canals at interface, (4) simplify the interface geometry (Chapter 2), (5) effects of the presence of canals at interface on mechanics of AC (Chapter 3), and finally (6) biomechanics of AC as a poroelastic material under bending as a results of implantation of lost AC.

Chapter 1 begins with an introduction to AC, structure, and composition of each part with the focus on the interface of AC-ScB as an area of interest. Uncalcified cartilage (UC), Calcified cartilage (CC), ScB and the interfaces between each layer are distinguished. Degeneration of AC is discussed as a result of OA progression and the presence of Vascular Canals (VCs) due to this progression. Strategies for visualizing 3-D structures of the synovial joints are discussed. Regarding material properties of AC based on its composition and structure, AC is defined as a poroelastic material following related mechanical and diffusion laws. Based on the poroelastic behavior, standard mechanical tests applied on AC are discussed.

Chapter 2 begins with the introduction of interface with the presence of vascular canals and the degree of their penetrations. Method of obtaining vertical and horizontal planes of the joint from DataViewer is presented. Different classifications of the canals according to their penetration through tidemark (TM) and cap are discussed. Based on the classifications of the canals, two simplified canal geometries are obtained. Finally, Coordinates of each canal, diameter, and spacing between canals are determined.

Chapter 3 continues to analyze the effect of geometrical dimensions and spacing between the canals (determined in Chapter 2) on the biomechanics of articular cartilage (AC). Some of the backgrounds regarding the presence of canals underneath AC are represented. Using software ABAQUS, the effect of the canals and their distributions on the biomechanics of AC as a poroelastic material is investigated based on the stress/strain and fluid pressure distributions for Three-time courses: short, intermediate and long times. The effect of time on fluid depressurization as well as stress and deformation within the solid phase of AC is discussed according to the canal size and spacing distribution.

Finally, chapter 4 introduces AC as a poroelastic material and explains some clinical backgrounds of cartilage implantation and various studies done on the poroelastic material. An analytical study is conducted to analyze the effect of bending of AC on the stress/strain distribution, fluid pressure and water concentration over two-time courses, stress relaxation and creep recovery.

Chapter 5 summarizes the major findings of the studies and implications for research of mechanical effects of osteoarthritis, and injury on AC and interface.

1.2 Synovial Joint, Composition and, Structure

1.2.1 Synovial joint

Synovial joints are the most common and movable types of joint in a mammal's body [44]. End of the bones is covered by articular cartilage (AC) (**Table 1.1**), 1-3mm thick [12]. In the normal adult synovial joint, AC is divided into two distinct zones, uncalcified cartilage (UC) and calcified cartilage (CC). Based on the structure of cartilage in different zones, UC is subdivided into three different zones, superficial zone (SZ), 10-20% , middle zone (MZ), 40-60% and deep zone (DZ), 20-50% overall tissue [18, 24, 27, 29, 37, 48] (**Fig. 1.2a**).

The uncalcified articular cartilage is separated from the subchondral plate (ScP) by an undulated shaped border called tidemark (TM). TM protects UC from progressive mineralization [15, 48, 52]. At the interface where we are interested to study, ScP is composed of two tissue layers, calcified cartilage (CC), ~100 μm thick, and "corticalized" subchondral bone plate (ScBP), ~300 μm thick (**Fig. 1.2b**). CC is separated from ScBP by cement line (CL). Finally, underneath ScBP there is trabecular bone, a spongy bony including marrows and vascular canals. Together, the synovial joint unit bears the load of the articulating joint, with a low friction, lubricated cartilage surface. Thus, a harder physical structure of the subchondral bone withstands compressive stresses, and the CC and ScBP transfer the load between the cartilage and bone [15, 48, 52].

1.2.2 Uncalcified articular cartilage, structure, and composition

AC covers the ends of synovial joints and provides lubrication and stability to the joints. The superficial zone comprises the upper 10-20% of the tissue. Within this area, collagen fibers are densely packed and oriented parallel to the cartilage surface [39]. The

matrix has a relatively low proteoglycan content, as well as low permeability [45, 38] and chondrocytes are almost flat and parallel to the surface.

The middle zone occupies approximately 40-60% of the overall tissue thickness. Collagen fibers type II are randomly oriented in this area and chondrocytes are more spherical [28]. Proteoglycans content reaches its maximum in the middle zone [59].

The deep zone comprises 20-50% of the total thickness. There are large collagen fibers in this area perpendicular to the cartilage surface and anchored in the underlying calcified cartilage [45]. In this zone, proteoglycans and cell densities are much lower than in the middle zone [56, 59]. Cells in the deep zone often group together in a columnar organization. They are slightly elongated and oriented in the direction of collagen fibers, perpendicular to the articular surface [20]. A summary of the density of each quantity within uncalcified cartilage is represented in **Fig 1.3**.

1.2.3 Calcified cartilage

Calcified cartilage is a mineralized articular cartilage tissue providing attachment of the uncalcified cartilage to bone [47]. In this zone, collagen fibrils are aligned vertically and cross the tidemark. The mineralization of the calcified layer is from calcium hydroxyapatite. The thickness of calcified cartilage is about 6-8% of the overall thickness [29, 46, 49]. This mineralized zone is less stiff than the subchondral bone and transfers the load from uncalcified cartilage to the bone [40].

1.2.4 Subchondral bone plate

The subchondral bone plate is a cotrified bone layer, with a thickness of approximately 0.1-3.0 mm [10, 42]. It is comprised of mostly Type I collagen and 60-70% mineral salts such as hydroxyapatite. The matrix is arranged in a series of sheets, also called lamellae, which in the plate mostly run tangential to the calcified cartilage. The mechanical function of the subchondral bone plate is to provide support for the overlying articular cartilage [19].

1.2.5 Tidemark and cement line interfaces

Tidemark (TM) is an undulated boundary separating the uncalcified articular cartilage from calcified cartilage [48]. It can be clearly distinguished as the mineralization front at the end of the deep zone of the articular cartilage, with a metachromatic line in most staining techniques of the tissue. In the normal tissue, only one tidemark is observed across the whole synovial joint. Collagen fibrils in this area cross the TM and run between the uncalcified and calcified cartilage [14].

Cement line (CL) separates the calcified cartilage from the subchondral bone plate. Unlike the tidemark, CL is undulated very strongly, to the point which it forms interdigitating fingers between the calcified cartilage and bone, possibly fortifying the physical bond between the two layers. The “fingers” of the interdigitating bone are often the result of the previously described vascular canals, with their closed bony caps poking up into the calcified cartilage, creating a bumpy cement line surface [35].

1.3 Cartilage Degeneration Due to Osteoarthritis and Trauma

1.3.1 Cartilage degeneration due to osteoarthritis

Osteoarthritis (OA) is the most common degeneration in articular cartilage (AC) which results in disability in the adult population. In addition to articular cartilage, it has been observed that other parts of the joints including calcified cartilage and subchondral bone are affected by OA [22]. Development of osteoarthritis results in cartilage fibrillation and degradation, chondrocyte clustering, cartilage calcification parallel to tidemark duplication (**Fig. 1.4**) [21, 22]. One of the important outcomes of OA is vascular canal invasion from the subchondral plate through articular cartilage which is visualized at the interface of articular cartilage and calcified cartilage (**Fig. 1.4**, OA joint). Effect of the presence of these canals at the AC-CC interface on the biomechanics of articular cartilage is of the interest of one of the studies of this thesis.

Invasion of the vascular canals through different layers of the synovial joint has occurred. Clark visualized various cartilage layers using scanning electron microscopy (SEM) techniques [14, 15]. It was observed that the subchondral bone and calcified cartilage were penetrated by some vascular canals (VC) with the smallest size of 10-30 μm and carrying blood vessels (**Fig. 1.5a**). These canals were found in two types: open and closed (**Fig. 1.5b**). In the open type, the canal was open at its top end. In the closed form, the canals did not open into the calcified cartilage and were capped by lamellar bone. However, there was no correlation found between the frequency of these two types and the joint degeneration.

Canal invasion through the tidemark and its frequency appear to be a common feature in the human osteoarthritis (OA) joints [7, 29, 51, 57, 58, 60]. The density of the

invaded canals was higher in the OA group with respect to the normal (NL) group [7, 23, 29, 36, 60]. Shibakawa [53] observed that the density of invaded canals through calcified cartilage and below tidemark for both NL and OA groups are similar while this invasion above tidemark is predominant in OA groups (**Fig 1.6**). The density of the canal invasion depends not only on aging [47] but also on load bearing area [30, 53], as well as some genetic factors. Independent of diagnostic groups, vascular density in the non-calcified cartilage increases with increasing degree of cartilage severity [36, 60].

Invasion of vascular canals through the tidemark may help trigger cartilage degeneration and mechanics especially at the deep zone [63]. On the one hand, the vascular canal invasion was observed to be accompanied by increase in the cartilage calcification associated with the tidemark duplication at the deep zone, not only in OA groups [7, 21, 22, 25, 33, 34, 62] but also in high aged normal ones [7]. The duplication of tidemark and resultant thinning of the articular cartilage [33] would be predicted to increase the mechanical stresses in the deep zones of the cartilage [23]. On the other hand, the presence of vascular canals invaded through articular cartilage may result in some exchanges of fluid and soluble products within cartilage which may affect the activities of the cartilage components [23, 30].

1.3.2 Cartilage degeneration due to trauma

Defected articular cartilage has a limited capacity of self-healing. Arthroscopic studies have shown that the defected cartilage area of patients knee ranges from <1 to 4 cm² [16, 26]. Since articular cartilage is an avascular tissue, if the defected area is not treated, it will generally increase in size [13, 31, 61]. There are various surgical treatments

for defected cartilage according to the defect size: microfracture [55], autologous chondrocyte implantation and its variations [8], and osteochondral grafting using native or synthetic cartilage [6, 17].

In order to do the osteochondral graft, the defected part of the cartilage (**Fig. 7a**) along with the interface is taken off from the surface of the subchondral bone (**Fig. 7b**). A native or synthetic tissue is bent around the bone (**Fig. 7c, d**) and a calcification interface is formed between cartilage and bone (**Fig. 7. e**)

1.4 Articular Cartilage and Subchondral Plate 3-D Visualization Methods

Recently, to visualize the 3-D microstructure of synovial joint, a serial sectioning and reconstruction imaging method called Digital Volumetric Imaging (DVI) is developed [32]. Samples with the dimension of up to 4mm are fixed, stained, and then embedded in a standard EM resin. After curing, samples are mounted on the DVI instrument. There is a rotary diamond blade microtome for cutting, an epifluorescence microscope, and various and imaging hardware. Samples are sectioned automatically, and the cut sections are then discarded. After each cut, the sample face of the specimen is digitally imaged by epifluorescence. Multiple spectral images expressing distinct fluorophores are collected at each plane. The digital serial images are assembled as a three-dimensional data set. This method of imaging provides about 0.9mm resolution to visualize biological features in detail in 3-D [32]. In the present study, DVI is used to characterize the three-dimensional structure of the vascular canals passing through subchondral bone, calcified cartilage and articular cartilage of the NL and OA samples [50]

1.5 Articular Cartilage as a Poroelastic Material

Poroelasticity is used to describe the interaction between viscous fluid flow and solid deformation within a porous medium [5]. The linear theory of poroelasticity, first developed by Biot (1941), is used to evaluate the time-dependent behavior in poroelastic material, incorporating Hook's law for deformation of the porous matrix and Darcy's law for the fluid flow through the porous matrix [3-5]. One important application of poroelasticity is to model articular cartilage. About 75% of cartilage volume is water [41]; then articular cartilage is considered as a biphasic tissue [1, 43] and most of the load applied on cartilage will be carried with water. It has been shown that the poroelasticity and biphasic theories are equivalent [54].

Articular cartilage often experiences compressive loading. Compression of articular cartilage is often accompanied by the fluid flow through the porous solid matrix. Fluid redistribution within the cartilage results in a time-dependent deformation in cartilage. As fluid pressure decays over time, more load is carried by the solid matrix, giving rise to stress relaxation and creep behaviors [43]. There is an important factor called characteristic time, τ which describes the kinetic process either in stress relaxation or creep. In poroelasticity, τ is material property and geometry dependent. Material properties (**Table 1.2**) of cartilage are known. However, the geometry and BCs in order to determine the characteristic time is obtained based on the given problem. Characteristic time is defined based on the characteristic length, L along which the diffusion happens and the mechanical properties of the poroelastic material (**Table 1.3**).

1.5.1 Stress relaxation in unconfined compression

Fig. 1.8a,b represent the schematics and graph of stress relaxation test. Articular cartilage is saturated in water and is placed between two impermeable plates [43]. A controlled displacement is applied on the top plate for a short time (**Fig. 1.8b**, red line, point A) compared to the characteristic time and held fixed until equilibrium time. Applied force reaches the maximum during the short time and then decays (stress relaxation) until equilibrium is reached [2]. In this test, the characteristic time is defined based on the diameter of the cartilage cylinder because diffusion is mainly along the radial direction.

1.5.2 Creep in confined compression

Fig. 1.8c,d represents the schematics and graph of creep test. Saturated articular cartilage is confined inside an impermeable chamber and compressed by a porous plate with a constant load [43]. A load is applied nearly instantaneously (point A of the green line) and held a constant. When the load is held constant, creep occurs within the cartilage until the displacement reaches equilibrium state [2]. In this test, the characteristic time is defined based on the height of the cartilage cylinder because diffusion occurs along the vertical direction.

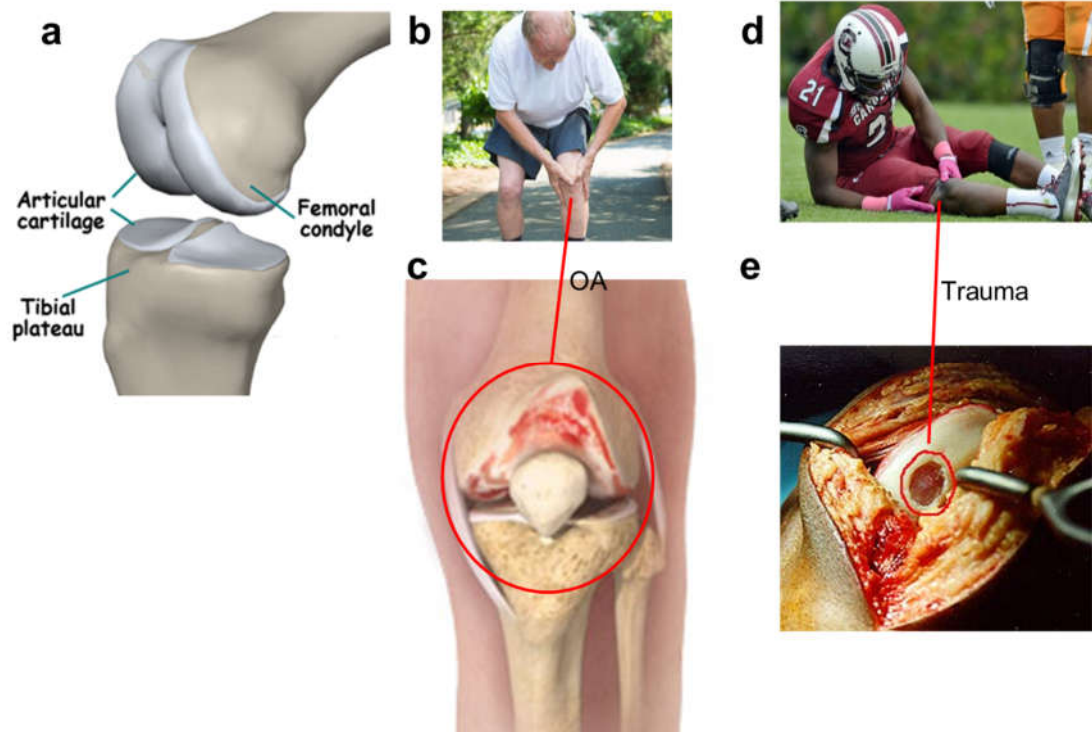


Figure 1.1: Representation of a synovial joint including cartilage degeneration. a) Schematics of a synovial joint in macro scale representing the bone ends and articular cartilage. b, c) Degradation of articular cartilage due to osteoarthritis (OA). d, e) Cartilage loss due to trauma.

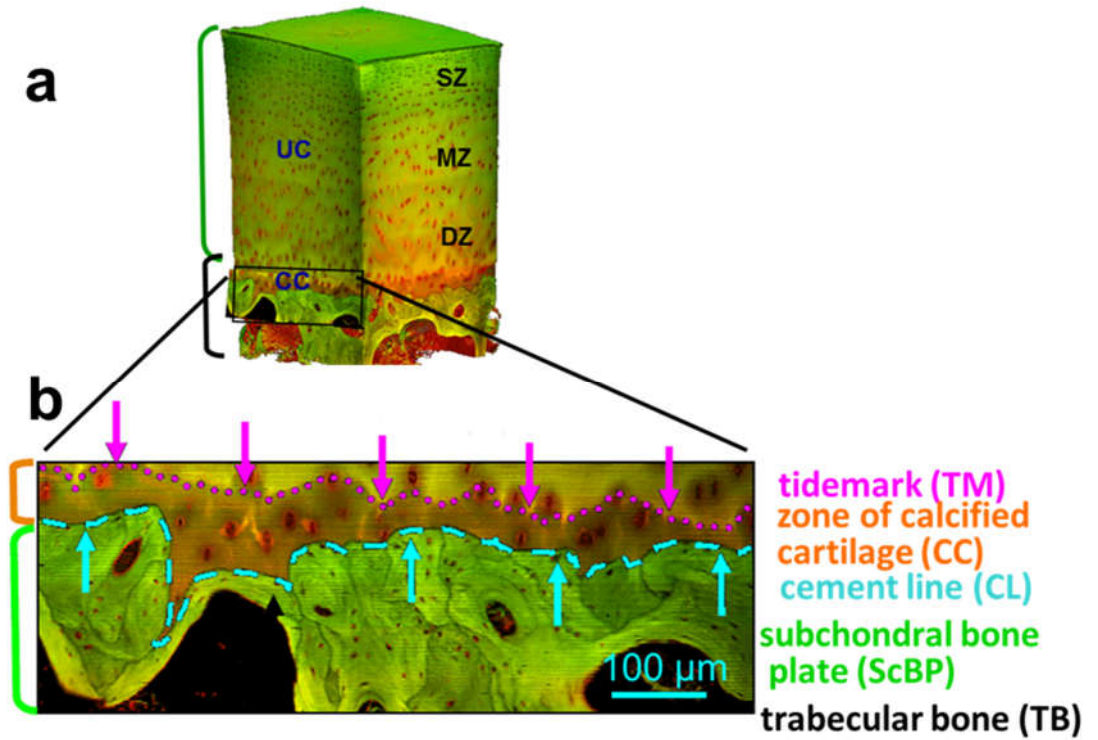


Figure 1.2: Structure of a synovial joint. a) Macroscale structure of the articular cartilage including uncalcified cartilage (UC) and calcified cartilage (CC). Uncalcified cartilage is subdivided into three different zones: superficial zone (SZ), middle zone (MZ) and deep zone (DZ). b) The interface of articular cartilage and subchondral bone (ScB)

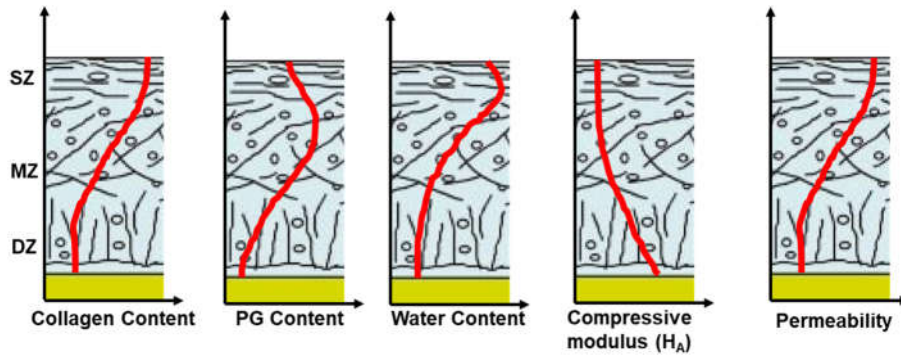


Figure 1.3: Zone variation of cartilage components as well as compressive modulus (H_A and hydraulic permeability). Articular cartilage zone includes superficial zone (SZ), middle zone (MZ) and deep zone (DZ)

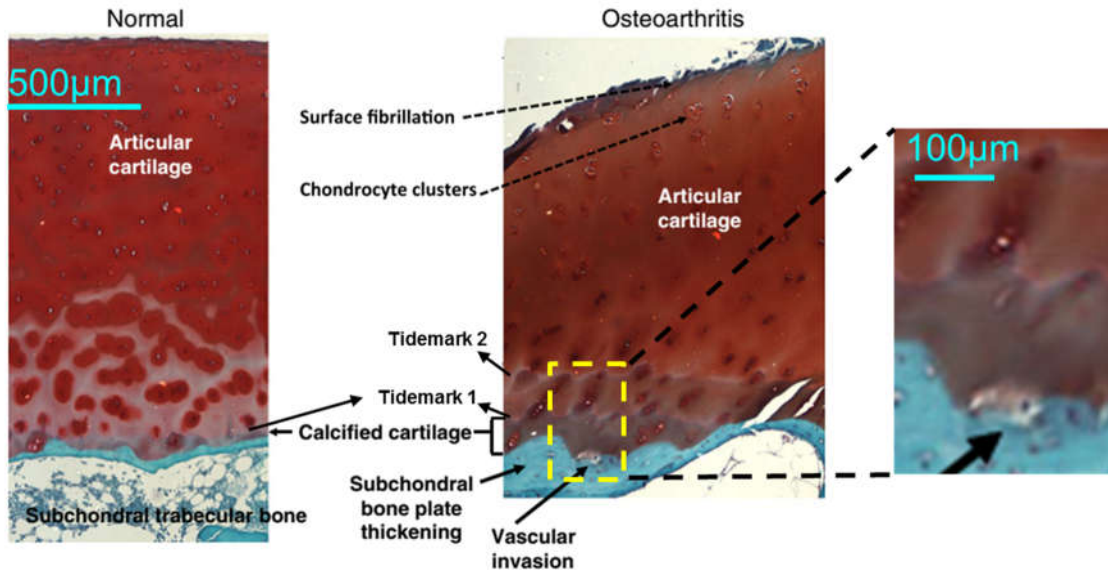


Figure 1.4: Comparison of composition and cellular organization of normal and osteoarthritis (OA) adult human cartilage. In OA joint, cartilage fibrillation, chondrocyte clusters, tidemark advancement and vascular canal invasion is observed [21].

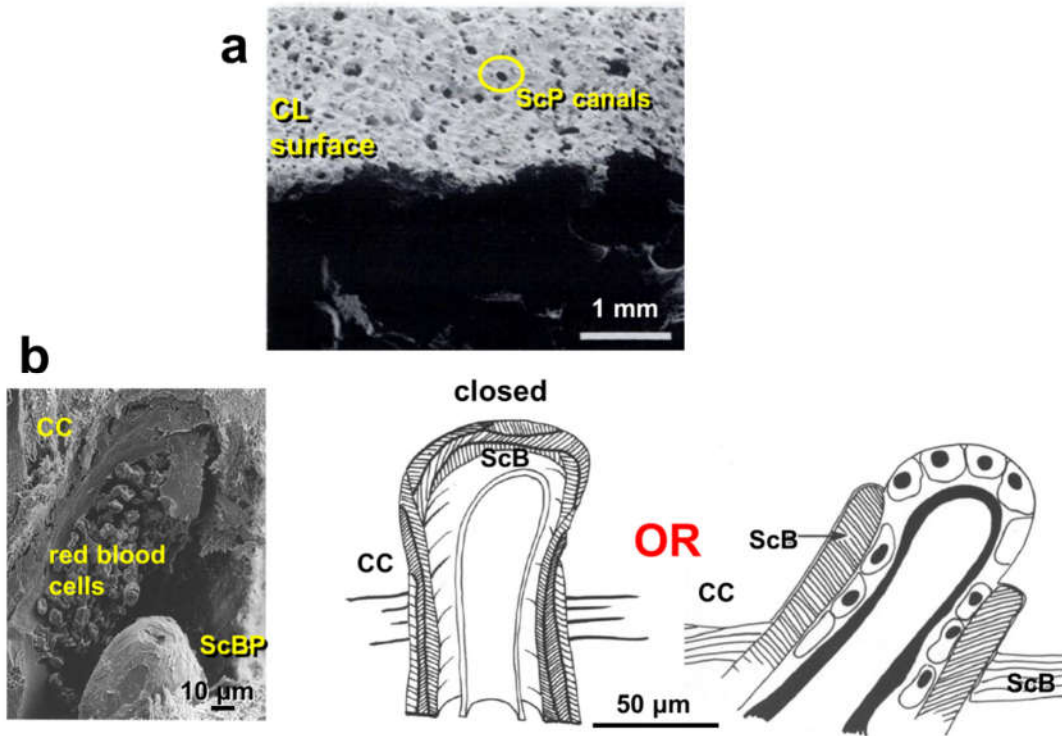


Figure 1.5: Canal invasion through the synovial joint. a) Vascular canals passing cement line (CL) and invaded through calcified cartilage. b) Vascular canals contain red cells and could be either closed or open according to the ending cap on the top [14, 15].

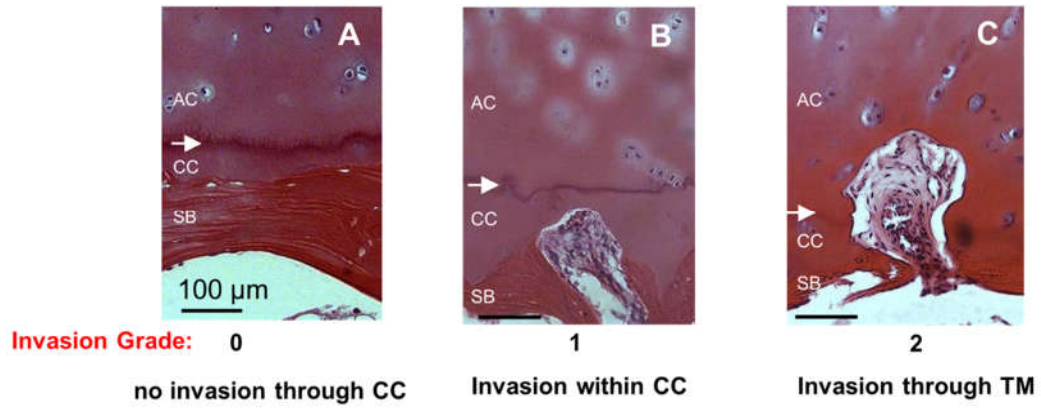


Figure 1.6: Histological findings of the subchondral plate with HE staining. Grade 0: subchondral plate with no invasion of the vascular canal. Grade 1: vascular canal invasion is limited within the calcified cartilage, Grade 2: vascular canal invasion into the articular cartilage beyond the tidemark. Arrow: tidemark (TM), articular cartilage (AC), calcified cartilage (CC), subchondral bone (SB).

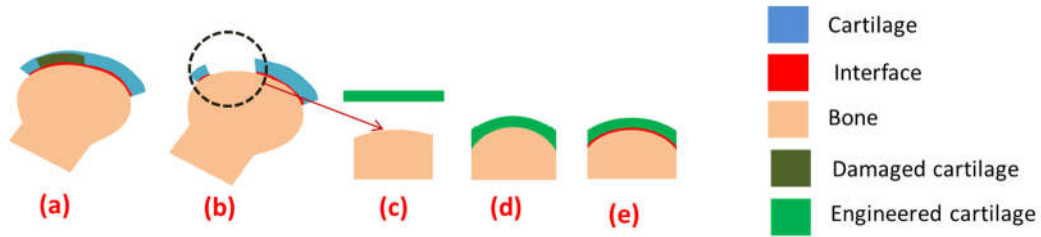


Figure 1.7: Process of osteochondral grafting. a) Defected cartilage is located through the synovial joint, b) defected cartilage is taken off along with the interface, c) A native or synthetic cartilage is used to replace the defected cartilage, d) Cartilage graft is bent around the bone, and e) a calcified interfaced is made between cartilage and bone.

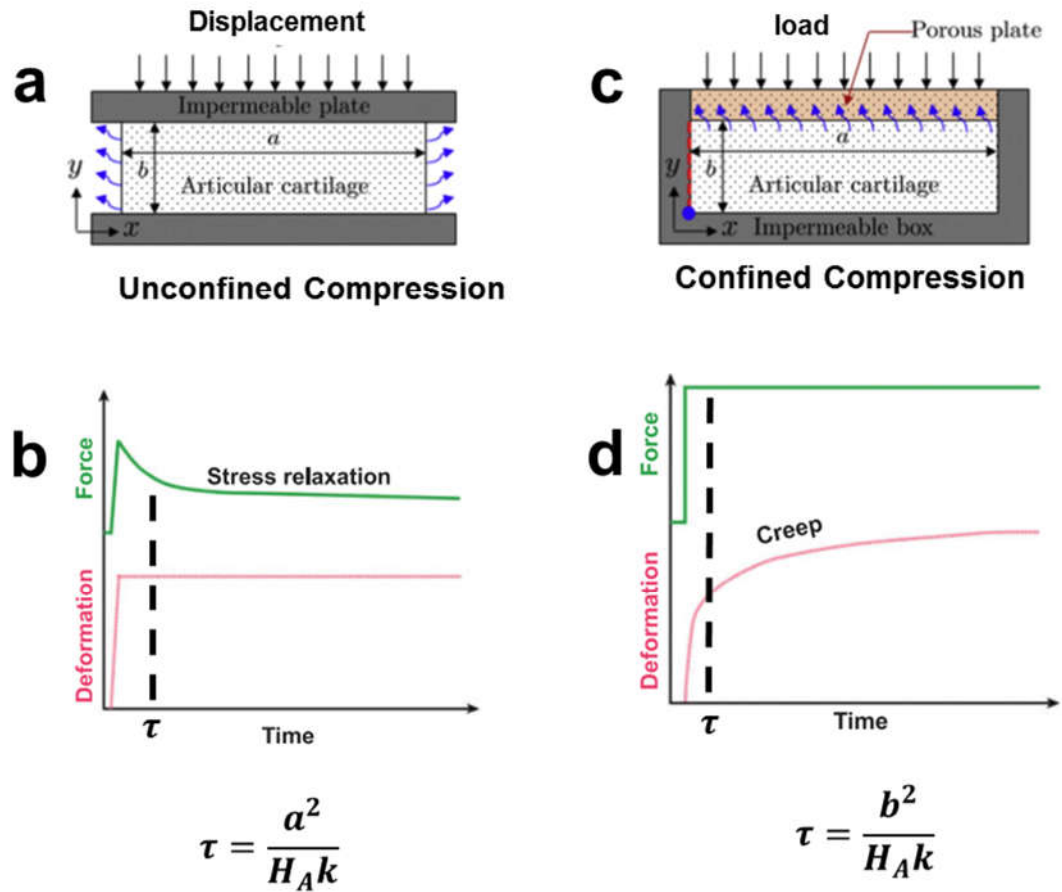


Figure 1.8: Stress relaxation and creep test. a) Schematics of unconfined compression test resulting in stress relaxation. b) Graph of stress relaxation test by controlling the displacement applied on the top surface of cartilage. c) Schematics of confined compression test resulting in creep. d) Graph of creep test by controlling the load applied on the top surface of cartilage. Green and red lines express the loading and deformation paths respectively.

Table 1.1: Definition of different parts of the synovial joint

Initial	Definition
AC	articular cartilage
TM	tide mark
CC	calcified cartilage
CL	cement line
ScBP	subchondral bone plate
ScP	subchondral plate
TB	trabecular bone

Table 1.2: Geometrical and material parameters and definitions

Parameter	Definition	Unit
L	Characteristic length	m
τ	Characteristic time	s
γ_w	Specific weight of the fluid	N/m ³
K	Hydraulic permeability	m ⁴ / Pa.s
E	Elastic modulus of cartilage	Pa
D	Diffusivity of cartilage	m ² /s
G	Shear modulus of cartilage	Pa
Y	Equilibrium Poisson's ratio	-
H	Viscosity of the fluid	N.s/m ²
H _A	Aggregate compressive modulus	Pa

Table 1.3: Characteristic time, τ based on the definition obtained by different studies.

τ (s)	Study
$\frac{L^2}{6Ek}$	[ABAQUS]
$\frac{L^2}{D} = \frac{L^2}{Gk} \left[\frac{1-2\nu}{2(1-\nu)} \right]$	[11]
$\frac{L^2}{H_A k}$	[43]

1.6 Reference

1. Armstrong CG, Lai WM, Mow VC: An analysis of the unconfined compression of articular cartilage. *J Biomech Eng* 106:165-73, 1984.
2. Behrou R, Foroughi H, Haghpanah F: Numerical study of temperature effects on the poro-viscoelastic behavior of articular cartilage. *J Mech Behav Biomed Mater* 78:214-23, 2018.
3. Biot MA: Theory of elasticity and consolidation for a porous anisotropic solid. *J Appl Phys* 26:182-5., 1955.
4. Biot MA: Mechanics of deformation and acoustic propagation in porous media. *J Appl Phys* 33:1482-98, 1962.
5. Biot MA: Theory of finite deformations of porous solids. *Indiana U Math J* 21:597-620, 1972.
6. Bobic V: Current methods of treating articular cartilage defects in the knee: an update on arthroscopic osteochondral autograft transplantation. *Arthroscopy* S10:14, 1998.
7. Bonde HV, Talman ML, Kofoed H: The area of the tidemark in osteoarthritis--a three-dimensional stereological study in 21 patients. *APMIS* 113:349-52, 2005.
8. Brittberg M, Lindahl A, Nilsson A, Ohlsson C, Isaksson O, Peterson L: Treatment of deep cartilage defects in the knee with autologous chondrocyte transplantation. *N Engl J Med* 331:889-95, 1994.
9. Buckwalter JA: Articular cartilage injuries. *Clin Orthop Relat Res* 402:21-37, 2002.
10. Burr DB, Gallant MA: Bone remodeling in osteoarthritis. *Nat Rev Rheumatol* 8:665-73, 2012.
11. Cai SQ, Hu YH, H ZX, Suo ZG: Poroelasticity of a covalently crosslinked alginate hydrogel under compression *J Appl Phys* 108:113514, 2010.
12. Chen AC, Bae WC, Schinagl RM, Sah RL: Depth- and strain-dependent mechanical and electromechanical properties of full-thickness bovine articular cartilage in confined compression. *J Biomech* 34:1-12, 2001.
13. Cicuttini F, Ding C, Wluka A, Davis S, Ebeling PR, Jones G: Association of cartilage defects with loss of knee cartilage in healthy, middle-age adults: a prospective study. *Arthritis Rheum* 52:2033-9, 2005.
14. Clark JM: The structure of vascular channels in the subchondral plate. *J Anat* 171:105-15, 1990.

15. Clark JM, Huber JD: The structure of the human subchondral plate. *J Bone Joint Surg Br* 72:866-73, 1990.
16. Curl WW, Krome J, Gordon ES, Rushing J, Smith BP, Poehling GG: Cartilage injuries: a review of 31,516 knee arthroscopies. *Arthroscopy* 13:456-60, 1997.
17. Czitrom AA, Langer F, McKee N, Gross AE: Bone and cartilage allotransplantation. A review of 14 years of research and clinical studies. *Clin Orthop Relat Res*:141-5, 1986.
18. Darling EM, Athanasiou KA: Articular cartilage bioreactors and bioprocesses. *Tissue Eng* 9:9-26, 2003.
19. Duncan H, Jundt J, Riddle JM, Pitchford W, Christopherson T: The tibial subchondral plate. A scanning electron microscopic study. *J Bone Joint Surg Am* 69:1212-20, 1987.
20. Egli PS, Hunziker EB, Schenk RK: Quantitation of structural features characterizing weight- and less-weight-bearing regions in articular cartilage: a stereological analysis of medial femoral condyles in young adult rabbits. *Anat Rec* 222:217-27, 1988.
21. Goldring MB: Articular cartilage degradation in osteoarthritis. *HSS J* 8:7-9, 2012.
22. Goldring MB, Goldring SR: Articular cartilage and subchondral bone in the pathogenesis of osteoarthritis. *Ann N Y Acad Sci* 1192:230-7, 2010.
23. Goldring SR: Alterations in periarticular bone and cross talk between subchondral bone and articular cartilage in osteoarthritis. *Ther Adv Musculoskelet Dis* 4:249-58, 2012.
24. Green WT, Jr., Martin GN, Eanes ED, Sokoloff L: Microradiographic study of the calcified layer of articular cartilage. *Arch Pathol* 90:151-8, 1970.
25. Greenwald AS, Haynes DW: A pathway for nutrients from the medullary cavity to the articular cartilage of the human femoral head. *J Bone Joint Surg Br* 51:747-53, 1969.
26. Hjelle K, Solheim E, Strand T, Muri R, Brittberg M: Articular cartilage defects in 1,000 knee arthroscopies. *Arthroscopy* 18:730-4, 2002.
27. Hunziker E, Quinn T, Shimaoka E, Hauselmann H: Quantitative structural organization of the normal adult human articular cartilage. *Trans Orthop Res Soc* 27:357, 2002.
28. Hunziker EB, Michel M, Studer D: Ultrastructure of adult human articular cartilage matrix after cryotechnical processing. *Microsc Res Tech* 37:271-84, 1997.

29. Hwang J, Bae WC, Shieu W, Lewis CW, Bugbee WD, Sah RL: Increased hydraulic conductance of human articular cartilage and subchondral bone plate with progression of osteoarthritis. *Arthritis Rheum* 58:3831-42, 2008.
30. Imhof H, Breitenseher M, Kainberger F, Trattnig S: Degenerative joint disease: cartilage or vascular disease? *Skeletal Radiol* 26:398-403, 1997.
31. Jackson DW, Lalor PA, Aberman HM, Simon TM: Spontaneous repair of full-thickness defects of articular cartilage in a goat model. A preliminary study. *J Bone Joint Surg Am* 83-A:53-64, 2001.
32. Jadin KD, Bae WC, Schumacher BL, Sah RL: Three-dimensional (3-D) imaging of chondrocytes in articular cartilage: growth-associated changes in cell organization. *Biomaterials* 28:230-9, 2007.
33. Lane LB, Bullough PG: Age-related changes in the thickness of the calcified zone and the number of tidemarks in adult human articular cartilage. *J Bone Joint Surg Br* 62:372-5, 1980.
34. Loeser RF, Goldring SR, Scanzello CR, Goldring MB: Osteoarthritis: a disease of the joint as an organ. *Arthritis Rheum* 64:1697-707 2012.
35. Madry H, van Dijk CN, Mueller-Gerbl M: The basic science of the subchondral bone. *Knee Surg Sports Traumatol Arthrosc* 18:419-33, 2010.
36. Mahjoub M, Berenbaum F, Houard X: Why subchondral bone in osteoarthritis? The importance of the cartilage bone interface in osteoarthritis. *Osteoporos Int* 23 Suppl 8:S841-6, 2012.
37. Maroudas A, Bullough P, Swanson SA, Freeman MA: The permeability of articular cartilage. *J Bone Joint Surg Br* 50:166-77, 1968.
38. Maroudas AI: Balance between swelling pressure and collagen tension in normal and degenerate cartilage. *Nature* 260:808-9, 1976.
39. Meachim G, Sheffield SR: Surface ultrastructure of mature adult human articular cartilage. *J Bone Joint Surg Br* 51-B:529-39, 1969.
40. Mente PL, Lewis JL: Elastic modulus of calcified cartilage is an order of magnitude less than that of subchondral bone. *J Orthop Res* 12:637-47, 1994.
41. Meyer FA: The use of enzyme-modified tissues to study selected aspects of tissue structure and function. In: *Methods in Cartilage Research*, ed. by A Maroudas, Kuettner KE, Academic Press, New York, 1990, 222-7.
42. Milz S, Putz R: Quantitative morphology of the subchondral plate of the tibial plateau. *J Anat* 185 (Pt 1):103-10, 1994.

43. Mow VC, Kuei SC, Lai WM, Armstrong CG: Biphasic creep and stress relaxation of articular cartilage in compression: theory and experiment. *J Biomech Eng* 102:73-84, 1980.
44. Mow VC, Ratcliffe A, Poole AR: Cartilage and diarthrodial joints as paradigms for hierarchical materials and structures. *Biomaterials* 13:67-97, 1992.
45. Muir H, Bullough P, Maroudas A: The distribution of collagen in human articular cartilage with some of its physiological implications. *J Bone Joint Surg Br* 52:554-63, 1970.
46. Muller-Gerbl M, Schulte E, Putz R: The thickness of the calcified layer of articular cartilage: a function of the load supported? *J Anat* 154:103-11, 1987.
47. Oegema TR, Carpenter R, Hofmeister F, Thompson RC: The interaction of the zone of calcified cartilage and subchondral bone in osteoarthritis. *Microsc Res Tech* 37:324-32, 1997.
48. Oegema TR, Jr., Carpenter RJ, Hofmeister F, Thompson RC, Jr.: The interaction of the zone of calcified cartilage and subchondral bone in osteoarthritis. *Microsc Res Tech* 37:324-32, 1997.
49. Oettmeier R, Abendroth K, Oettmeier S: Analyses of the tidemark on human femoral heads. I. Histochemical, ultrastructural and microanalytic characterization of the normal structure of the intercartilaginous junction. *Acta Morphol Hung* 37:155-68, 1989.
50. Oettmeier R, Abendroth K, Oettmeier S: Analyses of the tidemark on human femoral heads. II. Tidemark changes in osteoarthrosis--a histological and histomorphometric study in non-decalcified preparations. *Acta Morphol Hung* 37:169-80, 1989.
51. Pan J, Wang B, Li W, Zhou X, Scherr T, Yang Y, Price C, Wang L: Elevated cross-talk between subchondral bone and cartilage in osteoarthritic joints. *Bone* 51:212-7, 2012.
52. Redler I, Mow VC, Zimny ML, Mansell J: The ultrastructure and biomechanical significance of the tidemark of articular cartilage. *Clin Orthop Relat Res* 112:357-62, 1975.
53. Shibakawa A, Yudoh K, Masuko-Hongo K, Kato T, Nishioka K, Nakamura H: The role of subchondral bone resorption pits in osteoarthritis: MMP production by cells derived from bone marrow. *Osteoarthritis Cartilage* 13:679-87, 2005.
54. Simon BR: Multiphase poroelastic finite element models for soft tissue structures. *Appl Mech Rev* 45:191-218, 1992.
55. Steadman JR, Rodkey WG, Rodrigo JJ: Microfracture: surgical technique and rehabilitation to treat chondral defects. *Clin Orthop Relat Res* 391S:362-9, 2001.

56. Stockwell RA: The interrelationship of cell density and cartilage thickness in mammalian cartilage. *J Anat* 109:411-21, 1971.
57. Suri S, Gill SE, Massena de Camin S, Wilson D, McWilliams DF, Walsh DA: Neurovascular invasion at the osteochondral junction and in osteophytes in osteoarthritis. *Ann Rheum Dis* 66:1423-8, 2007.
58. Suri S, Walsh DA: Osteochondral alterations in osteoarthritis. *Bone* 51:204-11, 2012.
59. Venn M, Maroudas A: Chemical composition and swelling of normal and osteoarthrotic femoral head cartilage. I. Chemical composition. *Ann Rheum Dis* 36:121-9, 1977.
60. Walsh DA, Bonnet CS, Turner EL, Wilson D, Situ M, McWilliams DF: Angiogenesis in the synovium and at the osteochondral junction in osteoarthritis. *Osteoarthritis Cartilage* 15:743-51, 2007.
61. Wang Y, Ding C, Wluka AE, Davis S, Ebeling PR, Jones G, Cicuttini FM: Factors affecting progression of knee cartilage defects in normal subjects over 2 years. *Rheumatology (Oxford)* 45:79-84, 2006.
62. Yuan XL, Meng HY, Wang YC, Peng J, Guo QY, Wang AY, Lu SB: Bone-cartilage interface crosstalk in osteoarthritis: potential pathways and future therapeutic strategies. *Osteoarthritis Cartilage* 22:1077-89, 2014.
63. Zhang LZ, Zheng HA, Jiang Y, Tu YH, Jiang PH, Yang AL: Mechanical and biological link between cartilage and subchondral bone in osteoarthritis. *Arthritis Care Res (Hoboken)* 64:960-7, 2012.

CHAPTER 2:

3-D HISTOPATHOLOGICAL VISUALIZATION OF VASCULAR CANALS IN OSTEOARTHRITIS

2.1 Abstract

Introduction.

The interface of articular cartilage (AC) and subchondral bone (ScB) is an active remodeling site due to osteoarthritis (OA). Vascular canals embedded within ScB contain various types of cells and blood vessels and are present below the interface of the cartilage-ScB or penetrate through the cartilage. These canals are of many types, based on cap and the degree of penetration but are difficult to be imaged and visualized in three dimensions. The aim of this study is to establish and characterize the appearance of vascular canals with the Digital Volumetric Imaging method (DVI) in the NL and OA osteochondral tissue. Furthermore, coordinates, diameters, and spacing between canals are determined. The hypothesis was that the vascular canals are distinct based on their structures and penetrations, and their diameters and distribution change from one canal to another.

Method.

From 3D DVI datasets of 6 Normal (NL) and 5 OA osteochondral images, canal structures with the dimensions of ($\sim 1 \text{ mm}$)³ are classified based on cap and penetration. In addition to that, from vertical and horizontal images, coordinates of vascular canals ending at or penetrating through TM are determined using DataViewer from NL and OA samples. From the horizontal planes, effective diameters of the canals are calculated based on the

cross-sectional area of the canal. The average diameter over selected bins (lower 10%, lower 25%, mean, upper 25%, and upper 10%) is determined. Spacing is determined based on the closest and farthest nearest neighbors of the canal; and finally, three values of “small”, “mean” and “large” diameter and spacing are calculated.

Results.

For each sample, geometry and frequency of the canals of defined morphology (Cap, Extent of Penetration), with coordinate locations are determined. Diameters, bins (lower 10%, lower 25%, mean, upper 25%, upper 10%), and reduction to small, mean, and large diameter groups are calculated and three “small”, “mean” and “large” diameter and spacing are obtained.

Discussion.

More appearance of vascular canals ending at, or penetrating through the tidemark (TM) in OA samples compared with NL ones indicates that active remodeling of the interface is more likely to occur in the OA samples. In addition to that, the presence of these canals at the interface may cause cartilage degeneration. Under compressive loading, fluid flow within the cartilage may take the proteoglycans fragments out of the canals. Furthermore, under compression, depressurization occur within the cartilage which results in an increase of the stress and strain through the cartilage at the deep zone.

2.2 Introduction

In the normal adult synovial articular joint, articular cartilage (AC) as an avascular tissue, is attached to the calcified cartilage (CC) [8]. Calcified cartilage is a thin tissue layer, ~100 μm thick [16], separated from AC by tidemark (TM), 2-5 μm thick [18], and subchondral bone (ScB) by cement line (CL). Tidemark is a gently undulated border which protects articular cartilage from mineralization [20]. Subchondral bone merges into a porous network called trabecular bone (TB) [2, 8]. Clark [3, 4] visualized various cartilage layers using scanning electron microscopy (SEM) techniques. It was observed that the subchondral bone and calcified cartilage were penetrated by some vascular canals (VC) with the smallest size of 10-30 μm carrying blood vessels. These canals were found in two types: open and closed. In the open type, the canal was open at its top end. In the closed form, the canals did not open into the calcified cartilage and were capped by lamellar bone. However, there was no correlation found between the frequency of these two types and joint degeneration.

Canal invasion through the tidemark and its frequency appear to be a common feature in human osteoarthritis (OA) joints [1, 10, 17, 21-23]. The density of the invaded canals was higher in the OA group with respect to the normal (NL) group [1, 7, 10, 14, 23]. Shibakawa [19] observed that the density of the invaded canals through the calcified cartilage and below the tidemark for both NL and OA groups are similar while this invasion above tidemark is predominant in OA groups. This density of the canal invasion depends not only on aging [15] but also on load bearing area [11, 19] as well as some genetic factors. Independent of diagnostic groups, vascular density in the non-calcified cartilage increases with increasing degree of cartilage severity [14, 23].

Invasion of vascular canals through the tidemark may trigger the cartilage degeneration and mechanics especially at the deep zone [25]. On the one hand, The vascular canal invasion was observed to be accompanied by increase in cartilage calcification associated with the tidemark duplication at the deep zone, not only in the OA groups [1, 5, 6, 9, 12, 13, 24] but also in the high aged NL ones [1]. The duplication of tidemark and resultant thinning of the articular cartilage [12] would be predicted to increase the mechanical stress in the deep zone of the cartilage [7]. On the other hand, the presence of the vascular canals invaded through the articular cartilage may result in some exchange of fluid and soluble products within cartilage which may affect the activities of the cartilage components [7].

Various classifications, geometry, and density of the vascular canals are required in order to analyze the effect of the open canals on the biomechanics of articular cartilage. To address this information about the canals, first of all, the location of each canal should be determined. The hypothesis was to locate the canals based on their center coordinates, classify them according to the cap and un-capped end and the degree of penetration. Furthermore, diameters of the canals and spacing between them were determined based on the small, medium and large values. In this study digital volumetric imaging (DVI) method was used to characterize the appearance of the vascular canals. By using software DataViewer and ImageJ, data are collected and geometry and spacing of the canals have been determined.

2.3 Materials and Methods

2.3.1 Study design

Synovial tissue, containing the ScP, was used from eleven donors, $n = 6$ from normal and $n = 5$ from clinical OA donors (**Table 2.1 and 2.2**). The normal donor knee was retrieved from a cadaveric tissue bank, and the OA donors from remnant tissue were extracted during a total knee arthroplasty, both with IRB approval. Each of the eleven donor knees had a volume selected from the medial femoral condyle (MFC), taken from a weight-bearing region that represented the worst grade in the condyle: (1) normal/non-fibrillated for the normal donor sample, and (2) partial thickness erosion for all four OA donor samples. This selected volume was processed and imaged by DVI (**section 2.3.2**) and qualitatively assessed for the different types of vascular canals using two descriptors (**section 2.3.5**) (at 10X). From the vertical and horizontal images, coordinates of vascular canals for both NL and OA samples were determined using DataViewer. From horizontal images (at the tidemark, or above), effective diameter based on the area of the canal was measured. Average diameter over the selected bins (lower 10%, lower 25%, mean, upper 25%, and upper 10%) was determined. From coordinates of each canal, the spacing between canals was obtained and the closest, mean and farthest nearest neighbors were determined. Finally, values for “small”, mean, and “large” diameter and spacing were determined.

2.3.2 Sample preparation and imaging

Samples were taken from a weight-bearing region that represented the worst grade in the condyle: (1) normal/non-fibrillated for all six normal donor samples, and (2) partial thickness erosion for all five OA donor samples. ((~4 mm)³ cube (50% bone, 50% cartilage) centered around the ScP was extracted using a scalpel and processed to be prepared for DVI imaging. Each sample cube was fixed in 4% paraformaldehyde in phosphate-buffered saline for 48 hours, then decalcified in a solution for 10% EDTA in phosphate buffered saline for at least 72 hours. The samples were then stained with Acridine Orange and Eosin Y, sequentially dehydrated with graded alcohol, held in xylene, and embedded in Spurr resin. The cured resin block was sectioned and imaged in a DVI machine (MicroSciences Corp., Corte Madera, CA). The DVI acquired the block face images of the tissue with a 10X objective, cutting the block after each image at a thickness equivalent to the pixel resolution of each image acquired (0.89 μm), for isotropic voxel size. The machine software processed the data into a stack of ~(2000 x 2000) pixel RGB images (~2000 images at (0.89 μm)/pixel resolution, ~10GB per set), or a 3-D dataset encompassing a (1 mm)³ volume.

2.3.3 Image processing

The output dataset was aligned using 3-D image rotation software so that the tidemark was leveled relative to the frame of the reference of the sample, and then the sample was cropped systematically to remove dark areas (excess imaged area) around the sample. Using Dataset in DataViewer <DataViewer, Version 1.5.6.2, Jan., 2018> images

of the samples are open. For each open canal, the horizontal plane and one vertical plane are kept fixed and other vertical plane moves until the largest cross section of the channel end (at first TM or above) is achieved.

2.3.4 Assumptions

Due to the complexity of the geometry of images, there are some assumptions made to simplify the visualization and calculations. First, tidemark (TM) and cement line (CL) are assumed to be flat planes. Depending on the scale we choose it may not be a good assumption. Compared to the channel size, this assumption may play a role. Ignorance of the undulation is appropriate only when there is a large scale. But if the length we are investigating is close to the undulation height, our assumption would not be appropriate. If the scale is larger than the canal size, the results are more accurate. However, for each assumption, we have a limitation. Second, the tissue above the first TM is considered as articular cartilage (AC). In OA samples there are multiple TMs observed in the deep zone of AC. However, the material properties of these zones have not been determined yet and from the appearance, there is a difference observed between AC and the area between TMs. Third, canals ending at a distance of $\pm 5\mu\text{m}$ below or above the first TM are considered as the canals ending at TM. Finally, the largest cross-section of the canal at or above the first TM is considered during calculations of coordinates and diameters. There is more fluid going in or coming out of the canals with larger diameters. The resistance of the canals to the fluid flow is lower than when the canal has a smaller diameter. Therefore, larger canal

diameter is more significant when the fluid flow occurs within cartilage. In **Fig. 2.1.**, all these assumptions are made.

2.3.5 Classification of the canals

Vascular canals were categorized based on two descriptors (**Table 2.3**): the cap and depth to which they penetrated (deep-to-superficial), that is, the location of the blunt end of the channel, based on the surrounding layer: bone, calcified cartilage or uncalcified cartilage. Based on cap classification, if the canal is completely surrounded by bone, it is considered as (C)losed canal (**Fig. 2.2**). If the canal only does not have the cap above the canal end, it is considered as (O)pen. If the canal misses some parts of the bony wall, it is considered as missin(G)one. Based on the penetration classification, if the vascular canal is entirely below the cement line (CL), the canal is classified as (N)on penetrating. If the canal reaches the zone below the first TM, it is considered as penetrating cement (L)ine. It should be noted that a vascular canal that is capped cannot penetrate the cement line as the surface of the cap is part of the surface of the cement line by definition. If the canal ends at the TM and does not penetrate through the TM, it is categorized as (E)nding at first TM. Finally, if the vascular canal reaches the uncalcified cartilage, it is categorized as penetrating (T)idemark

2.3.6 Determination of coordinate of vascular canal center

Fig. 2.3 shows the vertical and horizontal planes of a typical vascular canal from sample “wdb-414-s08” ending at TM. There is a color cube showing different sides of the

sample by a distinct color from the superficial zone to deep zone. From the color lines around the vertical and horizontal images, it can be clear which plane is taken. Vertical and horizontal planes are transferred to ImageJ processing in order to measure the coordinates. From the vertical plane (**Fig. 2.3A**) the canal is magnified (**Fig. 2.3B**) and double TMs are traced (**Fig. 2.3C**). Two corners of the canal end (points “a” and “b”) are located, and their coordinates are obtained. Based on these two coordinates, the coordinate of the middle point (c) is calculated.

2.3.6.1 Y- coordinate

According to the calculation above for getting coordinates of point (c), “y-coordinate” of point (c) is considered as the “y-coordinate” of the canal center:

$$y_i^c = \frac{y_i^a + y_i^b}{2} \quad (1)$$

Where “i” is the canal number.

2.3.6.2 X- and Z-coordinates

From the corresponding horizontal plane, the image is transferred to ImageJ (**Fig. 2.3. D**) and magnified. The canal perimeter is marked, and the x and z coordinates are recorded (**Fig. 2.3 E**). Using MATLAB (function “mean”), the mean “x” and “z” coordinates are calculated and defined as the center of each canal, x_i , and z_i .

$$x_i^c = \frac{\sum_{j=1}^n x_j}{n} \quad (2)$$

$$z_i^c = \frac{\sum_{j=1}^n z_j}{n} \quad (3)$$

Where “n” is the number of coordinates along the border of the canal cross-section. In this study, $n \approx 20$ for each canal cross-section.

2.3.7 Determination of canal diameter

Using the $[x_i, z_i]$ dataset for each vascular canal, data are analyzed using MATLAB program (function “polyarea”) to obtain the canal cross-sectional area. Thus, the effective

canal diameter, d_{CH} , is calculated as $d_{CH} = \sqrt{\frac{4Area}{\pi}}$.

2.3.8 Determination of canal spacing

From the horizontal plane for each sample (**Fig. 2.4**), a 100 μm length of each side was removed (dashed square) during the analysis. Thus: First, edge effects are removed. Usually, during the experiment, when the sample is cut, the cells at the edges die. Second, the canals in this area don’t have enough canal neighbors. Third, if this edge is not removed, the largest distances between canals refer to the size of the sample which is not of our interest. Only canals left inside the remaining horizontal plane including those that have centers more than 10 μm within the border are considered for calculations. For each sample, if there is “m” coordinates corresponded to m canals, the 3D distances between i^{th} coordinates ($i=1:m-1$) and j^{th} coordinates ($j=i+1:m$) would be as follows:

$$Sp_{i,j} = \begin{bmatrix} 0 & Sp_{1,2} & Sp_{1,3} & \dots & Sp_{1,N} \\ 0 & 0 & Sp_{2,3} & \dots & Sp_{2,N} \\ \vdots & \vdots & \vdots & \ddots & \vdots \\ 0 & 0 & 0 & \dots & 0 \end{bmatrix}$$

$$Sp_{i,j} = \sqrt{(x_j - x_i)^2 + (y_j - y_i)^2 + (z_j - z_i)^2}$$

where i, j represent the canal numbers and “N” is the total number of the canals for each sample. Then, based on the matrix above we have all spaces between canals for each sample with no duplication. Now, for each canal, the closest neighbor is found and there are N canal neighbors for each sample.

2.3.9 Canal diameter and spacing statistics

To determine three values of “small”, “mean” and “large” diameters, for each sample, channel diameters from low to high. The bottom 10% and 25%, mean, and upper 25% and 10% of diameters and are determined. First, the mean of all samples for each bin is determined. The small diameter is the mean of the lower 10 and 25 % values. The mean diameter is the mean of mean values and the large diameter is the mean of the upper 10 and 25 % values.

To determine three values of “small”, “mean” and “large” spacing, the closest canal neighbors obtained from **Section 2.3.8** are sorted and lower and upper 10% of the spaces as well as means of closest neighbors for each sample are determined. For each 10%, the mean is calculated. The small spacing is the mean of the mean of lower 10% of all samples. The mean spacing is the mean of means for all samples and the large spacing is the mean of the mean of upper 10% of the canals for all samples.

2.4 Results

A general appearance of the vascular canals in the DVI imaging data is described below (**section 2.4.1**), followed by detailed distribution and description of the different types or feature categories and coordinates of open canals, and sorted by prevalence in the grade of the samples: NL and OA. In **section 2.4.2** and **2.4.3**, coordinates, diameters, and spacing of open canals are determined respectively and sorted based on three values: small, mean and large.

2.4.1 Appearance and classifications of canals

Vascular canals were apparent as the small finger penetrated canals, distinct from the surrounding bone or calcified cartilage tissue in that they did not stain at all for Eosin Y (green) and had minimal staining on a volume basis for Acridine Orange (red). These canals vary with shape and their cross sections which could be either uniform or changed. However, all canals are tube-like and connected to the larger marrow spaces below. **Fig. 2.5** represents three different canals from NL samples (first two columns) or OA samples (last four columns). The schematics show the simplification progression of each canal. For the first canal, it does not penetrate through the TM, even though it has a fingerlike shape. This canal is completely surrounded by bone. Since it is assumed that calcified cartilage (CC) is much stiffer than AC, the presence of the canals underneath cartilage would not affect the biomechanics of cartilage. The second canal ends at the first TM, then it is simplified as exactly a canal ending at TM1. Whatever is above TM1 is counted as AC. The third canal penetrates TM1. However, based on our assumptions, we consider the largest cross-section at or above TM as the diameter of the canal.

Based on the classifications shown in **Table 2.3**, if the canals are classified based on “C”, “G” or “O” but “E” or” T”, they are considered as closed canals. Even if they are “C” and either “e” or “T”, they are still considered as closed canals. Otherwise, they are open. According to **Tables 2.4 and 2.5**, from six NL samples, there are 112 canals found in total where only 11 of them are open. Compared to the NL canals, there are 108 canals found in five OA samples, where 38 of them are open and other 70 ones are closed. The cap and penetration can be categorized by indices: C=1 while Either “O” or “G” (O/G=2/3), N=1, L=2, E=3, and T=2. **Tables 2.6 and 2.7** represent data based on the explanation above regarding the closed and open canals. Then for NL samples, only 10% of the canals are open, while for OA samples, 35% of the canals are open. Finally, the density of the closed and open canals per 1mm² of the NL and OA sample area were calculated (**Tables 2.8 and 2.9**). The number of the closed canals in NL versus OA samples was 16 ± 6 versus 14 ± 7 per mm², while the number of closed canals in NL versus OA samples was 2 ± 2 versus 7 ± 4 .

2.4.2 Coordinate and diameter of the canal

Center location and diameter of each open canal has been determined according to its classification for NL (**Table 2.10**) and OA samples (**Table 2.11**). For NL samples there are only three samples represented since from six NL samples, in only three of them open canals are observed. Diameters of open canals vary in size from 15μm to 60μm, while for OA samples the diameter size reaches over 100μm. According to horizontal planes, at average TM, and 40μm above and below TM, It has been observed that the frequency of

the canals showed by their coordinates and numbers is higher for OA samples rather than NL Samples (**Fig. 2.6**).

Three “small”, “mean” and “large” values of diameters have been determined based on the statistics for NL (**Table 2.12**) and OA samples (**Table 2.13**). From the means, the final three values are determined (**Table 2.14**).

2.4.3 Canal spacing

Spacing is determined after cutting off 100 μ m of the edge around the sample. **Tables 2.15** represents the samples and the number of canals used for spacing calculation for NL and OA samples respectively. **Tables 2.16** and **2.17** show spacing measurements represented as matrix and color codes. Color codes show different distributions of the canal sizes with the related spacing. **Tables 2.18** and **2.19** show the various distribution of the diameters with the spacing. **Tables 2.20** and **2.21** show the statistical way to get three “small”, “mean” and “large” spacing. And finally, three spacing with mean and standard deviation have been determined (**Table 2.22**).

2.4.4 “Small”, “mean” and “large” diameters and spacing

Tables 2.23 and **2.24** show the final vascular canal diameters and spacing for NL and OA samples. In NL samples, diameter ranges from 27-46 μ m, while for OA ones, it ranges from 29-67 μ m. Spacing in NL samples ranges from 359-809 μ m while for OA ones it ranges from 137-405 μ m.

2.5 Discussion

The results obtained by DVI from six normal (NL) and five osteoarthritis (OA) samples confirm that the density of the open canals ending at or penetrating through the tidemark (TM) is higher in OA samples (**Tables 2.8 and 2.9**), in association with the structural changes in the deep zone of cartilage and presence of multiple tidemarks within cartilage and close to the interface of uncalcified cartilage and calcified cartilage. The magnitude of large diameter of the canals for OA samples was about 20 μm greater than the ones of NL samples (**Tables 2.23 and 2.24**), while the range of small, mean and large the spacing between canals for OA samples was significantly smaller than those of NL ones respectively (**Tables 2.23 and 2.24**).

Vascular canal classification was performed in order to obtain center coordinate and geometry of the canals (**Fig. 2.2**). Based on the classification categories, there were 12 different classifications associated with cap/uncap and the degree of penetration of the canals. From these 12 classifications, three of them (CL, ON, and GN) did not exist since those were the same as CN classification. Furthermore, OT classification was not found among 11 total samples. From NL samples, there was no invaded open canal through tidemark (**Table 2.10**), while from 37 open canals in OA samples, 11 of them were penetrated through the tidemark (**Table 2.11**). In the end, all different classifications were categorized into two simplified models with or without open canal ending at tidemark (**Fig. 2.5**). Clark [4] classified the canals just based on the cap but degree of penetration. In that study, the samples were taken from human, rabbit, and dog with no report of joint disease. In addition to the canal classification, 3D coordinates of the open canals were obtained (**Table 2.10 and 2.11**) and used to determine the diameter and spacing of the canals.

Diameters of the canals and the spacing between them were determined for each NL and OA sample. Three small, mean and large diameters and spacing were obtained in order to analyze the biomechanics of articular cartilage. The diameter of the canals were as small as 27 μm in NL samples and as large as 67 μm in OA samples. The smallest and largest sizes of the canals were reported to be 10-30 and over 100 μm respectively, but it was not specified whether they were obtained from NL or OA joint [4]. The spacing between the open canals were as small as 135 μm in OA samples and 809 μm in NL ones. It was observed that those of interfaces containing large canal diameters and small spacing belongs OA samples and may result in higher degeneration within the deep zone of cartilage. In fact, an increase of canal diameter and a decrease of spacing may cause that under loading of the joint, more fluid flow occurs through the canal which carries nutrients and, some cells and enzymes comes through the cartilage from the subchondral bone which may be associated with the calcification and increase of tidemarks at the deep zone.

There were some assumptions in this study related to the method of classification of the canals and geometry calculation. Calcified cartilage and subchondral plate together construct the subchondral bone. Since the material properties of the multiple tidemark regions have not been determined yet by any other study, this region was considered as uncalcified cartilage. Furthermore, the undulation of the tidemark and cement line was ignored. Regarding the canal assumptions, under compressive loading, cartilage bulges through the canal entrance, and shape and slope of the canal do not affect the biomechanics of cartilage significantly. Thus, canals with any shape and angle were assumed to be vertical and uniform.

The density of the canals penetrating tidemark was studied previously on different animal samples [17]. However, it was not determined if those canals were either open or closed and how the degree of penetration was determined. It was observed that in human, maximum penetrated vessel for a NL sample was 10 per 3.9 cm², while for an OA sample was 47 per 5.1 cm² of tidemark[1]. Shibakawa [19] reported the number of the pits penetrating tidemark in NL sample was ~0.25 per 10mm while in OA sample it was ~1.25 per 10mm. In this study, the maximum open canals ending at, or penetrating tidemark was 7±4 per mm² in OA sample and 2±2 per mm² in NL samples, corresponding to OA sample WDB 414 (**Table 2.9**). Comparing the results obtained from previous studies to the ones of the current study, it is confirmed that density of the canals (especially open ones) penetrating tidemark is higher in OA samples with respect to the NL ones.

Statistical analyzes in this study were based on small, mean and large diameter and closest nearest neighbor for spacing calculation. Three diameters were calculated according to the first 10 and 25% and last 10 and 25 % and the means of diameters of the open canals in both NL and OA samples. To determine the spacing between two open canals, the extreme case was predicted to be when those two canals placed in the nearest neighbor which may help trigger early cartilage degeneration.

As a conclusion, for both NL and OA samples, vascular canals were classified based on their cap and the degree of penetration and finally were simplified to two closed and open canals. The coordinates of open canals, as well as their diameters and spacing between them, were determined in order to obtain three small, mean and large diameter and the spacing between canals. Having these geometrical data, we analyzed the effect of open canals on the biomechanics of cartilage. In this study, synovial joint vascular density

increased with increasing cartilage severity associated with osteoarthritis. The presence of these canals in addition to calcifying cartilage may cause pain and swelling. Therefore, knowing the geometry and frequency of these canals may help to recognize OA disease and protect the joint from further degeneration development.

2.6 Acknowledgment

Chapter 2 is being prepared for submission to *Journal of Biomechanics*. The dissertation author is the co-author and thanks author Dr. Neil Chang and other co-authors Jason P. Caffrey, Matthew K Wang, Alborz Jelvani, Nasim Eshragh Nia, Van W Wong, Dr. William D Bugbee, Dr. Albert C. Chen, Prof. Shengqiang Cai, Dr. Koichi Masuda and Prof. Robert L. Sah for their contributions.

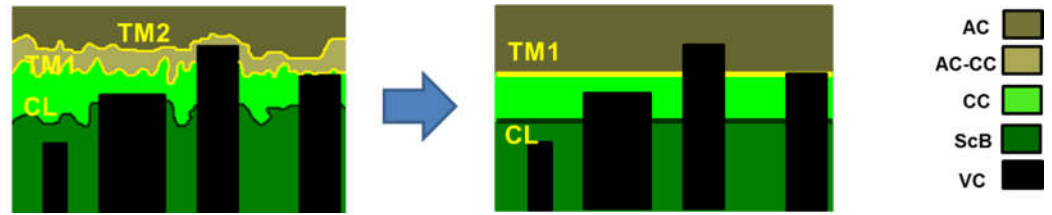


Figure 2.1: Schematics of the assumptions to simplify the interface of cartilage and bone: there is no undulation of tidemarks and tidemarks, the area between multiple tidemarks is considered as articular cartilage, the area underneath the first tidemark is considered as a bone.

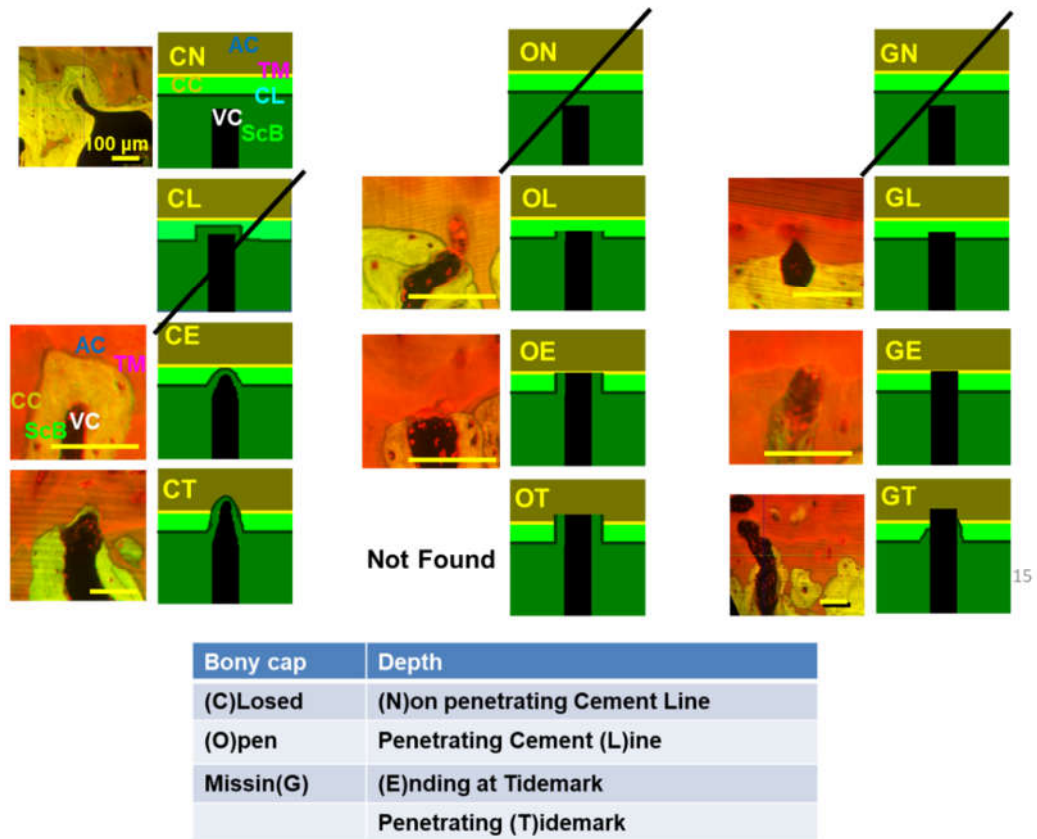


Figure 2.2: Classification of canals according to their bony cap and the degree of penetration. In general, there are three groups of bony cap and 4 groups of penetrations. In total, there should be 12 categories of canals. CL, ON and GN categories are similar to CN one and are ignored. In this study, the OT category was not found among all samples.

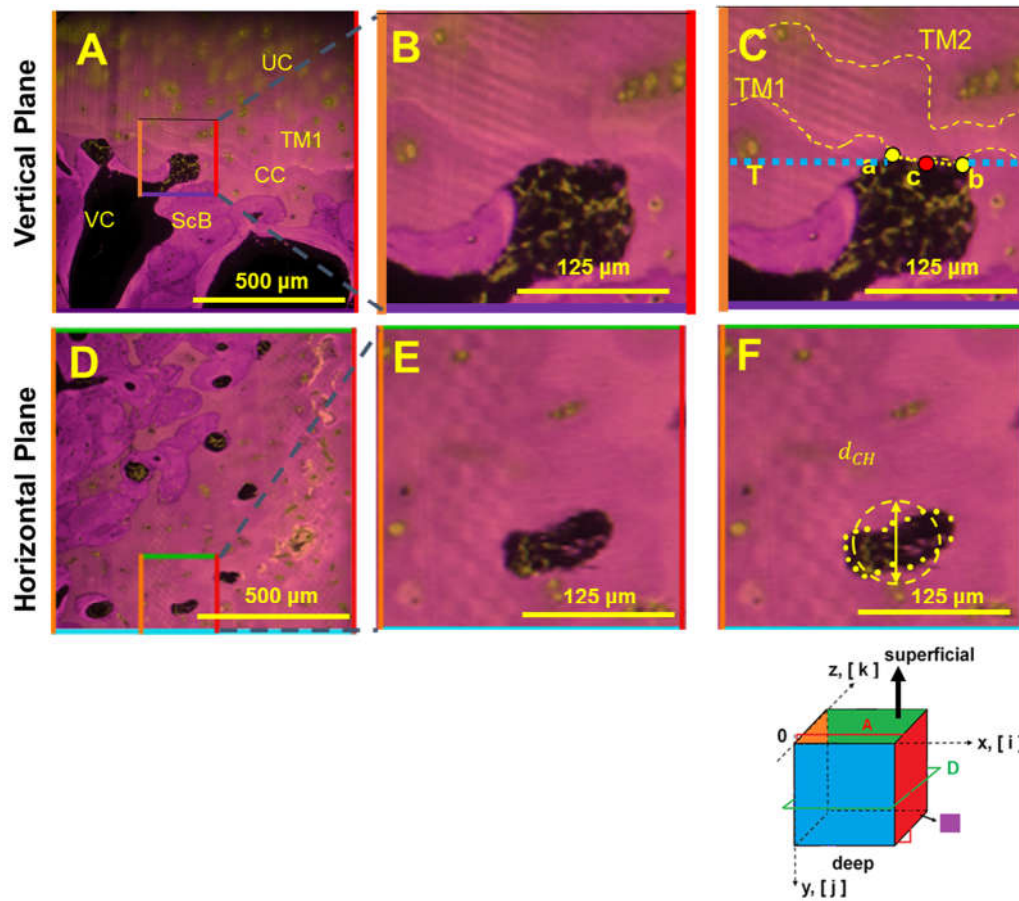


Figure 2.3: Method of determination of vascular canals center coordinate and diameter. A) A typical open GE canal from sample WDB414. B) 4X magnification of the canal presented in the square in panel A. C) determination of point c as the y coordinate of the canal and horizontal plane D (blue dashed line T) by using points a and b. D) Horizontal plane associated with the GE canal at point c of panel C. E) 4X magnification of the canal cross section presented in panel D. F) Equivalent diameter of the canal. The color frame around each panel is based on the color cube.

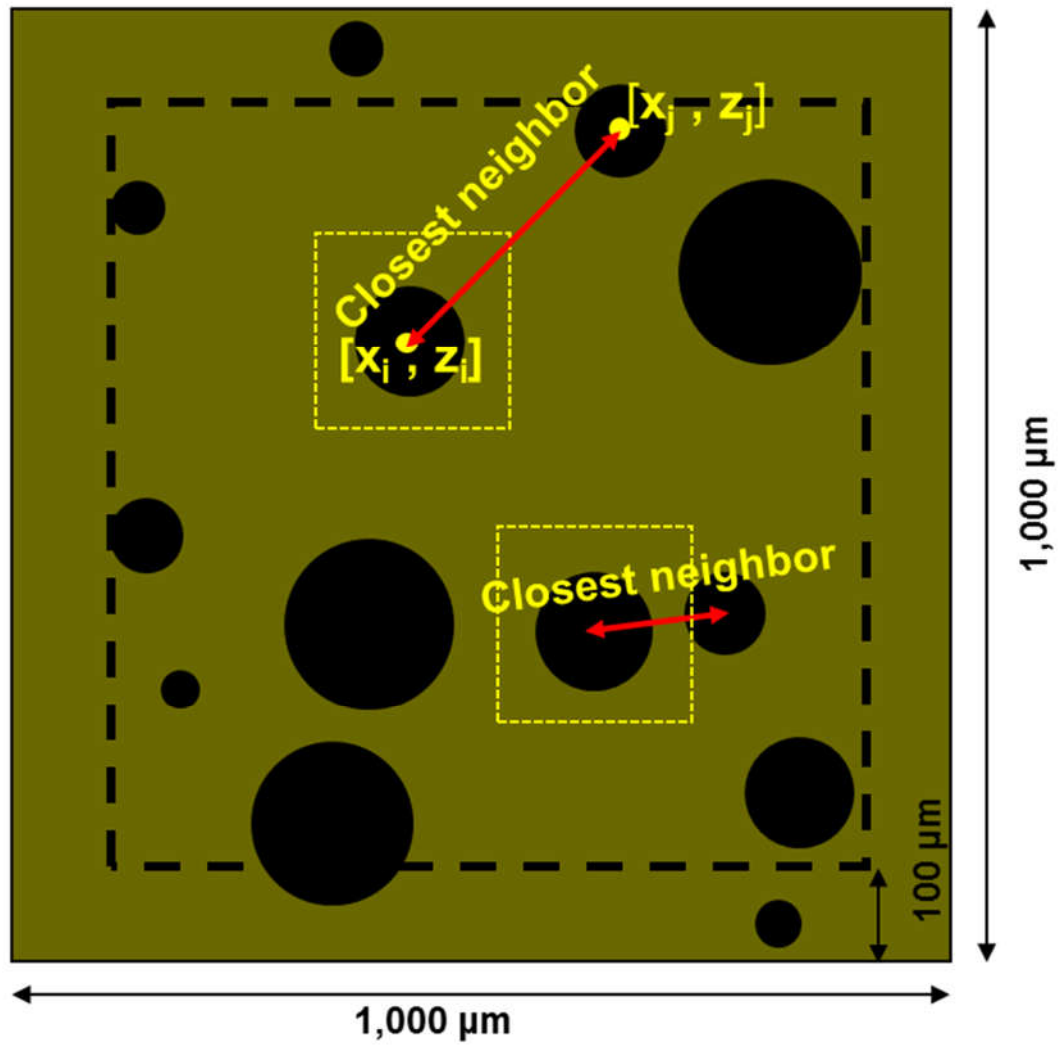


Figure 2.4: Schematics representing the method of determination of small, mean and large spacing between the canals. This method is based on a closest neighbor of each canal. The average sample size is 1mm.

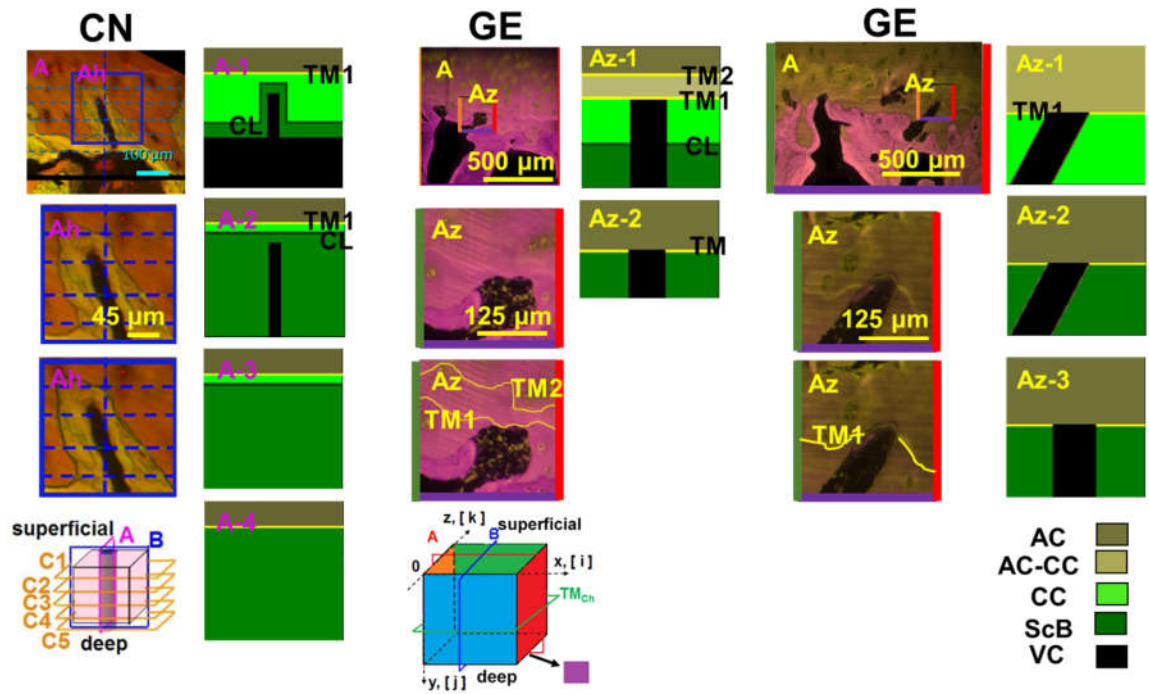


Figure 2.5: Method of simplification of the canal for three different categories of canal appearance. Categories CN, two GE are shown. The final schematics for each category is the last simplified representative of the canal within cartilage and bone.

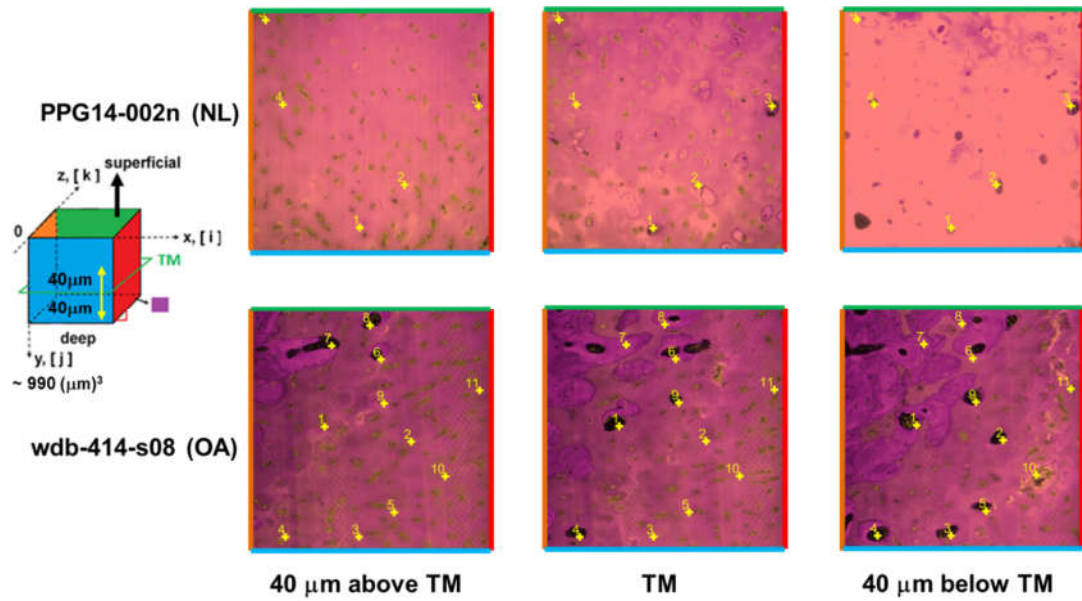


Figure 2.6: Representation of the open canals in the horizontal section for NL sample PPG14-002n and OA sample WDB414. For each sample, there are three horizontal cross-sections represented: average TM plane and two other planes of 40 μm below and above TM plane of the sample.

Table 2.1: Clinical details of normal (NL) and osteoarthritis (OA) samples analyzed in this study

Group	Treatment	N	F/M	Age range
1	Normal (NL)	6	4F, 2M	42-57
2	Osteoarthritic (OA)	5	4F,1M	54-78

Table 2.2: Sample IDs and the google paths of NL and OA samples

Sample	ID	Treatment	Google drive location
1	PPG10-084-s08-rotated cr	NL	https://drive.google.com/open?id=1Ea4rguWfnWj8_4-uCLeKS2CdF94Pw72t
2	PPG11-016-rotated	NL	https://drive.google.com/open?id=1D0VpqwfsFjXLqSUdiCe0QhhhIzKWK14T
3	PPG10-020-rotated-cr	NL	https://drive.google.com/open?id=1lmMF6o2RynScFn50BU5dFeRpcA8QP_t7
4	PPG14-056n-rotated-cr	NL	https://drive.google.com/open?id=1t19ZOHesHL8O8jphOXr0W2lhvqaLXpL2
5	PPG14-002n-rotated-cr	NL	https://drive.google.com/open?id=1THIFs4Ugo2BzwEztNsdIwS8RpxjSLAWf
6	PPG13-052-rotated-cr	NL	https://drive.google.com/open?id=1ROqw9d265ROdzPSxU7hjhITfsn23OFPC
7	wdb-121-rotated-cr	OA	https://drive.google.com/open?id=1ALhGotIvc9OeQgdBkHKnwquW8zfbyGDn
8	wdb-414-s08-rotated cr	OA	https://drive.google.com/open?id=0B3rPuWI_4jN8amxsZ3FaVFRyWmc
9	wdb-422-rotated-cr	OA	https://drive.google.com/open?id=1sDkWdSJQ5uV2uBkFU10cbDd3QnG-XaMO
10	wdb-575-rotated-cr	OA	https://drive.google.com/open?id=12gJuHOQwntm2i9Gn_3niq_WKDS_LQp4M
11	wdb-635-rotated-cr	OA	https://drive.google.com/open?id=1mZbBN_hUNf7I6LeXSHo_tAxK_AxSAHv15

Table 2.3: Classification of vascular canals according to their caps and the degree of penetration

Bony cap	Depth
(C)losed	(N)on-penetration
(O)pen	Penetration Cement (L)ine
Missin(G)	(E)nding at Tidemark
	Penetrating (T)idemark

Table 2.4: Quantification of vascular canal types in NL samples

Sample ID (NL)	Closed channels	Open channels	Total channels
PPG13-052-b1	13	0	13
PPG14-002n	23	5	28
PPG14-056n	23	2	25
PPG10-020	15	0	15
PPG11-016	16	4	20
PPG10-084- s08	11	0	11
Total	101	11	112

Table 2.5: Quantification of vascular canal types in OA samples.

Sample ID (OA)	Closed channels	Open channels	Total channels
WDB121	13	3	16
WDB414	9	11	20
WDB575	7	10	17
WDB635	20	10	30
WDB422	21	4	25
Total	70	38	108

Table 2.6: Quantification of vascular canals according to two simplified closed and open canals in NL samples

Grp (NL)	Grade	Cap (C:1, O/G:2/3)	TM1 Penetration (N:1, L:2, E:3, T:4)	N	%	Pooled (%)
1	Closed	1	1	70	62	90
2	Closed	1	2	0	0	
3	Closed	1	3	1	1	
4	Closed	1	4	0	0	
5	Closed	2/3	1	0	0	
6	Closed	2/3	2	30	27	
7	Open	2/3	3	11	10	10
8	Open	2/3	4	0	0	
Total				112	~100	100

Table 2.7: Quantification of vascular canals according to two simplified closed and open canals in OA samples

Grp (OA)	Grade	Cap (C:1, O/G:2/3)	TM1 Penetration (N:1, L:2, E:3, T:4)	N	%	Pooled (%)
1	Closed	1	1	53	49	65
2	Closed	1	2	1	1	
3	Closed	1	3	1	1	
4	Closed	1	4	1	1	
5	Closed	2/3	1	0	0	
6	Closed	2/3	2	14	13	
7	Open	2/3	3	27	25	35
8	Open	2/3	4	11	10	
Total				108	~100	100

Table 2.8: Quantification of number of closed and open vascular canals per 1mm² of the NL sample

(NL) Sample	1	2	3	4	5	6	Within Samples # / (mm)²	All Samples # / (mm)²
Type	# / (mm)²							16 ± 6 (Closed)
CN	11	16	13	15	7	4	11 ± 5	
CE	0	0	0	0	0	0	0	
CT	0	0	0	0	1	0	0	
O/G L	2	7	10	0	3	7	5 ± 4	
O/G E	0	5	2	0	3	0	2 ± 2	2 ± 2 (Open)
O/G T	0	0	0	0	0	0	0	

Table 2.9: Quantification of the number of closed and open vascular canals per 1mm² of the OA sample

(OA) Sample	1	2	3	4	5	Within Samples # / (mm)²	All Samples # / (mm)²
Type	# / (mm)²						14 ± 7 (Closed)
CN	7	8	2	18	19	11 ± 8	
CE	0	0	0	0	1	0	
CT	0	0	1	0	0	0	
O/G L	6	1	2	2	1	2 ± 2	
O/G E	3	7	4	8	4	5 ± 2	7 ± 4 (Open)
O/G T	0	4	4	2	0	2 ± 2	

Table 2.10: Representation of the classification of the open canals, their coordinates, diameter, and total numbers for each NL sample

Sample ID (NL)	Channel Number	Classification	$[x_c, y_c, z_c]$ ($\mu\text{m}, \mu\text{m}, \mu\text{m}$)	Diameter (μm)	N
PPG14-002n	1	GE	[448,418,95]	15.0	5
	2	GE	[633,406,272]	18.2	
	3	GE	[938,433,595]	20.7	
	4	GE	[132,454,602]	31.3	
	5	GE	[60.6,433,951]	34.5	
PPG14-056n	1	OE	[729,593,328]	39.3	2
	2	GE	[136,603,878]	44.1	
PPG11-016	1	OE	[772,674,123]	25.7	4
	2	GE	[1132,692,243]	32.0	
	3	OE	[734,1702,479]	39.4	
	4	OE	[384,638,1001]	60.2	

Table 2.11: Representation of the classification of the open canals, their coordinates, diameter, and total numbers for each OA sample

Sample ID (OA)	Channel Number	Classification	$[x_c, y_c, z_c]$ ($\mu\text{m}, \mu\text{m}, \mu\text{m}$)	Diameter (μm)	N
WDB121	1	GE	[535,618,295]	47.2	3
	2	GE	[553,619,27]	31.8	
	3	OE	[763,614,293]	61.9	
WDB414	1	GE	[287,413,519]	49.9	11
	2	GE	[638,466,457]	43.2	
	3	GE	[425,473,71]	64.0	
	4	GE	[127,422,71]	45.8	
	5	GE	[570,473,171]	53.5	
	6	GT	[515,367,791]	39.9	
	7	GT	[316,349,846]	73.2	
	8	GT	[472,358,929]	41.6	
	9	GT	[528,402,613]	53.7	
	10	OE	[776,511,317]	86.2	
	11	OE	[915,506,666]	45.8	
WDB575	1	GE	[986,358,535]	35.6	10
	2	GE	[335,399,150]	31.0	
	3	GE	[957,445,193]	31.6	
	4	GE	[352,370,638]	33.1	
	5	GE	[1092,506,144]	56.4	
	6	GT	[23.4,324,260]	82.7	
	7	GT	[737,304,562]	103.9	
	8	GT	[635,331,377]	57.2	
	9	GT	[78.2,352,562]	49.5	
	10	GT	[228,319,553]	78.9	
WDB635	1	GE	[635,299,513]	39.9	10
	2	GE	[76,333,782]	53.5	
	3	GE	[220,320,788]	30.9	
	4	GE	[387,352,896]	27.3	
	5	GT	[348,260,640]	38.5	
	6	GT	[40.1,301,700]	83.8	
	7	OE	[688,271,537]	35.8	
	8	OE	[101,342,551]	44.1	
	9	OE	[827,322,709]	32.3	
	10	OE	[492,310,714]	30.3	
WDB422	1	GE	[757,201,230]	27.3	4
	2	OE	[110,158,362]	11.0	
	3	OE	[180,107,742]	28.6	
	4	OE	[233,144,860]	40.9	

Table 2.12: Determination of three small, mean and large diameters of open vascular canals in NL samples. The calculation was based on the first 10 and 25%, mean and last 10 and 25 % of the diameters for each sample

NL	Definition	PPG14-002n	PPG14-056n	PPG11-016	Mean of means (μm)
N	Number of OA channels	5	2	4	
10% d_{Small}	0-10% of smallest diameters	15.0	39.3	25.7	
10% d_{Large}	90-100% of largest diameters	34.5	44.1	60.2	
25% d_{Small}	0-25% of smallest diameters	15.0 18.2	39.3	25.7	
25% d_{Large}	75-100% of largest diameters	31.3 34.5	44.1	60.2	
10% d_{Small}	0-10% of smallest diameters	15.0 \pm 0.0	39.3 \pm 0.0	25.7 \pm 0.0	26.7 \pm 12.1
10% d_{Large}	90-100% of largest diameters	34.5 \pm 2.2	44.1 \pm 0.0	60.2 \pm 0.0	46.3 \pm 13.0
25% d_{Small}	0-25% of smallest diameters	16.6 \pm 0.0	39.3 \pm 0.0	25.7 \pm 0.0	27.2 \pm 11.4
25% d_{Large}	75-100% of largest diameters	32.9 \pm 2.3	44.1 \pm 0.0	60.2 \pm 0.0	45.7 \pm 13.7
Mean	Average diameters	24.0 \pm 8.5	41.7 \pm 3.5	39.3 \pm 15.0	35.0 \pm 9.6
Total	Average of the N diameters	32.8 \pm 13			

Table 2.13: Determination of three small, mean and large diameters of open vascular canals in OA samples. The calculation was based on the first 10 and 25%, mean and last 10 and 25 % of the diameters for each sample

OA	Definition	WDB 121	WDB 414	WDB 575	WDB 635	WDB 422	Mean of means (µm)
N	Number of OA channels	3	11	10	10	4	
10% d_{Small}	0-10% of smallest diameters	31.8	39.9 41.6	31.0	27.3	11.0	
10% d_{Large}	90-100% of largest diameters	61.9	73.2 86.2	103.9	83.8	40.9	
25% d_{Small}	0-25% of smallest diameters	31.8	39.9 41.6 43.2	31.0 31.6 33.1	27.3 30.3 30.9	11.0	
25% d_{Large}	75-100% of largest diameters	61.9	64.0 73.2 86.2	78.9 82.7 103.9	44.1 53.5 83.8	40.9	
10% d_{Small}	0-10% of smallest diameters	31.8± 0.0	40.8± 1.2	31.0± 0.0	27.3± 0.0	11.0± 0.0	28.4±10.9
10% d_{Large}	90-100% of largest diameters	61.9± 0.0	79.7± 9.2	103.9 ±0.0	83.8± 0.0	40.9± 0.0	74.0±23.8
25% d_{Small}	0-25% of smallest diameters	31.8± 0.0	41.6± 1.7	31.9± 1.1	29.5± 1.9	11.0± 0.0	29.1±11.2
25% d_{Large}	75-100% of largest diameters	61.9± 0.0	74.5± 11.2	88.5± 13.5	60.4± 20.8	40.9± 0.0	59.2±23.3
Mean	Average diameters	47.0± 15.1	54.3± 14.6	56.7± 26.7	41.6± 16.7	27.0± 12.2	45.3±11.9
Total	Average of the N diameters	48.1±19.8					

Table 2.14: Diameter (small, mean, large) measurements based on Means of means from Table 2.10 and 2.11. Data are Mean±SD.

Bin	Diameter (µm)		Mean Diameter (µm)	
	NL	OA	NL	OA
10% Small	27 ± 12	28 ± 11	27 ± 0.0	29 ± 0.5
25% Small	27 ± 11	29 ± 11		
Mean	35 ± 10	45 ± 12	35 ± 10	45 ± 12
10% Large	46 ± 13	74 ± 24	46 ± 0.0	67 ± 11
25% Large	46 ± 14	59 ± 23		

Table 2.15: Number of channels used for spacing analysis for each sample

Sample ID (NL)	N
PPG11-016	6
PPG14-002n	2
PPG14-056n	2
Sample ID (OA)	
WDB414	7
WDB575	7
WDB635	8
WDB422	4

Table 2.16: Color-coded spacing measurements between NL vascular channels. The colors indicate the different distribution of the canal diameters.

Sample ID (NL)	Spacing (μm)					N _{sp}
PPG14-002n	602					1
PPG14-056n	809					1
PPG11-016		1	2	3	4	4
	1	0	380	359	961	
	2	380	0	463	1067	
	3	359	463	0	633	
	4	961	1067	633	0	







Small vs Small		Medium vs Medium	
Small vs Medium		Medium vs Large	
Small vs Large		Large vs Large	

Table 2.17: Color-coded spacing measurements between OA vascular channels.

Sample ID (OA)	Spacing (μm)									N _{sp}		
WDB414		1	2	5	6	7	9	10		7		
	1	0	365	457	362	339	262	544				
	2	365	0	297	373	525	203	204				
	5	365	297	0	637	740	454	258				
	6	362	373	637	0	211	184	566				
	7	339	525	740	211	0	324	728				
	9	262	203	454	184	324	0	405				
	10	544	204	258	566	728	405	0				
	WDB575		1	2	3	5	7	8	10			7
		1	0	762	355	430	258	389	764			
2		762	0	629	768	587	384	428				
3		355	629	0	155	455	391	828				
5		430	768	155	0	585	544	978				
7		258	587	455	585	0	214	512				
8		389	384	391	544	214	0	446				
10		764	428	828	978	512	446	0				
WDB635		L	1	3	4	5	7	8	9	10	8	
		1	0	504	465	320	66	543	279	251		
	3	504	0	205	207	540	268	619	285			
	4	465	205	0	278	481	454	484	216			
	5	320	207	278	0	360	278	493	171			
	7	66	540	481	360	0	598	229	270			
	8	543	268	454	278	598	0	752	429			
	9	279	619	484	493	229	752	0	339			
	10	251	285	216	171	270	429	339	0			
	WDB422		1	2	3	4						4
1		0	669	787	831							
2		669	0	395	519							
3		787	395	0	135							
4		831	519	135	0							

Table 2.18: Distribution of vascular canal diameter pairings based on the small, mean and large size of diameter in NL samples







VC diameter pairings (NL)	Number			
	PPG14-002n	PPG14-056n	PPG11-016	Total
Small-Small 	0	0	0	0
Small-Medium 	1	0	3	4
Small-Large 	0	0	0	0
Medium-Medium 	0	0	0	0
Medium-Large 	0	1	1	2
Large-Large 	0	0	0	0
Total	1	1	4	6

Table 2.19: Distribution of vascular canal diameter pairings based on the small, mean and large size of diameter in OA samples







VC diameter pairings (OA)	Number				
	WDB414	WDB575	WDB635	WDB422	Total
Small-Small 	0	0	3	2	5
Small-Medium 	0	1	5	2	8
Small-Large 	0	4	0	0	4
Medium-Medium 	4	0	0	0	4
Medium-Large 	3	0	0	0	3
Large-Large 	0	2	0	0	2
Total	7	7	8	4	26

Table 2.20: Spacing measurement based on lower and upper 10% values of nearest neighbors for individual samples, overall samples, and mean of means in NL samples

NL	Definition	PPG11-016	PPG14-002n	PPG14-056n
N	Number of nearest spaces	3	1	1
10% Sp_{Small}	0-10% of smallest Spacing	359 ± 0.0	--	--
10% Sp_{Large}	90-100% of largest Spacing	--	809 ± 0.0	--
Mean				602 ± 0.0
Total	Average of the total Spacing	590 ± 225		

Table 2.21: Spacing measurement based on lower and upper 10% values of nearest neighbors for individual samples, overall samples, and mean of means in OA samples

OA	Definition	WDB414	WDB57 5	WDB635	WDB42 2	Mean (µm)
N	Number of nearest spaces	7	7	8	4	
10% Sp_{Small}	0-10% of smallest Spacing	184	155	66	135	135±50
10% Sp_{Large}	90-100% of largest Spacing	262	428	268	669	407±191
Mean		215±32	258±108	173±73	255±334	225±40
Total	Average of the total Spacing	231±126				

Table 2.22: Spacing values to be used for simulations based on means of means from Tables 2.18 and 2.19

Bin	Spacing (μm)	
	NL	OA
Small	359 \pm 0.0	135 \pm 50
Mean	602 \pm 0.0	225 \pm 40
Large	809 \pm 0.0	407 \pm 191

Table 2.23: Values for parameters of interest for diameters and spacing in NL samples.

NL/ Parameter	Small (μm)	Medium (μm)	Large (μm)
Diameter	27	35	46
Spacing	359	602	809*

Table 2.24: Values for parameters of interest for diameters and spacing in OA samples

OA/ Parameter	Small (μm)	Medium (μm)	Large (μm)
Diameter	29	45	67
Spacing	135	225	407

2.7 Reference

1. Bonde HV, Talman ML, Kofoed H: The area of the tidemark in osteoarthritis--a three-dimensional stereological study in 21 patients. *APMIS* 113:349-52, 2005.
2. Burr DB, Gallant MA: Bone remodeling in osteoarthritis. *Nat Rev Rheumatol* 8:665-73, 2012.
3. Clark JM: The structure of vascular channels in the subchondral plate. *J Anat* 171:105-15, 1990.
4. Clark JM, Huber JD: The structure of the human subchondral plate. *J Bone Joint Surg Br* 72:866-73, 1990.
5. Goldring MB: Articular cartilage degradation in osteoarthritis. *HSS J* 8:7-9, 2012.
6. Goldring MB, Goldring SR: Articular cartilage and subchondral bone in the pathogenesis of osteoarthritis. *Ann N Y Acad Sci* 1192:230-7, 2010.
7. Goldring SR: Alterations in periarticular bone and cross talk between subchondral bone and articular cartilage in osteoarthritis. *Ther Adv Musculoskelet Dis* 4:249-58, 2012.
8. Goldring SR, Goldring MB: Changes in the osteochondral unit during osteoarthritis: structure, function and cartilage-bone crosstalk. *Nat Rev Rheumatol* 12:632-44, 2016.
9. Greenwald AS, Haynes DW: A pathway for nutrients from the medullary cavity to the articular cartilage of the human femoral head. *J Bone Joint Surg Br* 51:747-53, 1969.
10. Hwang J, Bae WC, Shieu W, Lewis CW, Bugbee WD, Sah RL: Increased hydraulic conductance of human articular cartilage and subchondral bone plate with progression of osteoarthritis. *Arthritis Rheum* 58:3831-42, 2008.
11. Imhof H, Breitenseher M, Kainberger F, Trattnig S: Degenerative joint disease: cartilage or vascular disease? *Skeletal Radiol* 26:398-403, 1997.
12. Lane LB, Bullough PG: Age-related changes in the thickness of the calcified zone and the number of tidemarks in adult human articular cartilage. *J Bone Joint Surg Br* 62:372-5, 1980.
13. Loeser RF, Goldring SR, Scanzello CR, Goldring MB: Osteoarthritis: a disease of the joint as an organ. *Arthritis Rheum* 64:1697-707 2012.
14. Mahjoub M, Berenbaum F, Houard X: Why subchondral bone in osteoarthritis? The importance of the cartilage bone interface in osteoarthritis. *Osteoporos Int* 23 Suppl 8:S841-6, 2012.

15. Oegema TR, Carpenter R, Hofmeister F, Thompson RC: The interaction of the zone of calcified cartilage and subchondral bone in osteoarthritis. *Microsc Res Tech* 37:324-32, 1997.
16. Oegema TR, Jr., Carpenter RJ, Hofmeister F, Thompson RC, Jr.: The interaction of the zone of calcified cartilage and subchondral bone in osteoarthritis. *Microsc Res Tech* 37:324-32, 1997.
17. Pan J, Wang B, Li W, Zhou X, Scherr T, Yang Y, Price C, Wang L: Elevated cross-talk between subchondral bone and cartilage in osteoarthritic joints. *Bone* 51:212-7, 2012.
18. Pesesse L, Sanchez C, Henrotin Y: Osteochondral plate angiogenesis: a new treatment target in osteoarthritis. *Joint Bone Spine* 78:144-9, 2011.
19. Shibakawa A, Yudoh K, Masuko-Hongo K, Kato T, Nishioka K, Nakamura H: The role of subchondral bone resorption pits in osteoarthritis: MMP production by cells derived from bone marrow. *Osteoarthritis Cartilage* 13:679-87, 2005.
20. Simkin PA: Consider the tidemark. *J Rheumatol* 39:890-2, 2012.
21. Suri S, Gill SE, Massena de Camin S, Wilson D, McWilliams DF, Walsh DA: Neurovascular invasion at the osteochondral junction and in osteophytes in osteoarthritis. *Ann Rheum Dis* 66:1423-8, 2007.
22. Suri S, Walsh DA: Osteochondral alterations in osteoarthritis. *Bone* 51:204-11, 2012.
23. Walsh DA, Bonnet CS, Turner EL, Wilson D, Situ M, McWilliams DF: Angiogenesis in the synovium and at the osteochondral junction in osteoarthritis. *Osteoarthritis Cartilage* 15:743-51, 2007.
24. Yuan XL, Meng HY, Wang YC, Peng J, Guo QY, Wang AY, Lu SB: Bone-cartilage interface crosstalk in osteoarthritis: potential pathways and future therapeutic strategies. *Osteoarthritis Cartilage* 22:1077-89, 2014.
25. Zhang LZ, Zheng HA, Jiang Y, Tu YH, Jiang PH, Yang AL: Mechanical and biological link between cartilage and subchondral bone in osteoarthritis. *Arthritis Care Res (Hoboken)* 64:960-7, 2012.

CHAPTER 3:

EFFECTS OF OPEN VASCULAR CANALS ON THE BIOMECHANICS OF THE DEEP ZONE OF ARTICULAR CARTILAGE

3.1 Abstract

Introduction.

Articular cartilage (AC) is an avascular biphasic tissue located at the end of the bones providing low friction movement of AC surfaces as well as high-velocity movement between bones. The interfacial SCP contains many vascular canals. Penetration of these canals through articular cartilage (AC) may affect the cartilage biomechanics and structure. The aim of this study is to determine the effect of the size of open vascular canals and their distribution in the subchondral bone plate on the temporal and spatial variations of stress-strain and depressurization maps of deep-zone cartilage. The hypothesis is that an increase of canal diameter as well as the decrease of the spacing between canals may affect the biomechanics of cartilage which may cause early calcification and damage to the cartilage at the deep zone.

Methods.

From the data obtained from **Chapter 2**, there are three “small”, “mean” and “large” diameters and spacing used to analyze cartilage biomechanics and cell mechanism around the canal entrance as well as along the spacing between the canals. There would be

five groups of canal diameter and spacing as extreme geometries to be simulated in ABAQUS. Then based on material properties obtained from pieces of literature for the deep zone of AC, we run a confined compression problem where cartilage behaves as a poroelastic material. For an axisymmetric problem, we will get stress-strain, fluid pressure, and flux at short, intermediate and infinite times. Finally, results will be compared to the ones obtained for a simple confined compression test where there is no canal underneath cartilage and the joint is a normal joint.

Results.

For each group of canal diameter and spacing, Stress-strain, depressurization and fluid flux maps are obtained and compared to the results obtained from the normal joint as a control case. Spatial variation of the results are presented at Three-time courses: short, intermediate and infinite times.

Discussion.

With the increase of canal diameter and a decrease of the spacing between canals at the interface of AC and ScP, depressurization decreases at different time courses. This depressurization may cause calcification of the deep zone of the cartilage over loading time. In addition to that, fluid flux increases with the decrease of canal diameter. With higher fluid flux, more proteoglycan fragments may be carried with the fluid through the canal entrance which may result in damage to the cartilage structure at the deep zone.

3.2 Introduction

Articular cartilage (AC) is an avascular biphasic tissue located at the end of the bones providing low friction movement to the AC surfaces as well as high-velocity movement between bones [32]. Structure and interstitial fluid pressurization enable a healthy AC to withstand the large forces associated with the joint motion and weight-bearing over the lifetime [40, 19, 29]. AC is separated from the zone of calcified cartilage (ZCC) by tidemark [19], an impenetrable barrier against the diffusion of water, marrow, and various ions. Beneath the calcified cartilage is the zone of the subchondral bone (SB). ZCC along with SB is considered as a subchondral plate (ScP), an interfacial zone between AC and trabecular bone (TB) which provides support for the forces applied on a synovial joint [44].

The interfacial SCP contains many vascular canals. Vascular canals contain marrow cells and blood vessels and invasion of them toward AC may contribute to the variation of cartilage micro environmental functions as well as chondrocyte viability [9, 33, 16, 20]. The frequency of these canals has been observed to be more significant in osteoarthritis joints and is expected to cause local loss of pressurization as well as stress-strain concentration through AC [39, 49]. Any effect on chondrocyte viability and mechanical biphasic behavior of AC may affect the load carriage mechanism across the cartilage especially in a region around the hole [2, 46, 52, 53].

Several experimental data have been offered to introduce some biphasic mechanical factors affecting cell metabolism and viability in cartilage under various loading boundary conditions (**Table 3.1**). The magnitude of the intra-tissue strains and stresses including compressive [28, 1, 12, 45, 50], shear [26] and principal strains [6] as well as compressive

stresses [22, 37] have implications for cells viability and injury through the articular cartilage. Moreover, the range of the time during which the stresses and strains are applied is involved in cartilage injury and chondrocyte viability [18, 30, 37, 51]. Impact loading and low strain rate may cause chondrocyte death [38]. In addition to the mechanical factors, biphasic criteria such as dehydration and fluid pressurization inside the cartilage may induce chondrocyte apoptosis [1, 18, 21, 34, 36, 37, 43].

To understand how the presence of vascular canals, their diameter and spacing influence the cells response and biphasic behavior of AC requires an understanding of various mechanical and biphasic criteria within AC according to the region of cartilage where a criterion is calculated. However, the distribution of various criteria within AC cannot be readily measured in experimental models due to some measurement limitations as well as the complexity of the model. Therefore numerical solutions are essential to provide a more complete understanding of the mechanics of synovial joints.

Many finite element models (FEMs) have been developed to study the biomechanical contact behavior of the synovial joint, either as single phase solid [17, 31] or biphasic [3, 25] contact problems. Shim et. al. [47] employed a multiscale framework to associate the effect of mechanical factors on the initiation of OA at the synovial joint. A whole continuum knee model was numerically linked to a model of cell mechanics. In their study, any abnormal mechanical loading environment of the knee influenced the von-mises cartilage strains and changed the micro architecture of the joint interface. In their model, the effect of fluid flow through the cartilage was neglected and cartilage was treated as a linear elastic material. Furthermore, invasion of the vascular canals toward the tidemark was not studied. Guo et al [23] conducted a numerical analysis to study the biomechanical

microenvironment of chondrocyte in articular cartilage under simple unconfined compression test[23]. It was found that the spatial locations of chondrocyte affected the biphasic mechanical factors such as axial, radial and maximum principal shear stresses as well as fluid pressure and fluid flow inside the cartilage [23].

Influence of the presence of vascular canals and their size variations at the interface of cartilage on fluid transport through the canal and stress distribution within cartilage around the hole has been studied under confined compression test by using numerical methods. Ayotte et. al. [4, 5] analyzed the effect of subchondral canal underneath the intervertebral cartilage region on fluid transportation and stress distribution within cartilage at the interface. A non-linear poroelastic material was confined in an impermeable chamber while a pressure was applied on the top free surface at a steady state condition. Buschmann et. al. [11] set up a compression test by controlling the displacement applied on the cartilage in the presence of a porous plate on the cartilage surface. Mow et. al. [39] studied the effect of the change of the ratio of the hole size with respect to the cartilage thickness on stress distribution within cartilage at the top of the hole underneath cartilage by controlling the pressure applied on the cartilage surface. In these models, there was no specific study regarding the effect of subchondral canals and spacing on the local biphasic properties of cartilage at deep zone based on cartilage material properties and real sizes of cartilage and vascular canals.

The objective of this study was to investigate the effect of the subchondral canals at the interface of cartilage and bone and their distribution on local biphasic and mechanical behavior of articular cartilage and evaluate cells viability and metabolism through the cartilage in radially confined compression. In this study, an axisymmetric model of the

synovial joint including cartilage as a nonlinear poroelastic material, and a subchondral canal underneath is analyzed for five different groups as well as one normal group (as a control group). Since the subchondral plate is much stiffer than cartilage, it is assumed to be a rigid body. Due to the complexity of the geometry as well as limitations of analytical models for evaluating spatial variation of different mechanical properties through cartilage, we employ ABAQUS software to simulate our axisymmetric model.

We hypothesize that change of vascular canal size, as well as the spacing between the canals, will affect the local mechanical and biphasic behavior of articular cartilage around the canal as well as the deep zone of the cartilage within the space between the canals. In addition to that, there would be some possible mechanical-biphasic quantities evaluated through cartilage especially in the neighborhood of the canal, which may be estimated as the reasons for cartilage degradation. Based on the data measured by previous experiments and under various loading boundary conditions, there are critical values for different criteria which cause to affect cartilage degradation and consequently. The quantities obtained by this study can be compared with the related critical ones in order to predict the region where undergoes any degradation.

In this study, numerical simulations of the hydrated cartilage were carried out using ABAQUS which is based on soils mechanics. It has been established that soils mechanics is equivalent to conventional biphasic theory [8, 10, 48].

3.3 Materials and Methods

3.3.1 Study design

Based on the vascular canal simplification for normal (NL) and osteoarthritis (OA) samples, there are two significant appearances of the joint as shown in **Fig. 3.1**, for NL and OA cases. In the NL case, it was assumed that the presence of the vascular canal underneath TM would not affect the biomechanics of cartilage because the stiffness of CC and ScB is much higher than that of cartilage. According to the data from **Chapter 2** for three “small”, “mean” and “large” diameters and spacing, five different groups are modeled and the results are compared with those of NL group in which there is no vascular canal underneath cartilage. As shown in **Table 3.2**, five groups are chosen from the data obtained from OA samples as five generic groups: group 1: small versus small diameter with large spacing, group 2: large versus large diameter with small spacing, group 3: medium versus medium diameter with small spacing, group 4: medium versus medium diameter with medium spacing, and group 5: medium versus medium diameter with large spacing. Group 6 represents the normal joint with no open canal underneath cartilage (**Fig. 3.1.A**). A confined compression test under pressure control has been applied using the axisymmetric model to evaluate stress-strain and fluid pressure and flux through the cartilage.

3.3.2 Assumptions

There are some assumptions made in order to simplify the problem and be able to simulate it. First, According to **Fig. 3.2**, the undulation of TM and CL has been ignored due to the complexity of the geometry of the joint. Second, the area above TM1 is

considered as AC although in OA cases, multiple TMs are observed in the deep zone. However, the area between two TMs is considered as AC. Third, the area underneath TM1 is considered as a bone as a rigid body, since its stiffness is much greater than that of AC. Fourth, material properties of articular cartilage are assumed to be the ones corresponded to the deep zone. Fifth, Liquid and solid phases are assumed to be incompressible. Sixth, a nonlinear poroelastic model has been adopted for cartilage under small strain, since the deep zone of cartilage has shown to have a strain at most 5%. Seventh, Axisymmetric geometry has been chosen for the geometry since we have assumed that diameter and spacing distribution is uniform along the interface.

3.3.3 Schematics of confined compression test

Fig. 3.3 outlines the schematics of the confined compression test for evaluating the cartilage biomechanics at deep zone either around the vascular canal or along the spacing between canals. A cylindrical core of synovial joint (**Fig. 3.3a**) including a number of subchondral canals was placed into the confining impermeable chamber with the ScB on the bottom surface of the chamber (**Fig. 3.3c**). The top surface of the cartilage and the bottom surface at the entrance of the canal, are in contact with water. A pressure of P_0 was applied on the surface of the cartilage for a very short time, $t = t_1$ (**Fig. 3.3b, d and e**) and then kept fixed for a long time, $t = t_{inf}$ (**Fig. 3.3f and g**). According to **Fig. 3.3**, it has been assumed that canal diameters and distribution are consistent. In order to analyze the effect of different mechanical biphasic quantities on the microenvironment of the cartilage around the vascular canal, it is necessary to employ numerical approximations of the geometry.

Fig. 3.4 shows the schematics of the synovial joint which is supposed to be modeled in ABAQUS. **Fig. 3.4.a** is the magnified image of the red dashed square from **Fig. 3.3.c**, including AC and ScB. The spacing between the canal centers and half of the diameters of the canals are represented by SP_{CH} and R_{CH} respectively. Since the canal diameters are assumed to be equal for all canals, half of this space has been taken and the geometry of the joint is modeled as an axisymmetric geometry (**Fig. 3.4.b**). The results from five groups would be compared to those obtained from control geometry. In control geometry the interface is normal and there is no open canal underneath AC (**Fig. 3.4c**). In all models, the thickness of AC is 2.4 mm while the thickness of ScB is considered as 0.36mm.

3.3.4 Material properties

Material properties of AC during simulation is set to be those corresponded to the deep zone of human AC (**Table 3.3**). The homogeneous compressive aggregate modulus (H_A) of AC is about 3MPa [14]. However, the modulus related to the deep zone is about 9 MPa [14]. Poisson's ratio of the deep zone of cartilage, ν was set to be 0.25. Cartilage is an inhomogeneous, anisotropic having nonlinear tension-compression behavior [54, 15] [13]. However, under small strain, we can have a homogeneous Poisson's ratio especially for deep zone [27, 54]. To enable simulation of the dynamics of compaction, hydraulic permeability, \tilde{k}_0 , was set to be appropriate for the deep zone of cartilage equal to $1.5 \times 10^{-16} \text{ m}^2/\text{MPa.s}$ [35]. About 75% of the deep zone of cartilage is water. Therefore, the void ratio, n which is defined as the ratio of the fluid volume respect to the solid volume is set to be 3. To input the material properties of AC into ABAQUS, presentation of the

properties are different based on their units (**Table 3.4**). In this study, AC is represented by a solid phase as a hyperplastic material having permeability. Neo-Hookean model has been considered for modeling cartilage. Due to the time cost during simulation, the problem has been run for 40 (s). To get the results corresponded to the equilibrium time, in order to decrease the time cost, we use a compressible hyperelastic material having only confined aggregate modulus, H_A and equilibrium Poisson's ratio, ν . In fact, in a very large time, only solid phase but fluid carries the whole pressure. Thus, we can model cartilage as either porohyperelastic material with a very high permeability or hyperelastic material. ScB is much stiffer than AC and assumed to be a rigid body with no deformation during simulation.

3.3.5 Initial and boundary conditions

Cartilage-bone unit shown in **Fig. 3.3c** is initially assumed to be saturated in water under no displacement and loading boundary condition. The connections of the cartilage with the wall of the chamber are modeled by imposing rollers to confine the displacement of the cartilage in r-direction (**Fig. 3.4**). The bottom surface of the cartilage is bonded to an impermeable subchondral bone. Therefore, the cartilage-bone interface contact has been modeled as a tie contact ($R_{CH} < r < SP_{CH}/2$). However, the bottom surface of the cartilage which is not initially in contact with the bone is considered to be permeable ($r < R_{CH}$). The top surface of the cartilage where the pressure is applied has been considered to be permeable.

In the current simulation, the mechanical properties of cartilage are chosen based on a confined compression test and for a homogeneous cartilage (compressive modulus and hydraulic permeability). Therefore, the application of the stress in simulated confined compression of cartilage, initially at zero strain, would provide a reasonable simulation of the dynamics and equilibrium behavior of deep zone of articular cartilage, where fluid exudation (and resulting compressive strain) occurs. First, the equilibrium compressive strain of full-thickness articular cartilage was noted to be 20%, based on the in-vivo biomechanical studies of the human knee [24]. Assuming that the cartilage compaction had reached equilibrium under such whole joint loading, the cartilage depth-dependent modulus results in local (depth-dependent) strain that is 6% of that overall strain [14, 24]. Therefore, the compressive strain in the deep 1/6 of cartilage was targeted as 7%. To achieve such compaction at equilibrium, the confined compression modulus of the deep zone of cartilage, H_A , is set to be 9 MPa, assuming an overall compressive modulus of 3 MPa, with corresponding applied (time-averaged) compressive stress of $P_0 = 0.6$ MPa.

A pressure history is prescribed as shown in **Fig. 3.3b**. A total pressure of $P_0 = 0.6$ Mpa is applied on the top surface of the cartilage within a short time $t = t_1$ and then kept fixed for a long time ($t = t_{inf}$). The short and equilibrium times are defined based on the characteristic time (diffusion time), τ . Based on the geometries and material properties of the cartilage, characteristic time is defined as $\tau = \frac{L^2}{H_A \bar{k}}$, where L is the length of the interest corresponded to the canal size, spacing or cartilage thickness and bottom part includes the material properties of cartilage from **Table 3.3**.

According to **Table 3.2**, there are different characteristic times defined for the problem (**Table 3.5**). In all of them, material properties are the same. To be consistent in time coursing for all groups of simulations, there are three different time courses at which the results are evaluated: $t=t_1=0.001(s)$ (short time much less than the mean of the characteristic time based on the canal diameter), $t= t_2= 12(s)$ (intermediate time determined by the average of the means of characteristic times of the diameter and spacing), and $t= t_{inf}$, the time much higher than the one based on cartilage height (**Table 3.6**).

3.3.6 Equations used in ABAQUS

In this study, cartilage was treated as a homogeneous and isotropic nonlinear poroelastic material containing incompressible solvent (here it is water) and solid porous phase [41, 42]. The solid phase of cartilage is set to be hyperelastic employing Neo-Hookean model having the strain energy density given in ABAQUS as follows:

$$U = C_{10}(\bar{I}_1 - 3) + \frac{1}{D_1}(J_{el} - 1)^2, \quad (1)$$

$C_{10} = \frac{G}{2}$, where G is the short time shear modulus of the tissue (**Table 3.4**), $D_1 = \frac{2}{K}$, where K is the equilibrium bulk modulus of the tissue. \bar{I}_1 is the first invariant of the isochoric part of the right Cauchy-Green deformation tensor, and J_{el} is the elastic volume ratio. In ABAQUS, the total Cauchy stress matrix acting at a point for the completely saturated biphasic porous cartilage takes the following form:

$$[\sigma] = [\sigma^m] - \Delta p[I], \quad (2)$$

where $[\sigma^m]$ is the effective stress which is referred to the stress in the solid phase, Δp represents the change of pore pressure of the fluid inside the porous material with respect

to the reference state, and $[I]$ is the unit matrix. All variables have been defined in **Table 3.7** as well.

To govern the fluid flow in the porous media under a uniform condition, Darcy's law is employed where the volumetric flow rate of the fluid through a unit area of the cartilage, f , is proportional to the negative of the gradient of the pressure [7]:

$$\vec{f} = n\vec{V}_w = -k \frac{\nabla p}{\rho g}, \quad (3)$$

Where n is the void ratio (volume of the pores respect to the volume of the solid phase), $V_w \left(\frac{m}{s}\right)$ is the average velocity of the fluid relative to the solid phase (seepage velocity), and $k \left(\frac{m}{s}\right)$ is the hydraulic conductivity of the material, which is an input parameter in ABAQUS and is related to the permeability of the cartilage by $\left(\frac{m}{s}\right) = \tilde{k} \left(\frac{m^4}{Ns}\right) \gamma_w \left(\frac{N}{m^3}\right)$, where $\gamma_w = \rho g$, is the specific weight of fluid.

3.3.7 Define the contact between cartilage and bone in ABAQUS

Cartilage interface with bone: cartilage is bounded to the bone and there is a “tie” contact between them. Bottom surface of the cartilage in contact with water and channel wall is a frictionless surface (frictional coefficient of the cartilage is about 0.001), Hard contact (the “hard” contact relationship minimizes the penetration of the slave surface into the master surface at the constraint locations and does not allow the transfer of tensile stress across the interface).

3.4 Results

3.4.1 Effect of diameter of vascular canal on the biomechanics of articular cartilage

Change of the diameter of the vascular canal (VC) is expected to affect the biomechanics of the articular cartilage at the deep zone, significantly around the canal. **Figs. 3.5 and 3.6** illustrate the effect of an increase of the VC diameter with the same spacing, on pore pressure, maximum and minimum strains within the cartilage along path P1 on the top right schematics. To illuminate the edge effects at the interface of cartilage and bone, path P1 is chosen to be $4\mu\text{m}$ above the interface. The r axis is in logarithmic scale in order to express the biomechanics of cartilage within a small area around the canal. The tables underneath each figure represent three groups to be compared: NL or control group (green color), first (blue color) and fifth group (magenta color) groups. The results are presented for three different time periods: short time ($t=0.001$ s), intermediate time ($t=12$ s) and long time ($t=\infty$).

At $t=t_1$, under pressure of $P_0=0.6$ MPa applied on the surface of cartilage, fluid pressure is homogeneous along path P1 for NL group because cartilage undergoes simple confined compression and pore pressure along path P1 is equal P_0 (solid green line) (**Fig. 3.5**). Under this boundary condition, maximum principal strain (ϵ_{max}) is zero (**Fig. 3.6**). With the increase of the diameter of the VC, pore pressure decays especially around the canal. Due to loading, cartilage bulges out of the VC and ϵ_{max} increases, while ϵ_{min} is close to zero. At the VC corner, due to the edge effect, there is a jump in pore pressure and strains subsequently. Far from the VC hole, pore pressure and strain become more homogeneous equal to the ones of the NL group.

At $t=t_2=12$ s as an intermediate time, pore pressure decays and ε_{max} decreases around the VC, while ε_{min} is still closed to zero (dashed lines **Figs. 3.5** and **3.6**) in results are shown with the dashed line for three different groups (**Figs. 3.5** and **3.6**). However, for the NL group, the results overlapped the ones from $t=t_1$.

At a very long time ($t = \infty$) with respect to the characteristic times, there is no pore pressure within the cartilage anymore and highest value of ε_{min} is corresponded to the NL group.

3.4.2 Effect of the spacing between vascular canals on the biomechanics of articular cartilage

Effect of spacing for two different groups containing the same size diameter (group 3, medium versus medium diameter with small spacing, and group 5, medium versus medium diameter with large spacing) on the biomechanics of cartilage at the deep zone has been compared and the results are evaluated with respect to the ones obtained for the NL group. According to **Fig. 3.7**, similar to the schematics of the figures of **section 3.4.1**, the mechanical and biphasic variables are evaluated along path P1, 4 μm above the interface of cartilage and bone.

At $t= t_1$, pore pressure decays with the decrease of the spacing between canals (**Fig. 3.7**, left side graph, solid line). At the same time, the absolute value of the minimum principal stress, σ_{min} , applied on the solid phase increases. However for NL group with no canal underneath cartilage, at this short time pore pressure is homogeneous and equal to the pressure applied on the cartilage. Therefore, there is no principal stress within the solid phase at this time.

Over time of the creep, pore pressure decays within cartilage until it becomes zero. There is a jump observed in the pore pressure and min principal stress graphs due to the stress concentration at the corner of the canal. At equilibrium ($t=\infty$) the highest value of stress is applied on the solid phase of the cartilage since no load is carried with fluid within cartilage anymore.

3.4.3 Temporal variation of the total vertical fluid flux

Temporal variation of the total vertical fluid flux through the free surface of cartilage at the interface of the cartilage and subchondral bone has been evaluated in **Fig. 3.8** for five OA groups and one NL group. As shown in the schematics of the cartilage and bone, this evaluation has been analyzed along the red line at the interface. The time axis is scaled based on the logarithmic time. From $t=0$ to $t=0.001$ (s) (short time), with the increase of the diameter of the canal, the total vertical flux will increase (negative sign indicates the downward direction of fluid). As shown in the table underneath **Fig. 3.8**, the largest diameter of the canal belongs to group 2 (G2). Over time of the creep, pore pressure decays and fluid flux decreases. Since the fluid flux is evaluated along the canal opening, change of spacing does not show any significant effect on the fluid flux.

Contour plots shown in **Figs. 3.9** and **3.10** represent the effect of the change of diameter and spacing on the biomechanics of cartilage at the deep zone respectively. Since the biomechanics of the cartilage is more significant around the canal, a rectangle contour has been chosen around the canal. In **Fig. 3.9**, the contour plot has been shown for a rectangle around the canal with the height of $30\ \mu\text{m}$ and the width of $50\ \mu\text{m}$ and the results are compared among group1 (G1), group5 (G5) and the control group (G6), while in **Fig.**

3.10, the height of the rectangle is 20 μm and the contour is represented along the whole width of cartilage in order to evaluate the effect of spacing on the pore pressure and strain within cartilage. Contour plots are shown only for half of the geometry of the cartilage due to the axisymmetric model. As shown in **Fig. 3.9**, with the increase in canal size, fluid depressurization occurs earlier. At $t = t_1$, maximum principal strain occurs above the canal entrance. Over time of the creep, zero pore pressure spreads through the cartilage and maximum principal strain decays within the cartilage around the canal. Finally, at equilibrium time, the cartilage becomes in equilibrium and pore pressure equals zero. As shown in **Fig. 3.9**, max principal strain becomes negative meaning that at equilibrium, the maximum principal strain is a compressive strain. In **Fig. 3.10**, pore pressure and minimum principal strain have been compared for three different groups: group 3 (G3), group 5 (G5) in which the diameters of the canal are the same and equal to 45 μm , and group 6 (G6) as a control group. As shown in **Fig. 3.10A**, with the decrease of space between the canals (G3), depressurization and increase in absolute value of min principal strain along cartilage width at deep zone occur earlier.

3.5 Discussion

The results of FEM analysis support the hypothesis that the change of the canal diameter, as well as the spacing between the canals penetrated through subchondral bone and underneath articular cartilage, plays an important role in the fluid depressurization within the cartilage and increase of stress-strain applied on the solid phase of cartilage. In fact, with the increase of the diameters of the canals and decrease of the spacing between them, fluid pressure (pore pressure) within cartilage, especially at the deep zone, decays.

These results are consistent with the ones obtained due to the increase of the size of the permeable boundary in which earlier fluid depressurization occurs over loading time.

In this study, to simulate the evolution of pore pressure and stress/strain field within the cartilage and under confined compression test, a non-linear poroelastic material behavior was defined in ABAQUS for articular cartilage matrix. The saturated synovial joint sample was confined in a non-porous chamber and subjected to a load controlled creep test (**Fig. 3.2**). Since it was assumed that the canal distribution underneath cartilage was uniform, an axisymmetric geometry was modeled (**Fig. 3.3**). According to the results obtained from **Chapter 3** for extreme size of canals and the spacing between them, five different groups of geometries based on the canal diameter and spacing were identified. The results were compared with those of synovial joint geometry with no canal underneath, as a control group.

Material properties of cartilage were defined based on the data obtained from experimental tests. Poisson's ratio, ν , the ability of cartilage to imbibe additional solvent in response to the loading was defined under an equilibrium condition. Equilibrium confined compression modulus, H_A , and hydraulic permeability, \tilde{k}_0 , were the homogenous parameters corresponded to the deep zone of the cartilage and under confined compression test. In this study since the length of the cartilage was much larger than the size of the canals and the spacing between them, fluid diffusion around the canal and along the width of the cartilage occurs much faster than within the thickness of cartilage. Thus, the material properties of the deep zone of cartilage is assumed to be the homogeneous properties of the whole thickness of the cartilage and depth independent properties did not affect the biomechanical results significantly.

The increase of the canal diameter resulted in decreasing pore pressure within cartilage at the deep zone, especially around the canal entrance. This result was confirmed with the previous studies in which, an increase of the canal size reduced the resistance to the fluid flow [4, 5, 39]. Group1 (G1) and group5 (G5) in which the spacing between canals was the same, were chosen. Pore pressure reached its peak at the short time, t_1 (**Figs.3.5 and 3.9**) since at this time the maximum pressure was applied on the surface of the cartilage and there was no time for fluid to exude from the cartilage into the canal. Thus, the total load was carried by the fluid ($p=0.6$ MPa). However, over the time of the creep, more fluid came out of the canal. Exudation of the fluid from the cartilage may result in cartilage damage due to the excessive load applied on the solid phase and lack of nutrients through cartilage. At the canal entrance, cartilage bulged out of the hole and maximum and minimum principal strain occurs within the cartilage and around the canal which their absolute value decreases by increasing the canal size (**Figs.3.6 and 3.9**).

A decrease of the spacing between the canals resulted in early fluid depressurization over the time of loading (**Figs. 3.7 and 3.10**). Two groups of joint geometries with the same diameters and small (G3) and large (G5) spacing were analyzed and the results were compared to those of NL samples. In fact, an increase of the frequency of the canal underneath the cartilage changes the interface boundary condition (BC) to a porous platen one and increases the load carried by the solid works of cartilage [11], not only at the deep zone but also within the thickness of cartilage. Under porous platen BC, the characteristic time defined based on the thickness of the cartilage is reduced to a quarter of the original one because of the geometry symmetry with respect to the middle of the cartilage thickness.

With the increase of the spacing between canals, the mechanical response of the sample becomes close to that of NL sample.

Cell metabolism and cartilage degeneration at the deep zone of articular cartilage under compression is time-dependent. Although, pore pressure decays over the time of loading, stress-strain fields fluctuate within the cartilage. As shown in **Fig. 3.9**, just above and in the center of the canal penetration, the maximum principal strain is positive at a short time. However, over the time of loading, it turned negative. The peaks of stress-strain fields may change according to the BCs and depth-dependent variation of cartilage material properties (**Table 3.1**) and depending on what mechanical or biphasic quantities are of the interest as criteria of cartilage damage and cell viability. According to the temporal variation of the vertical flux of the solvent at the interface of cartilage and bone, the group of large-large diameter and small spacing (G2, **Fig. 3.8**) includes the extreme geometry in which maximum volume of the solvent exudes from the cartilage into the canal which may result in more cartilage calcification and cell apoptosis.

In conclusion, the results of the quantitative FE model demonstrates that with the increase of the diameter of the canals reaching articular cartilage at the interface of the cartilage and bone, and decrease of the spacing between canals results in early depressurization within cartilage at the deep zone and transformation of the applied pressure to the solid phase of the cartilage. Furthermore, carrying more solvent from cartilage into the canal as a result of increasing the size of the canal may result in a lack of nutrition within the cartilage and cartilage degeneration. With the increase of the frequency of the canals at the interface which may be due to a higher degree of osteoarthritis (OA), the interface of cartilage and bone boundary condition may change to a porous platen which

results to early equilibrium along the thickness of cartilage as well. Thus, not only the deep zone of cartilage undergoes degeneration, the thickness of cartilage also would be damaged. This study reveals that due to the vascular canal invasion developed by osteoarthritis, cartilage degeneration and cell damage may occur within cartilage.

3.6 Acknowledgment

Chapter 3, in full, is being prepared for submission to *Journal of Biomechanics*.

The dissertation author is the primary investigator and thanks co-authors Dr. Shengqiang Cai, Dr. Robert L.Sah., and Dr. Albert Chen for their contributions.

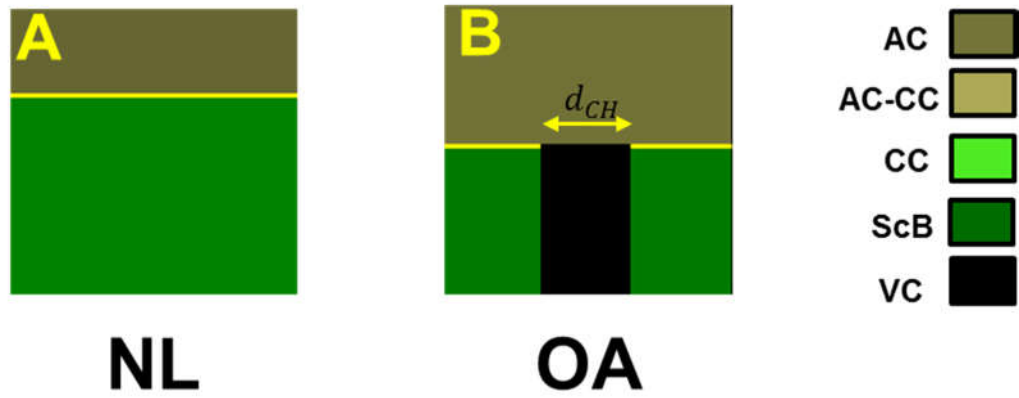


Figure 3.1: Two schematics representing types of simplified vascular channels: A. NL osteochondral joint and B. OA osteochondral joint including an open channel underneath the cartilage

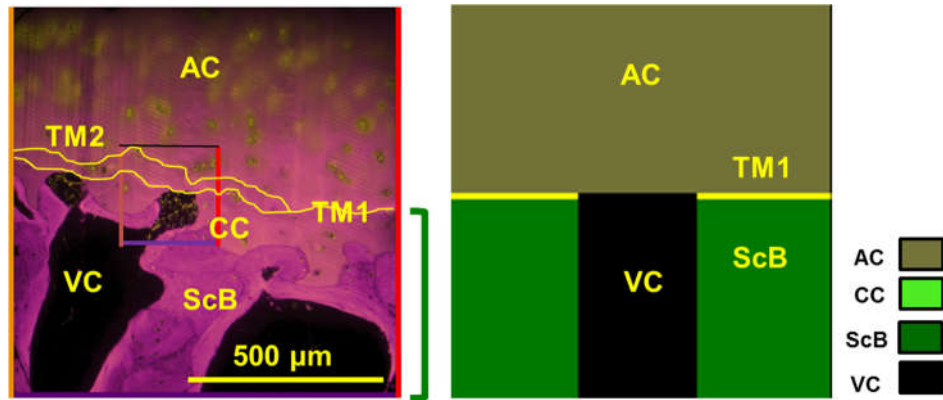


Figure 3.2: Various structural assumptions made through the joint in order to simulate the problem: 1- no undulation along the first TM, 2- the area between two TMs is considered as articular cartilage (AC), 3- the vascular canals ending at or penetrating through cartilage are considered as canals ended at TM, 4- calcified cartilage (CC) and subchondral bone (ScB) together form ScB, 5- vascular canal is vertical.

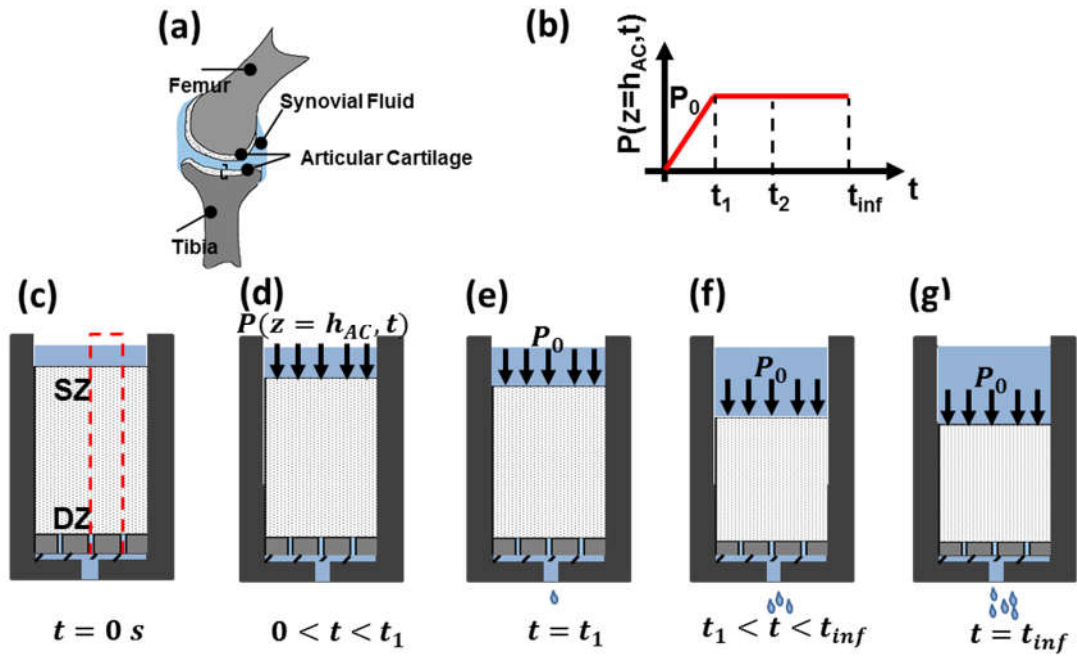


Figure 3.3: Schematics of confined compression test done on OA osteochondral joint. a. a macroscale representation of femoral-tibial joint. b. the loading path applied on the surface of AC. c. joint confinement in an impermeable chamber initially in equilibrium. d. apply a pressure, $P(t)$ on the surface of the cartilage with the path shown in panel (b). e. fix the value of the pressure at $t = t_1$. f. keep the pressure value fixed for the time $t_1 < t < t_{inf}$. g. pressure is applied until $t = t_{inf}$.

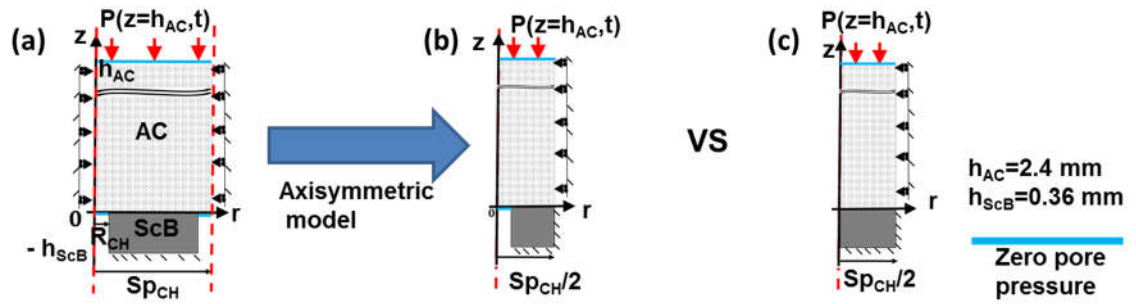
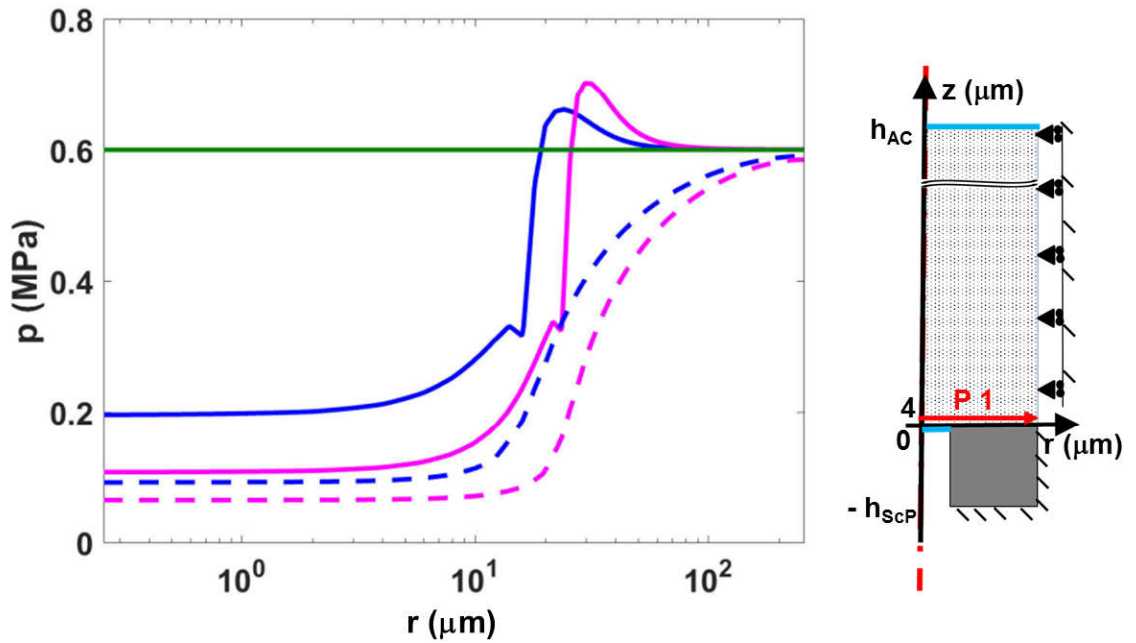
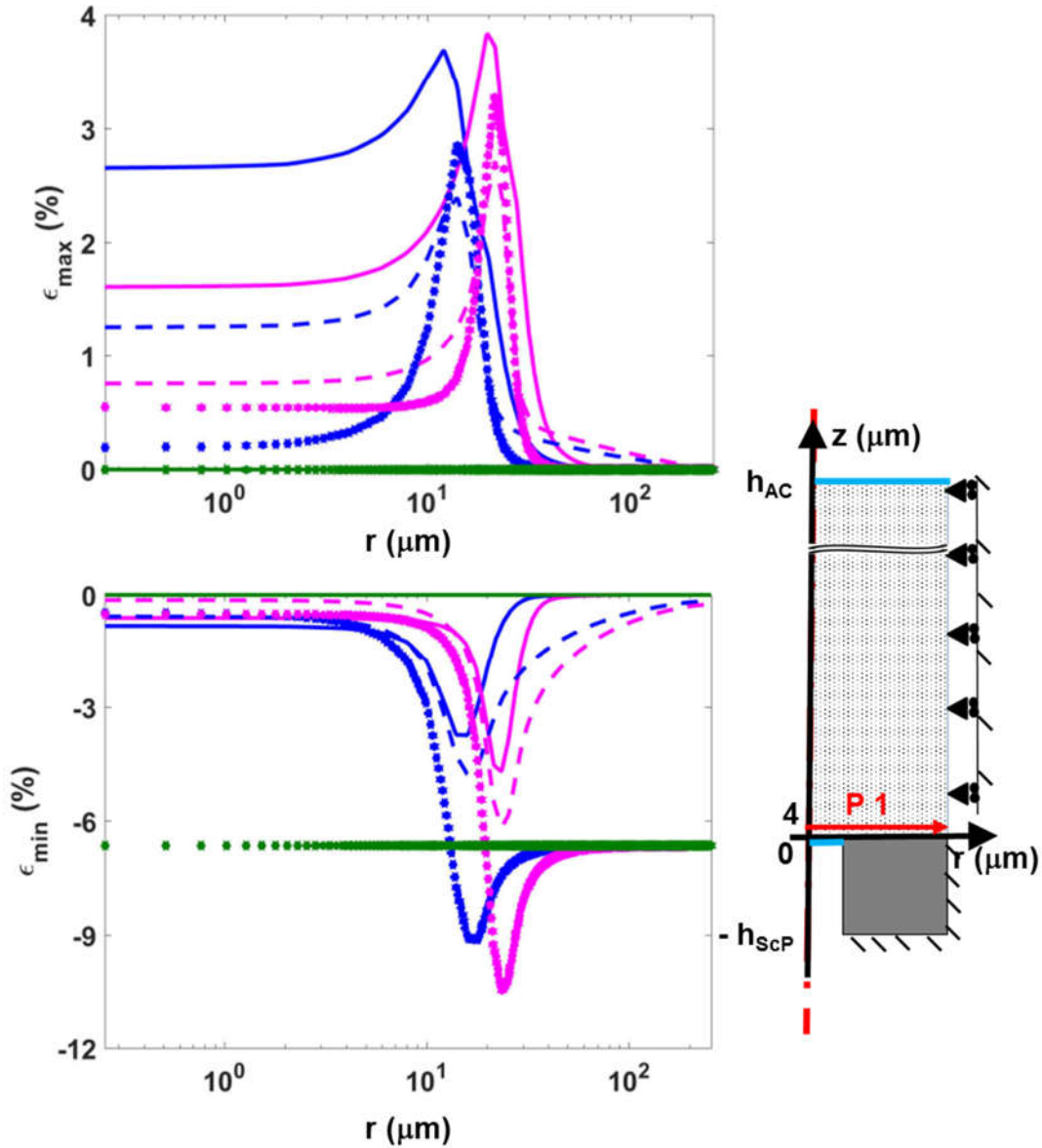


Figure 3.4: Schematics of the axisymmetric model in ABAQUS. a. cropped part from a dashed rectangle in Fig. 3.3c. b. an axisymmetric model representing half of the schematics of the panel (a). c. Control model with no canal underneath AC



Group	$d_{CH}/2$ (μm)	$Sp/2$ (μm)	Color	t	Value (sec)	Marker
6 (NL)	0	--	 	t_1	0.001	—
1	15-15 (S-S)	256 (L)	 	t_2	12	- -
5	22.5-22.5 (M-M)	256 (L)	 	t_{inf}	∞	*

Figure 3.5: effect of diameter change on the special variation of pore pressure along r direction at $z=4\mu\text{m}$. A special variation of pore pressure is shown along path P1 on the schematics for two groups (group 1, blue color and group 5, magenta color) having the same spacing (large spacing, $512\mu\text{m}$) and the results are compared with the ones of normal group (green color). Solid lines, dashed lines and star lines represent the short time ($t = 0.001$ (s)), intermediate time ($t=12$ (s)) and infinite time ($t=\infty$).



Group	$d_{CH}/2$ (μm)	$Sp/2$ (μm)	Color
6 (NL)	0	--	Green
1	15-15 (S-S)	256 (L)	Blue
5	22.5-22.5 (M-M)	256 (L)	Magenta

t	Value (sec)	Marker
t_1	0.001	—
t_2	12	- -
t_{inf}	∞	*

Figure 3.6: Effect of diameter change on the special variation of max and min principal strains (ϵ_{max} and ϵ_{min}) along r direction at $z=4\mu\text{m}$. Special variation of principal strains is shown along path P1 on the schematics for two groups (group 1, blue color and group 5, magenta color) having the same spacing (large spacing, $512\mu\text{m}$) and the results is compared with the ones of normal group (green color). Solid lines, dashed lines and star lines represent the short time ($t = 0.001$ (s)), intermediate time ($t=12$ (s)) and infinite time ($t=\infty$).

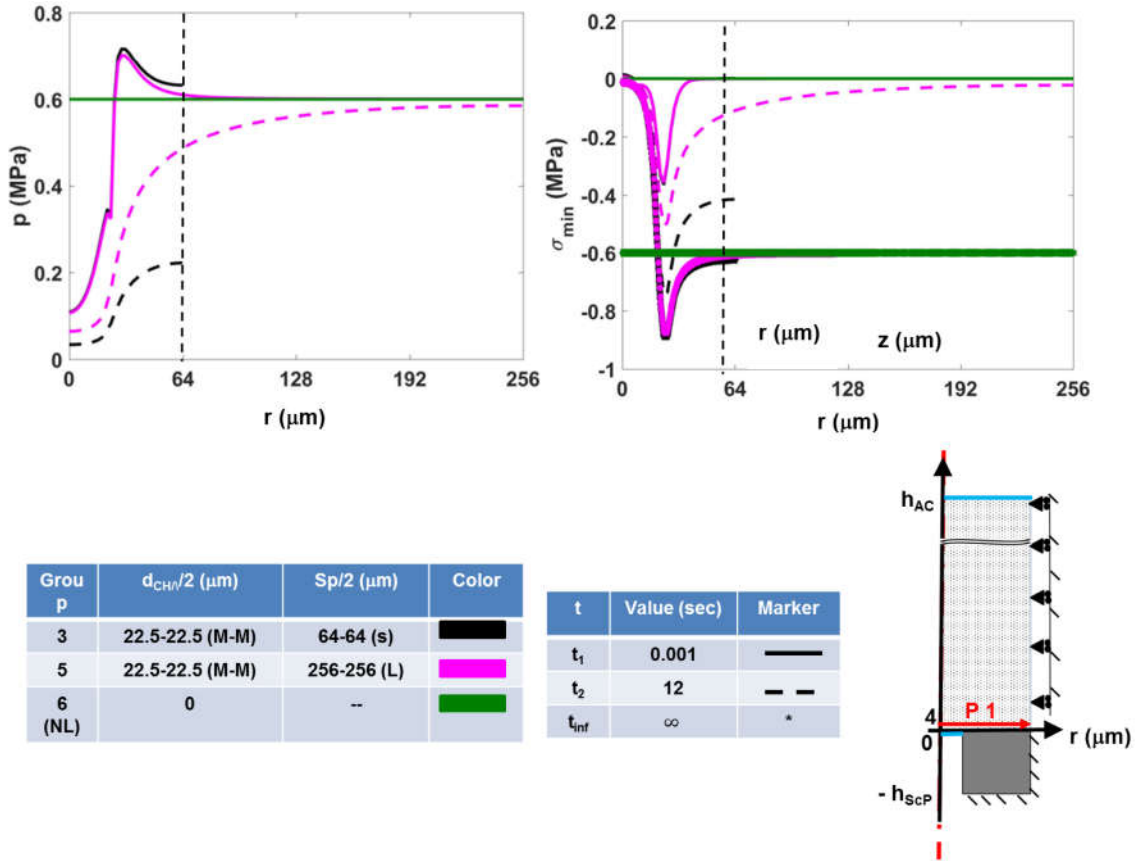
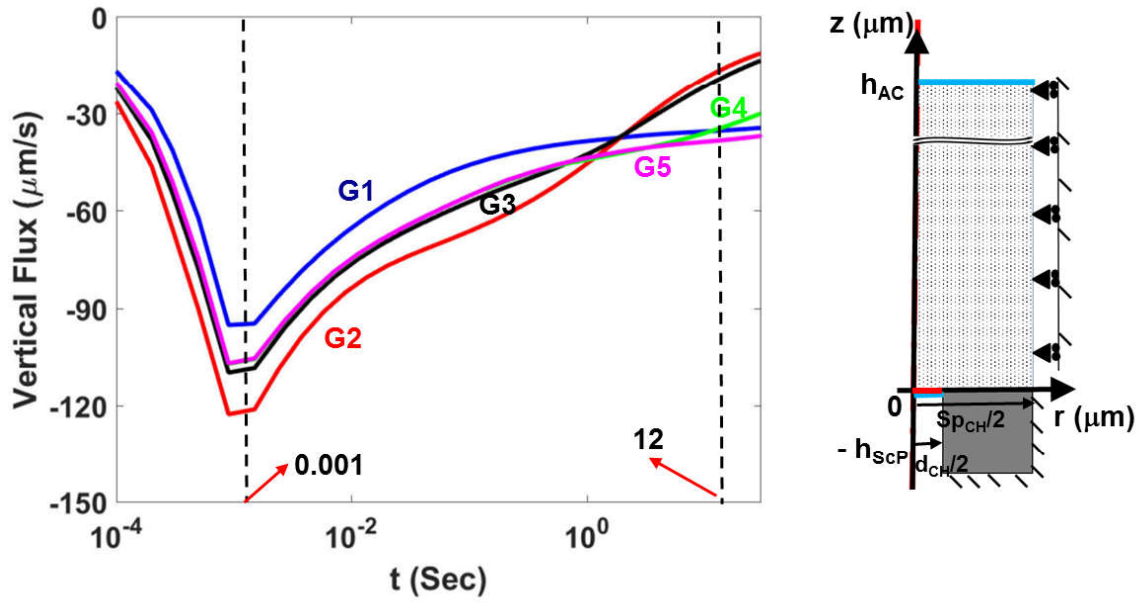


Figure 3.7: Effect of spacing on the special variation of pore pressure (P) and min principal stress applied on a solid phase (σ_{min}) along r direction at $z=4\mu\text{m}$. Special variation is shown along path P1 on the schematics for two groups (group 1, blue color and group 5, magenta color) having the same diameter (Medium diameter, $45\mu\text{m}$) and the results is compared with the ones of normal group (green color). Solid lines, dashed lines and star lines represent the short time ($t = 0.001$ (s)), intermediate time ($t=12$ (s)) and infinite time ($t=\infty$).



Group	VC diameter (mm)	VC spacing (mm)
1	Small-Small (30-30)	Large (512)
2	Large-Large (60-60)	Small (128)
3	Medium-Medium (45-45)	Small (128)
4	Medium-Medium (45-45)	Medium (256)
5	Medium-Medium (45-45)	Large (512)

Figure 3.8: Temporal variation of vertical flux along the free surface of cartilage at the top of the vascular canal (red line on the schematics). Results have been graphed for five different groups for a time period of 30 (s). Short and intermediate times are represented by vertical black dashed lines, $t=0.001$ and 12 (s) respectively.

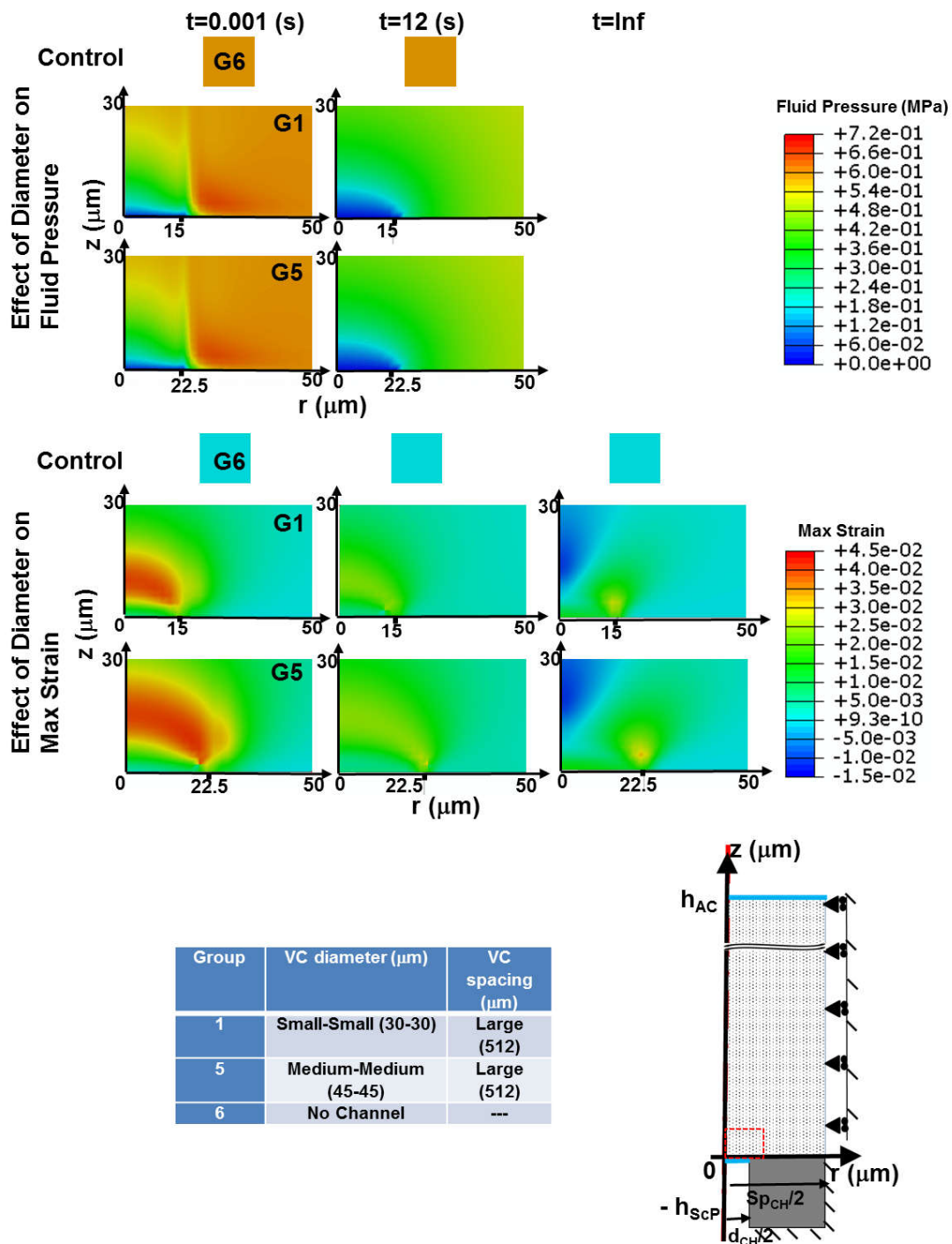


Figure 3.9: Contour plot of the effect of change of diameter on fluid pressure and max principal strain. Results have been shown for the control group (G6), group 1 (G1) and group 5 (G5). The contour plot rectangle is representing the red dashed rectangle around through the cartilage and around the vascular canal in an undeformed state.

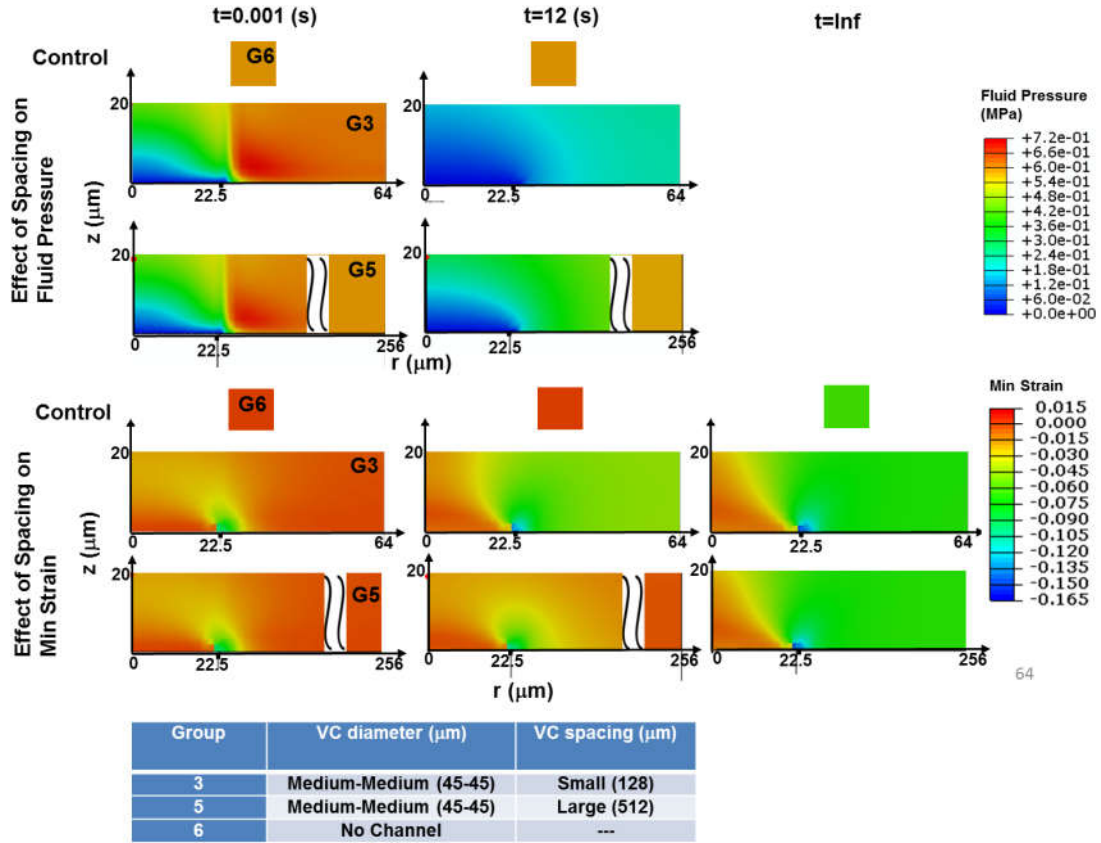


Figure 3.10: Contour plot of the effect of change of spacing on fluid pressure and min principal strain. Results have been shown for the control group (G6), group 3 (G3) and group 5 (G5). Each rectangle shows the area with the height of $20\ \mu\text{m}$ and whole radius of cartilage. for the radius of cartilage having the value of $256\ \mu\text{m}$, a tilt symbol has been represented in order to skip showing the whole long radius. All results are in the undeformed state.

Table 3.1: Representation of critical magnitudes of Mechanical criteria affecting cell viability.
Different experiments have been applied in each study.

Specimen	Geometry	Loading BCs	Displacement/Load control	Criterion	Cell viability	Location	Citation
Calf	disk	Dynamic unconfined compression	u_z	$E_z = 4.3-6.8\%$ $\sigma_z = 0.5\text{MPa}$	Yes	Through thickness	[28, 45]
Calf	disk	compression for 12hrs	u_z	$E_z = 50\%$	No	--	[28, 45]
Mature steer	cartilage disk	Unconfined compression	u_z	$\sigma_z = 2-8\text{ MPa}$ $E_z = 25\%$	Yes	On the surface	[50]
freshly slaughtered calves	plugs	unconfined compression	u_z, u_x	$E_z = 50-80\%$	Yes	Increase through the surface and thickness	[12]
1- to 2-week-old calves	Disk	dynamic tissue simple shear deformation	u_{xz}	$E_{xz,Max} = 1-3\%$	Yes	Center, middle, edge	[26]
young cadaveric human	Cube	indentation	u_z	$E_{z,Max}, E_{z,Min}$ $E_{xz,Max} = 0-15\%$	Considered for comparison	--	[6]
4-5 month old bovine	disk	unconfined compression	P	$\sigma_{z,Max} = 1.0\text{ MPa}$	No	--	[22]
Mature bovine	disk	impacted in confined compression	P, \dot{P}	$E_z = 0.14-0.24$	Yes	Through the thickness	[37]
1 - 2week old calf	disk	Radially unconfined compression	u_z, \dot{u}_z	$\dot{E}_z = 0.1-1/s$ $\sigma_z = 20-24\text{MPa}$	Yes	Through the whole thickness	[30]
Mature bovine	strip	Impact indentation	P	$\sigma_z = 10\text{MPa}$ $E_z = 0.64$	Yes	Starting from under the indenter	[51]
Mature bovine	disk	Impact confined compression	P, \dot{P}	$\sigma_z = 10-60\text{MPa}$	Yes	, 2-6% total thickness	[36]
18 month old bovine	disk	single ramp confine compression	P, \dot{u}_z	$\dot{E}_z = 3e-5/s$ $\sigma_z = 7\text{ MPa}$	Yes	near the radially the central region of explants	[43]

Table 3.2: Different group of geometries for simulation. The first group includes the smallest diameter with the largest spacing. The second group includes the largest diameter with the smallest spacing. Third to fifth groups include medium diameter with smallest, medium and largest diameters respectively, and the last group includes a normal synovial joint with no canal underneath AC.

Group	VC diameter (μm)	VC spacing (μm)
1	Small-Small (30-30)	Large (512)
2	Large-Large (64-64)	Small (128)
3	Medium-Medium (45-45)	Small (128)
4	Medium-Medium (45-45)	Medium (256)
5	Medium-Medium (45-45)	Large (512)
6	No Channel	---

Table 3.3: Material properties of articular cartilage for simulation

Symbol	Definition	Unit	Value	Citation
H_A	Equilibrium Aggregate Modulus	MPa	9	[14].
ν	Poisson's ratio in equilibrium	–	0.25	[54]
\tilde{k}_0	Permeability	m^2/Pas	$1.5e - 16$	[35]
n	Void ratio	–	3	[14].

Table 3.4: Material property inputs in ABAQUS based on data from Table 3.3

Symbol	Definition	Unit	value
C_{10}	$\frac{G}{2}$	MPa	1.5
D_1	$\frac{2}{K}$	MPa^{-1}	0.4
k_0	Initial permeability	$\frac{mm}{s}$	$1.5e - 9$
n	Void ratio	–	3

Table 3.5: Half of diameter and spacing and the corresponded characteristic times based on half sizes

GrP	$d_{CH}/2$ (μm)	$Sp_{CH}/2$ (μm)	τ_{CH} (s)	τ_{Sp} (s)
1	15	256.0	0.2	48.5
2	30	64	0.8	3.4
3	22.5	64	0.4	3.4
4	22.5	128	0.4	12.9
5	22.5	256.0	0.4	48.5
Mean			0.4	23.3

Table 3.6: Three-time courses of the simulation

Time course (s)	Short time (t_1)	Intermediate time (t_2)	Equilibrium time (t_{inf})
	1×10^{-3}	~ 12	∞

Table 3.7: Variables to define the equations of the problem in ABAQUS

Symbol	Definition	Unit
U	Strain energy density	$\frac{N \cdot mm}{mm^3}$
\bar{I}_1	First invariant of the isochoric part of the right Cauchy-Green deformation tensor	--
J_{el}	Elastic volume ratio	---
σ	Total Cauchy stress	MPa
σ^m	Effective stress	MPa
Δp	change of pore pressure of the fluid inside the porous material respect to the reference state	MPa
$[I]$	Unit matrix	----
\vec{f}	volumetric flow rate of the fluid through a unit area of the cartilage	mm/s
\vec{V}_w	average velocity of the fluid relative to the solid phase	mm/s

3.7 Reference

1. Armstrong CG, Lai WM, Mow VC: An analysis of the unconfined compression of articular cartilage. *J Biomech Eng* 106:165-73, 1984.
2. Ashraf S, Mapp PI, Walsh DA: Contributions of angiogenesis to inflammation, joint damage, and pain in a rat model of osteoarthritis. *Arthritis Rheum* 63:2700-10, 2011.
3. Ateshian GA, Maas S, Weiss JA: Finite element algorithm for frictionless contact of porous permeable media under finite deformation and sliding. *J Biomech Eng* 132:061006, 2010.
4. Ayotte DC, Ito K, Perren SM, Tepic S: Direction-dependent constriction flow in a poroelastic solid: the intervertebral disc valve. *J Biomech Eng* 122:587-93, 2000.
5. Ayotte DC, Ito K, Tepic S: Direction-dependent resistance to flow in the endplate of the intervertebral disc: an ex vivo study. *J Orthop Res* 19:1073-7, 2001.
6. Bae WC, Lewis CW, Levenston ME, Sah RL: Indentation testing of human articular cartilage: effects of probe tip geometry and indentation depth on intra-tissue strain. *J Biomech* 39:1039-47, 2006.
7. Bear J. Dynamics of Fluids in Porous Media. New York: American Elsevier Publishing; 1972.
8. Biot MA: General theory of three-dimensional consolidation. *J Appl Phys* 12:155-64, 1941.
9. Blagojevic M, Jinks C, Jeffery A, Jordan KP: Risk factors for onset of osteoarthritis of the knee in older adults: a systematic review and meta-analysis. *Osteoarthritis Cartilage* 18:24-33, 2010.
10. Bowen RM: Incompressible porous media models by use of the theory of mixtures. *Int J Eng Sci* 18:1129-48, 1980.
11. Buschmann MD, Soulhat J, Shirazi-Adl A, Jurvelin JS, Hunziker EB: Confined compression of articular cartilage: Linearity in ramp and sinusoidal tests and the importance of interdigitation and incomplete confinement. *J Biomech* 31:171-8, 1998.
12. Chahine NO, Ateshian GA, Hung CT: The effect of finite compressive strain on chondrocyte viability in statically loaded bovine articular cartilage. *Biomechan Model Mechanobiol* 6:103-11, 2007.
13. Chahine NO, Wang CC, Hung CT, Ateshian GA: Anisotropic strain-dependent material properties of bovine articular cartilage in the transitional range from tension to compression. *J Biomech* 37:1251-61, 2004.

14. Chen SS, Falcovitz YH, Schneiderman R, Maroudas A, Sah RL: Depth-dependent compressive properties of normal aged human femoral head articular cartilage: relationship to fixed charge density. *Osteoarthritis Cartilage* 9:561-9, 2001.
15. Choi JB, Youn I, Cao L, Leddy HA, Gilchrist CL, Setton LA, Guilak F: Zonal changes in the three-dimensional morphology of the chondron under compression: the relationship among cellular, pericellular, and extracellular deformation in articular cartilage. *J Biomech* 40:2596-603, 2007.
16. Clark JM: The structure of vascular channels in the subchondral plate. *J Anat* 171:105-15, 1990.
17. Donahue TL, Hull ML, Rashid MM, Jacobs CR: A finite element model of the human knee joint for the study of tibio-femoral contact. *J Biomech Eng* 124:273-80, 2002.
18. Ewers BJ, Dvoracek-Driksna D, Orth MW, Haut RC: The extent of matrix damage and chondrocyte death in mechanically traumatized articular cartilage explants depends on rate of loading. *J Orthop Res* 19:779-84, 2001.
19. Fawns HT, Landells JW: Histochemical studies of rheumatic conditions. I. Observations on the fine structures of the matrix of normal bone and cartilage. *Ann Rheum Dis* 12:105-13, 1953.
20. Felson DT, Lawrence RC, Dieppe PA, Hirsch R, Helmick CG, Jordan JM, Kington RS, Lane NE, Nevitt MC, Zhang Y, Sowers M, McAlindon T, Spector TD, Poole AR, Yanovski SZ, Ateshian G, Sharma L, Buckwalter JA, Brandt KD, Fries JF: Osteoarthritis: new insights. Part 1: the disease and its risk factors. *Ann Intern Med* 133:635-46, 2000.
21. Garcia JJ, Altiero NJ, Haut RC: An approach for the stress analysis of transversely isotropic biphasic cartilage under impact load. *J Biomech Eng* 120:608-13, 1998.
22. Guilak F, Meyer BC, Ratcliffe A, Mow VC: The effects of matrix compression on proteoglycan metabolism in articular cartilage explants. *Osteoarthritis Cartilage* 2:91-101, 1994.
23. Guo H, Maher SA, Torzilli PA: A biphasic multiscale study of the mechanical microenvironment of chondrocytes within articular cartilage under unconfined compression. *J Biomech* 47:2721-9, 2014.
24. Hosseini A, Van de Velde SK, Kozanek M, Gill TJ, Grodzinsky AJ, Rubash HE, Li G: In-vivo time-dependent creep articular cartilage contact behavior of the tibiofemoral joint. *Osteoarthritis Cartilage* 18:909-16, 2010.
25. Hou JS, Holmes MH, Lai WM, Mow VC: Boundary conditions at the cartilage-synovial fluid interface for joint lubrication and theoretical variations. *J Biomech Eng* 111:78-87, 1989.

26. Jin M, Frank EH, Quinn TM, Hunziker EB, Grodzinsky AJ: Tissue shear deformation stimulates proteoglycan and protein biosynthesis in bovine cartilage explants. *Arch Biochem Biophys* 395:41-8, 2001.
27. Jurvelin JS, Buschmann MD, Hunziker EB: Optical and mechanical determination of Poisson's ratio of adult bovine humeral articular cartilage. *J Biomech* 30:235-41, 1997.
28. Kim YJ, Sah RL, Grodzinsky AJ, Plaas AH, Sandy JD: Mechanical regulation of cartilage biosynthetic behavior: physical stimuli. *Arch Biochem Biophys* 311:1-12, 1994.
29. Kurosawa H, Fukubayashi T, Nakajima H: Load-bearing mode of the knee joint: physical behavior of the knee joint with or without menisci. *Clin Orthop Relat Res* 149:283-90, 1980.
30. Kurz B, Jin M, Patwari P, Cheng DM, Lark MW, Grodzinsky AJ: Biosynthetic response and mechanical properties of articular cartilage after injurious compression. *J Orthop Res* 19:1140-6, 2001.
31. Li G, Gil J, Kanamori A, Woo SL: A validated three-dimensional computational model of a human knee joint. *J Biomech Eng* 121:657-62, 1999.
32. Loeser RF, Goldring SR, Scanzello CR, Goldring MB: Osteoarthritis: a disease of the joint as an organ. *Arthritis Rheum* 64:1697-707 2012.
33. Mahjoub M, Berenbaum F, Houard X: Why subchondral bone in osteoarthritis? The importance of the cartilage bone interface in osteoarthritis. *Osteoporos Int* 23 Suppl 8:S841-6, 2012.
34. Mak AF, Lai WM, Mow VC: Biphasic indentation of articular cartilage--I. Theoretical analysis. *J Biomech* 20:703-14, 1987.
35. Maroudas A: Physicochemical properties of cartilage in the light of ion exchange theory. *Biophys J* 8:575-95, 1968.
36. Milentjevic D, Helfet DL, Torzilli PA: Influence of stress magnitude on water loss and chondrocyte viability in impacted articular cartilage. *J Biomech Eng* 125:594-601, 2003.
37. Milentjevic D, Torzilli PA: Influence of stress rate on water loss, matrix deformation and chondrocyte viability in impacted articular cartilage. *J Biomech* 38:493-502, 2005.
38. Morel V, Quinn TM: Cartilage injury by ramp compression near the gel diffusion rate. *J Orthop Res* 22:145-51, 2004.
39. Mow VC, Bachrach NM, Ateshian GA: The effects of a subchondral bone perforation on the load support mechanism within articular cartilage. *Wear* 175:167-75, 1994.

40. Mow VC, Guo XE: Mechano-electrochemical properties of articular cartilage: their inhomogeneities and anisotropies. *Annu Rev Biomed Eng* 4:175-209, 2002.
41. Mow VC, Holmes MH, Lai WM: Fluid transport and mechanical properties of articular cartilage: a review. *J Biomech* 17:377-94, 1984.
42. Mow VC, Kuei SC, Lai WM, Armstrong CG: Biphasic creep and stress relaxation of articular cartilage in compression: theory and experiment. *J Biomech Eng* 102:73-84, 1980.
43. Quinn TM, Allen RG, Schalet BJ, Perumbuli P, Hunziker EB: Matrix and cell injury due to sub-impact loading of adult bovine articular cartilage explants: effects of strain rate and peak stress. *J Orthop Res* 19:242-9, 2001.
44. Redler I, Mow VC, Zimny ML, Mansell J: The ultrastructure and biomechanical significance of the tidemark of articular cartilage. *Clin Orthop Relat Res* 112:357-62, 1975.
45. Sah RL, Kim YJ, Doong JH, Grodzinsky AJ, Plaas AHK, Sandy JD: Biosynthetic response of cartilage explants to dynamic compression. *J Orthop Res* 7:619-36, 1989.
46. Shibakawa A, Yudoh K, Masuko-Hongo K, Kato T, Nishioka K, Nakamura H: The role of subchondral bone resorption pits in osteoarthritis: MMP production by cells derived from bone marrow. *Osteoarthritis Cartilage* 13:679-87, 2005.
47. Shim VB, Hunter PJ, Pivonka P, Fernandez JW: A multiscale framework based on the physiome markup languages for exploring the initiation of osteoarthritis at the bone-cartilage interface. *IEEE Trans Biomed Eng* 58:3532-6, 2011.
48. Simon BR: Multiphase poroelastic finite element models for soft tissue structures. *Appl Mech Rev* 45:191-218, 1992.
49. Suh JK, Woo SLY: Negative hydrostatic pressure in articular cartilage extracellular matrix under cyclic compressive load. *ASME Advances in Bioengineering* BED-22:199-202, 1992.
50. Thibault M, Poole AR, Buschmann MD: Cyclic compression of cartilage/bone explants in vitro leads to physical weakening, mechanical breakdown of collagen and release of matrix fragments. *J Orthop Res* 20:1265-73, 2002.
51. Torzilli PA, Grigiene R, Borrelli J, Jr., Helfet DL: Effect of impact load on articular cartilage: cell metabolism and viability, and matrix water content. *J Biomech Eng* 121:433-41, 1999.
52. Walsh DA, Bonnet CS, Turner EL, Wilson D, Situ M, McWilliams DF: Angiogenesis in the synovium and at the osteochondral junction in osteoarthritis. *Osteoarthritis Cartilage* 15:743-51, 2007.

53. Walsh DA, McWilliams DF, Turley MJ, Dixon MR, Franses RE, Mapp PI, Wilson D: Angiogenesis and nerve growth factor at the osteochondral junction in rheumatoid arthritis and osteoarthritis. *Rheumatology (Oxford)* 49:1852-61, 2010.
54. Wang CC, Deng JM, Ateshian GA, Hung CT: An automated approach for direct measurement of two-dimensional strain distributions within articular cartilage under unconfined compression. *J Biomech Eng* 124:557-67, 2002.

CHAPTER 4:

BENDING OF A POROELASTIC SHEET:

IMPLICATIONS FOR CARTILAGE SHAPING AND

GRAFTING

4.1 Abstract

Introduction.

Grafts of contour-matched cartilage attached to bone are a promising treatment of large articular defects. However, fabrication of such grafts is complicated by curved surfaces. One approach to achieving shaped cartilage is to bend and hold a sheet of immature tissue, allowing gradual remodeling that ultimately reshapes the tissue to a bent state. While the mechanics of cartilage and hydrogels subjected to compression are described well by poroelastic biphasic models, the response of hydrogel sheets to bending remains to be elucidated. The aim of this study was to analyze the mechanics of a poroelastic sheet when subjected to ramp-and-hold bending, and then instantaneous release.

Methods.

Assuming linear elastic behavior, small strain, and constant material properties, a semi-analytical solution was developed.

Results.

Under pure bending, axial strain varies linearly between compression and tension (concave to convex). In the bent state, the bending moment relaxes as strain redistributes axially, and fluid is exuded from the compressed region and imbibed in the stretched region. At equilibrium, the bending moment and strain stabilize as fluid ceases to flow. After the bending is suddenly released, creep recovery occurs as fluid flow into and out of the sheet reverses and also redistributes within the sheet.

Discussion.

These results indicate the spatial-temporal variation of stress, strain, and flow within a hydrogel sheet when subjected to bending, and may be useful for TE-RM.

4.2 Introduction

Poroelasticity, as a well-developed theory, describes the mechanics of a porous medium through the coupled migration of the viscous solvent and elastic deformation of the solid network [3]. The linear poroelastic theory developed by Biot [3] incorporates Hooke's law of elasticity of the solid matrix, the Navier-Stokes equations for a viscous fluid [9], and Darcy's law for fluid flow through a porous matrix [3, 9]. With the solid and fluid components, each assumed to be incompressible, the constitutive equations describing poroelasticity reduce to relatively simple constitutive ones [3, 42]. The theory of poroelasticity is equivalent mathematically to the theory of mixtures [32]. Poroelasticity facilitates analysis of the time-dependent porous media behavior and has been applied widely, in civil engineering [8], chemical engineering [7], petroleum engineering [11], mechanical engineering [29], and bioengineering [24].

One of the most important aspects of poroelasticity is to model articular cartilage, a hydrated load-bearing connective tissue [2, 10, 25], construed as a two-phase material of solid and liquid. Under some mechanical injuries or wear, articular cartilage needs to be replaced with a synthetic cartilage such as hydrogel [22, 33, 5]. Hydrogel, a three-dimensional hydrophilic polymer network swollen in water [5, 22, 33], has a similar biphasic structure respect to articular cartilage [16, 34]. To analyze biphasic behavior of articular cartilage or hydrogel, theory of poroelasticity was applied to model the biphasic creep or stress relaxation of articular cartilage under various loading conditions [3, 4, 6, 42] including uniaxial confined compression [12, 24], as well as unconfined compression [1] and indentation [21].

We have recently reported an experiment on a flat cartilage specimen, submerged in a solvent, bent around a cylinder. The bent cartilage sheet was held subsequently with a fixed radius for a prolonged period (\sim days), and finally, the external load was removed [39]. It was observed that the stress/strain field and solvent concentration in the cartilage sheet were inhomogeneous and evolved with time. This important phenomenon motivated us to analyze the bending of a poroelastic sheet around a cylindrical contour analytically, during the whole time periods of loading (stress relaxation) and unloading (creep) process.

In preceding investigations of biphasic and mechanical behavior of poroelastic materials, either isotropic [15, 17, 18, 27, 28, 29, 35, 37, 38, 43] or transversely isotropic [13, 19, 26], only the creep or stress relaxation has been analyzed during loading process. Several tests have been employed to study stress relaxation in poroelastic materials with different geometries, containing annular poroelastic disk under unconfined compression [13], a poroelastic plate with limited length [17, 36, 37] or infinite length [26] as well as a cylindrical shell under different loading conditions. Furthermore, Stress relaxation has been analyzed in poroelastic beams of rectangular [27, 26, 29, 38, 43] or circular [19, 18, 26, 27, 28, 29, 38, 41, 43] cross sections under bending. In addition to stress relaxation tests, creep only has been studied in poroelastic materials under different loading conditions such as terminal couples [26] as well as distributed axial and normal loads [17] [18] and bending [15, 17, 18, 26, 29, 41]. Despite the studies above in which stress relaxation or creep has been investigated, in this study in agreement with our experiment[39], disregarding cartilage remodeling, we use linear poroelastic theory to formulate the bending problem and attain semi-analytical solutions. In the following, we

first review linear poroelasticity theory and then apply the theory to the problem discussed above.

4.3 Materials and Methods

Rapid bending and then release of a hydrogel around a cylinder is sketched in Fig. 1. A flat free-standing poroelastic sheet, with length l , thickness h , and width w , completely swollen in solvent, is initially in an equilibrium state (**Fig. 4.1A**, $t=0$). Constant parameters have been defined in **Table 4.1**. Both the stress and strain fields in the sheet are zero, namely, $\sigma_{ij} = 0$ and $\varepsilon_{ij} = 0$ (**Table 4.2**). First, in a short time, the sheet is bent around a cylindrical contour with the radius of R_c (**Fig. 4.1B**, $t=0^+$). During instantaneous bending of the sheet, the variables are not function of time. Second, the radius of the bottom surface of the sheet is fixed for a certain period of time (**Fig. 4.1C**, $0^+ < t \leq \infty$). Third, the external load on the sheet is removed instantaneously (**Fig. 4.1D**, $t' = 0^+$). Fourth the shape of the sheet recovers gradually to its original state (**Fig. 4.1E, F**). As interpreted above, t and t' express the time interval of loading and unloading respectively. As shown in this figure, the neutral plane is assumed to be located at the middle plane, while in a real non-linear experiment, the location of the neutral plane may change based on the deformed geometry of the poroelastic sheet. However, applying beam theory results in no change of the length of the neutral plane during stress relaxation and creep recovery.

In the current problem, increasing the radius of the cylinder, R_c , and decreasing the thickness of the sheet, h , results in decreasing the strain such that the linear theory would be valid. Following Biot's theory [3] and our previous work, the constitutive equation for a linear poroelastic material takes the form [46]:

$$\sigma_{ij} = 2G \left(\varepsilon_{ij} + \frac{\nu}{1-2\nu} \varepsilon_{kk} \delta_{ij} \right) - \frac{\Delta\mu}{\Omega} \delta_{ij}, \quad (1)$$

where ν is the Poisson's ratio of the poroelastic matrix in an equilibrium condition (In the calculation, the Poisson's ratio of the poroelastic sheet is set to be $\frac{1}{3}$ [42].), G is the shear

modulus of the solid matrix, and Ω is the volume per molecule of the solvent (constant parameters are introduced in **Table 4.1**). In this formulation, $\Delta\mu = \mu - \mu_0$, where μ and μ_0 are the chemical potentials of solvent inside and surrounding the material respectively [33]. In alternative formulations, $\frac{\Delta\mu}{\Omega}$ is described as the hydrostatic pore pressure [46]. Along with the above equation, the first part of right-handed side expresses the Hook's law for the isotropic elastic solid phase.

The solid matrix and solvent molecules in the sheet are assumed to be incompressible (for cartilage to act as a compressible material, the magnitude of the load needs to be in the order of 10 MPa [40]). Thus, the increase or decrease of the volume of the poroelastic material is due to the influx or efflux of solvent molecules, where ΔC is the change in density concentration of solvent molecules absorbed by the sheet.

$$\varepsilon_{kk} = \Omega\Delta C, \quad (2)$$

The concentration of solvent in the poroelastic material is a time-dependent field, $C(x, y, z, t)$. The number of solvent molecules is conserved, where \vec{J} is the flux of the solvent [6]:

$$\frac{\partial\Delta C}{\partial t} + \nabla \cdot \vec{J} = 0, \quad (3)$$

In general, the poroelastic sheet is not in equilibrium, so that the chemical potential of the solvent in the sheet is also a time-dependent field, $\mu(x, y, z, t)$. The migration of the solvent in the gel is taken to obey Darcy's law, **Eq. 4**, where η is the viscosity of the solvent and k is the permeability of the gel, a measure of the ease with which solvent can flow through a porous material.

$$\vec{j} = -\left(\frac{k}{\eta\Omega^2}\right)\vec{\nabla}(\Delta\mu), \quad (4)$$

The values of η and Ω are generally constant and well known for a given solvent, so that, **Eq. 4** depends on the permeability of the material, k , which has the dimension of length squared. The ratio, $\frac{k}{\eta}$ is often described as hydraulic permeability, k_p [14].

Since the thickness of the poroelastic sheet, h , is assumed to be much less than its width, w , and the radial dimension of interest, R_0 , the sheet is assumed to be in a plane-strain condition, i.e., $\varepsilon_z = 0$. Therefore, **Eq. 1** can be expanded into its x and y components,

$$\sigma_x(y, t) = 2G \left(\varepsilon_x(y, t) + \frac{\nu}{1-2\nu} [\varepsilon_x(y, t) + \varepsilon_y(y, t)] \right) - \frac{\Delta\mu(y, t)}{\Omega}, \quad (5)$$

$$\sigma_y(y, t) = 2G \left(\varepsilon_y(y, t) + \frac{\nu}{1-2\nu} [\varepsilon_x(y, t) + \varepsilon_y(y, t)] \right) - \frac{\Delta\mu(y, t)}{\Omega}, \quad (6)$$

According to the Saint-Venant's Principle [39], a calculation needs to be sufficiently remote from the edges, such that it depends only on the static resultant of the applied load.

In addition, **Eq. 2** expands into the following:

$$\varepsilon_x(y, t) + \varepsilon_y(y, t) = \Omega\Delta C(y, t). \quad (7)$$

Furthermore, due to the small thickness of the sheet, the time of the diffusion through the thickness of the sheet is much shorter than the time of diffusion through the other sides. So, the migration of the solvent is assumed to be along the normal direction of the sheet, so that, J_i only has y component. Analogously, the concentration field, $C(y, t)$ only has y component. Thus, **Eqs. 3,4** and simplify to:

$$\frac{\partial\Delta C(y, t)}{\partial t} + \frac{\partial J_y(y, t)}{\partial y} = 0, \quad (8)$$

And
$$J_y = -\left(\frac{k}{\eta\Omega^2}\right) \frac{\partial\Delta\mu(y,t)}{\partial y}. \quad (9)$$

The combination of **Eqs. 8, 9** gives the governing equation,

$$\frac{\partial\Delta C(y,t)}{\partial t} = \left(\frac{k}{\eta\Omega^2}\right) \frac{\partial^2\Delta\mu(y,t)}{\partial y^2}. \quad (10)$$

In our experiment, the poroelastic sheet is under bending. $R(t)$ is defined as the radius of the bottom side of the sheet. Using beam theory [39], the strain field in the sheet is approximated by,

$$\epsilon_x(y, t) = \frac{2(R(t)+y)}{2R_c+h} \frac{\theta(t)}{\theta_0} - 1. \quad (11)$$

The traction-free condition at the edges ($y = 0, h$) requires that $\sigma_y(y, t) = 0$ at the top and bottom sides of the sheet. Since the stress field should be identical along the thickness, the vertical stress is zero, i.e., $\sigma_y(y, t) = 0$. The net force in any vertical cross section of the sheet is zero, namely,

$$w \int_0^h \sigma_x(y, t) dy = 0, \quad (12)$$

According to the theory of bending, the moment required to bend the sheet is:

$$M = w \int_0^h \left(y - \frac{h}{2}\right) \sigma_x(y, t) dy. \quad (13)$$

Definition of the normalized variables is expressed in **Table 4.3**. The solutions to the differential equations **Eqs. 8-10** are given in the next section, subject to specific initial and boundary conditions. MATLAB R2010a (MathWorks, Natick, Massachusetts) was used to solve these equations by applying explicit method. Numerical integrations were done using the trapezoidal rule to approximate derivatives of equations, the finite difference method (FDM) was used.

4.4 Results

In this study, the variables are normalized with constant parameters h , w , R_0 , G , Ω , η , k (**Table 4.3**). The radial position of the neutral axis is defined as $R_0 = R_c + h/2$ which is the same as the radius of the neutral plane of the sheet for small deformations. Time of diffusion is related to the size of the material and diffusivity. Over time, a disturbance diffuses over a length \sqrt{Dt} ; Thus, time is normalized as $\frac{Dt}{h^2}$, where diffusivity is $D = \frac{2(1-\nu)Gk}{(1-2\nu)\eta}$. Following our previous paper [46], this expression is based on the coefficient of the diffusion equation, which is calculated using the equations expressed above. In the following, we will analyze the kinematics of the poroelastic sheet in the whole process of loading and unloading, step by step.

4.4.1 Instantaneous bending ($t=0+$)

At a short time, there is no solvent migration within the thickness of the sheet and the sheet is assumed to behave like an incompressible material (**Fig. 4.1B**). In the experiment [43], the time of bending the sheet (\sim several minutes) is much shorter than the characteristic time of the solvent diffusion (\sim days). Thus, we have that,

$$\Delta C = 0. \quad (14)$$

A combination of **Eqs. 7, 14** gives,

$$\varepsilon_x(y) + \varepsilon_y(y) = 0. \quad (15)$$

Based on **Eqns. 5, 6, 11-13, 15**, we find the chemical potential of the solvent in the sheet:

$$\frac{\Delta\mu R_0}{\Omega Gh} = 1 - \frac{2y}{h}, \quad (16)$$

the strain distribution:

$$\frac{\varepsilon_x R_0}{h} = \frac{y}{h} - \frac{1}{2}, \quad (17)$$

$$\frac{\varepsilon_y R_0}{h} = \frac{1}{2} - \frac{y}{h}, \quad (18)$$

the stress distribution:

$$\frac{\sigma_x R_0}{Gh} = \frac{4y}{h} - 2, \quad (19)$$

and the bending moment applied on the sheet:

$$\frac{MR_0}{Gwh^3} = \frac{1}{3}. \quad (20)$$

The chemical potential of the solvent within the sheet is distributed linearly, resulting in constant solvent flux along the thickness of the sheet. Top and bottom surfaces of the sheet are the boundaries between the solvent outside and inside the poroelastic sheet where the chemical potential gradient is infinite due to a discontinuous change in $\Delta\mu$. Based on **Eq. 9**, the flux of the solvent along the thickness would be infinite at the boundaries at $t=0^+$ (**Fig. 4.2A, C**). At $t=0^+$, since the load has been instantaneously applied on the sheet, the chemical potential inside the sheet suddenly changes, increasing in compression part and decreasing in tension part of the sheet (**Fig. 4.3**).

4.4.2 Moment relaxation with maintaining the cylindrical contour ($0^+ < t < \infty$)

In the second step where the curvature of the sheet is kept fixed, the concentration of the solvent changes with time, and the moment applied on the sheet relaxes, due to the fixed curvature of the sheet (**Fig. 4.1C**). It is assumed that both the top and bottom surface of the sheet are permeable. So, the boundary conditions for the chemical potential of the solvent are,

$$\Delta\mu(0, t) = 0 \quad (21)$$

$$\Delta\mu(h, t) = 0 \quad (22)$$

The initial chemical potential of solvent in this step is given in Sec. 3.1, the initial distribution of solvent concentration, $\Delta C = 0$, and the initial bending angle $\theta(0) = \theta_0$. A combination of **Eqs. 5-7** and **Eqs. 10-12** gives the controlling equation of the chemical potential in the sheet,

$$D \frac{\partial^2 \Delta\mu(y, t)}{\partial y^2} = \frac{\partial \Delta\mu(y, t)}{\partial t} + \frac{(1-2\nu)(R_c+y)}{R_0 h} \int_0^h \frac{\partial \Delta\mu(y, t)}{\partial t} dy, \quad (23)$$

With increasing time, the chemical potential of the solvent in the poroelastic sheet becomes increasingly homogenous, and ultimately reaches equilibrium. Based on the above equation and corresponding boundary conditions, the evolution of the solvent chemical potential can be calculated numerically (**Fig. 4.3A, C**). The chemical potential of solvent in the sheet is equal to the chemical potential of solvent outside, when $\frac{Dt}{h^2} \rightarrow \infty$. During this period, since the boundaries are permeable and change of chemical potential is continuous, the distribution of the change of chemical potential has a sinusoidal-like pattern. It can be easily proved that the chemical potential of solvent in the sheet is anti-

symmetric with respect to the middle plane $y = h/2$, which is consistent with our numerical results in **Fig. 4.3** [28-30].

A combination of **Eqs. 5, 7, 11-12** gives the relationship between the bending angle and the distribution of chemical potential,

$$\frac{\theta(t)}{\theta_0} = 1 + \frac{1-2\nu}{2\Omega Gh} \int_0^h \Delta\mu(y, t) dy . \quad (24)$$

Since the chemical potential is anti-symmetric with respect to the middle plane, $y = h/2$, the integration in **Eq. 24** is zero. In consequence, $\theta(t) = \theta_0$. Inserting this result into **Eq. 11**, we can obtain the strain field in the axial direction which indicates that the evolution of horizontal strain is independent of the time of relaxation. (**Fig. 4.4A, C**).

$$\frac{\varepsilon_x(y, t) R_0}{h} = \frac{y}{h} - \frac{1}{2} , \quad (25)$$

Although in this step, the horizontal strain is independent of time, the vertical strain field evolves with time due to the change of solvent concentration in the sheet. Using the calculated distribution of chemical potential of solvent in the poroelastic sheet and strain distribution in **Eq. 25**, we further calculate the evolution of strain in the vertical direction (**Fig. 4.5**). The concentration of the solvent inside the sheet increases in the upper half part and decreases in the lower half part (**Fig. 4.6A, C**), and so does the vertical strain (**Fig. 4.5A, C**). During stress relaxation, since the distribution of horizontal strain does not change over time, and the change of chemical potential at the boundaries are zero, both changes of solvent concentration and vertical strain fields will remain constant at the boundaries of the sheet.

With the migration of solvent, both stress and moment gradually relax during this step. The stress field in the sheet and bending moment applied on the sheet have been sketched in **Fig. 4.7** and **Fig. 4.8** respectively. The graphs plotted in **Fig. 4.2A, C** prove that during the stress relaxation time, the solvent influxes into the top surface and effluxes from the bottom surface.

After a long enough time, the poroelastic sheet reaches the equilibrium state, and the chemical potential of solvent inside the gel is equal to that of the solvent outside the gel, namely, $\Delta\mu(y) = 0$. Therefore, when the poroelastic sheet reaches equilibrium, based on the beam theory discussed in Sec. 2, we can easily obtain the distribution of the vertical strain:

$$\frac{\varepsilon_y(y,t \rightarrow \infty)R_0}{h} = \frac{\nu}{2h(1-\nu)}(h - y), \quad (26)$$

the stress distribution in axial direction:

$$\frac{\sigma_x(y,t \rightarrow \infty)R_0}{Gh} = \frac{\nu}{2h(1-\nu)}(2y - h), \quad (27)$$

the moment:

$$\frac{M(y,t \rightarrow \infty)R_0}{Gwh^3} = \frac{1}{6(1-\nu)}, \quad (28)$$

which is plotted as dash line in **Fig. 4.7A**, and the solvent concentration:

$$\frac{\Omega\Delta C(y,t \rightarrow \infty)R_0}{h} = \frac{1-2\nu}{2h(1-\nu)}(2y - h), \quad (29)$$

In these results, Poisson's ratio characterizes the chemomechanical interaction of the poroelastic sheet such that, at equilibrium, the poroelastic sheet behaves like an elastic sheet having compressibility.

4.4.3 Instantaneous unloading ($t' = 0^+$)

In this step, the sheet is fully equilibrated with external solvent and the external load on the poroelastic sheet is removed suddenly (\sim seconds), where the sheet retains its shape immediately following. Following the experimental procedure [43], in the fast unloading process, the time is too short to allow for solvent migration such that $\Delta C(y, t' = 0^+) = \Delta C(y, t \rightarrow \infty)$ (**Fig. 4.6B,C**). As the result of removing the external load, both the external force and applied moment are zero. In this step, under instantaneous unloading, as shown in **Fig. 4.3**, the chemical potential resists the applied compression to the upper half part of the sheet, so it increases. The chemical potential will decrease in the lower half part under instantaneous tension.

As expressed in Sec. 3.2, the concentration of solvent is a linear function of y -axis, so the horizontal stress is zero through the horizontal strain is not zero (**Fig. 4.6**),

$$\sigma_x(y, t' = 0^+) = 0, \quad (30)$$

A combination of **Eqs. 5-7, 11** enables us to calculate the chemical potential of the solvent in the sheet (**Fig. 4.3B, C**),

$$\frac{\Delta\mu(y, t'=0^+)R_0}{\Omega Gh} = \frac{1}{2h(1-\nu)}(y - h), \quad (31)$$

The strain in horizontal (**Figs. 4.4B, C**) and vertical (**Figs. 4.5B, C**) directions are:

$$\frac{\varepsilon_x(y, t'=0^+)R_0}{h} = \frac{\varepsilon_y(y, t'=0^+)R_0}{h} = \frac{1-2\nu}{4h(1-\nu)}(2y - h), \quad (32)$$

The top part of the sheet is squeezed suddenly during instantaneous unloading. Therefore, the horizontal strain decreases while the vertical strain increases. The curvature (**Fig. 4.8D**) of the middle plane of the sheet is found to be:

$$\kappa(t' = 0^+)R_0 = \frac{1-2\nu}{2(1-\nu)}. \quad (33)$$

Repeatedly, as a result of the discontinuity of the change of chemical potential at the boundaries, the flux of the solvent is infinite at the top and bottom surfaces of the sheet (**Fig. 4.2B, D**).

4.4.4 Creep recovery ($0^+ < t' \leq \infty$)

In our model, the poroelastic sheet gradually retains its original flat shape. In the recovery process, the chemical potential of solvent on the top and bottom surface of the sheet is equilibrated with the solvent outside. In this step, the initial chemical potential of solvent and the initial radius of the middle plane of the sheet are calculated by **Eq. 31** and **Eq. 33** respectively. The initial distribution of solvent concentration is given in Sec 4.2.

A combination of **Eqs. 5,6** and **Eqs. 10-13**, inputting zero moment, gives the controlling equation of the chemical potential in the sheet,

$$D \frac{\partial^2 \Delta\mu(y,t')}{\partial y^2} = \frac{\partial \Delta\mu(y,t')}{\partial t} + \frac{3(1-2\nu)}{h^3} (2y - h) \int_0^h (2y - h) \frac{\partial \Delta\mu(y,t')}{\partial t} dy. \quad (34)$$

The distribution of the chemical potential of solvent can be calculated numerically based on the equation above, and corresponding boundary conditions and initial conditions, (**Fig. 4.3B, C**). It can be proved that in this step, the chemical potential of solvent in the

sheet is also anti-symmetric with respect to the middle plane $y = h/2$, which is consistent with our numerical results shown in **Fig. 4.3**. Another result which validates our numerical codes is so-called Mandel-Cryer effect [31]. According to **Fig. 3B**, as the poroelastic sheet starts to regain its original shape, the chemical potential in the upper part of the sheet rises beyond its initial value and then relaxes to zero after reaching a maximum amount. After instantaneous unloading, fluids efflux from the upper surface and a larger portion of the stress is transferred to the stiffer middle region of the poroelastic sheet. Similar behavior is found for strain and stress.

A combination of **Eqs. 5, 7, 11, 12** gives the relationship between the bending angle and the distribution of chemical potential,

$$\frac{\theta(t')}{\theta_0} = \frac{3R_0(1-2\nu)}{\Omega Gh^3} \int_0^h (2y - h) \Delta\mu(y, t') dy . \quad (35)$$

Inserting this result into **Eqs. 11-12**, we obtain the strain field in the horizontal direction:

$$\varepsilon_x(y, t') = \frac{3(1-2\nu)}{2\Omega Gh^3} (2y - h) \int_0^h (2y - h) \Delta\mu(y, t') dy . \quad (36)$$

which gives the relaxation of strain field in this step as shown in **Fig. 4.4**.

Using the calculated distribution of chemical potential of solvent in the poroelastic sheet and strain distribution in **Eq. 36**, we can calculate the evolution of strain distribution in vertical direction (**Fig. 4.5**), solvent concentration (**Fig. 4.6**), stress field (**Fig. 4.7**) and the evolution of the curvature of the middle plane of the sheet as plotted in **Fig. 4.8D**. Since the flux of the solvent is calculated based on the gradient of the chemical potential of the solvent inside the poroelastic sheet, it is consistent in the symmetric part of the sheet respect to the middle plane (**Fig. 4.2B, D**). After a long enough time, the poroelastic sheet reaches

its original free-standing state with a flat shape, and the chemical potential of solvent inside the gel is equal to the chemical potential of the solvent outside the gel

4.5 Discussion

In this study, a semi-analytical calculation was successfully developed to shape a poroelastic cartilage sheet through the application of bending mechanical loading and unloading. The results of the micromechanical stress and strain analysis support the hypothesis that tension–compression nonlinearity plays an important role in determining the flexural biomechanics of cartilage. To simulate the evolution of stress and strain fields and solvent concentration in the cartilage sheet under bending, linear poroelastic theory was adopted to calculate the evolution of deformation and solvent concentration in a poroelastic sheet submerged in a solvent and subjected to a pure bending. Loading consists of two subsequent time periods: loading time, $0^+ \leq t \leq \infty$, and unloading time, $0^+ \leq t' \leq \infty$ (**Fig. 4.1**). Next, the governing equations of different fields such as chemical potential and concentration of solvent were acquired. Applying different initial and boundary conditions to the governing equations, the transient response of the bending of hydrogels and cartilage can be easily calculated, although, it has not been analyzed previously.

The deformation within the cartilage was assumed to be infinitesimal by employing linear theory. This assumption helps obtain analytical or semi-analytical results and formulate the plane-strain problem. However, in the previous work, during experiment, the cartilage was under large deformation [43]. Moreover, the solid material and the solvent molecules in the sheet were assumed to be independently incompressible. Thus, the increase or decrease of the volume of the material was due to the influx or efflux of solvent molecules.

Based on the results of this problem, after a long enough time of loading or unloading, the chemical potential of solvent inside the sheet is equal to the chemical

potential of the surrounding solvent (**Fig. 4.2**). These numerical results show that the distribution of some fields such as chemical potential, solvent concentration, strain field and stress field in a poroelastic sheet are anti-symmetric with respect to the middle plane $y = h/2$ in which, the peak amount of the sinusoidal-like graph will decrease over the time of relaxation or creep recovery. This behavior has been observed in some other studies [46]. Distribution of the flux of the solvent is symmetric with respect to the middle plane by cause of the antisymmetric profile of the chemical potential of the solvent inside the sheet. Once the equilibrium is reached after unloading, there is no residual strain and stress inside the sheet and, the poroelastic sheet will recover its original shape.

Although, there are some studies analyzing saturated linear poroelastic materials, such as a disk under unconfined compression [13], plate under cyclic, distributed loads [18, 38] or bending [27, 36], there are no documented studies on poroelastic sheets. According to the assumptions and boundary conditions of the problem, the diffusion of the solvent inside beam-like materials can be in either vertical or horizontal directions [16, 19, 20, 27, 30, 45], which in the current study, is in the vertical direction. Also, previous studies have not studied the unloading creep recovery process integral to practical experiments. In some investigations of poroelastic beams, the main objective is to characterize elastic properties and permeability of the poroelastic beam [28] or the effect of deflection rate and Hertzian indentation [29]. Concisely, in our study, all of the biphasic and mechanical fields have been explained and the creep recovery behavior of the material during the unloading process has been formulated.

In our model, the variables have been normalized in terms of the constant parameters h , w , R_0 , G , Ω , η , k . In consequence, the plotted results are independent of the

modulus of the material, the size of the sheet and the ratio between R_0 and h . However, this model does not account for shear strains and also certain cartilage material properties. In particular, the linear material assumption is an approximation since cartilage exhibits mechanical nonlinearity at higher strains [15]. Although the loading/unloading path in our model was the same as the loading/unloading conditions in our recent experiments on cartilage [43], in the current model, material growth is ignored, which has been observed in our experiments on cartilages and influenced the mechanical behavior.

Our challenge will be how to simulate cartilage behavior under different loading conditions due to the important therapeutic applications of cartilage grafts of pre-determined shapes in the restoration of damaged joints and the reconstruction of head, neck, and joint pathologies. The deformation field and solvent concentration in cartilage can be solved using finite element software such as FEBio [21] or ABAQUS [24]. For example, Wu et al. have successfully used ABAQUS to conduct a mechanical analysis of joint contact problems with the articular cartilage layer [44]. Shirazi et al. [32] have investigated the influence of osteochondral defects on the mechanical environment of cartilage and knee joint using finite element analysis under physiological compression forces.

The results of this study help elucidate inhomogeneous distribution of stress and strain within the thickness of the poroelastic sheet. The deformation applied during this study mimicked that used previously for inducing alterations in cartilage explant shape, the analytical findings help understand the reshaping process [43]. Although poroelastic sheet shaping was analyzed in a simplified 2- dimensional bending configuration, expanding this calculation to 3- dimensional geometry could enhance its potential for clinical utility.

Furthermore, it would be of interest to investigate bending of the cartilage with including non-linearity to the material properties as well as considering an inhomogeneous growth in cartilage. This study provides a foundation for further cartilage bending studies. The testing modality may be conveniently applied to other studies involving implants or grafts.

4.6 Acknowledgment

Chapter 3, in full, is being prepared for submission to *Journal of Biomechanics*. The dissertation author is the primary investigator and thanks co-authors Dr. Shengqiang Cai and Dr. Robert L.Sah.for their contributions.

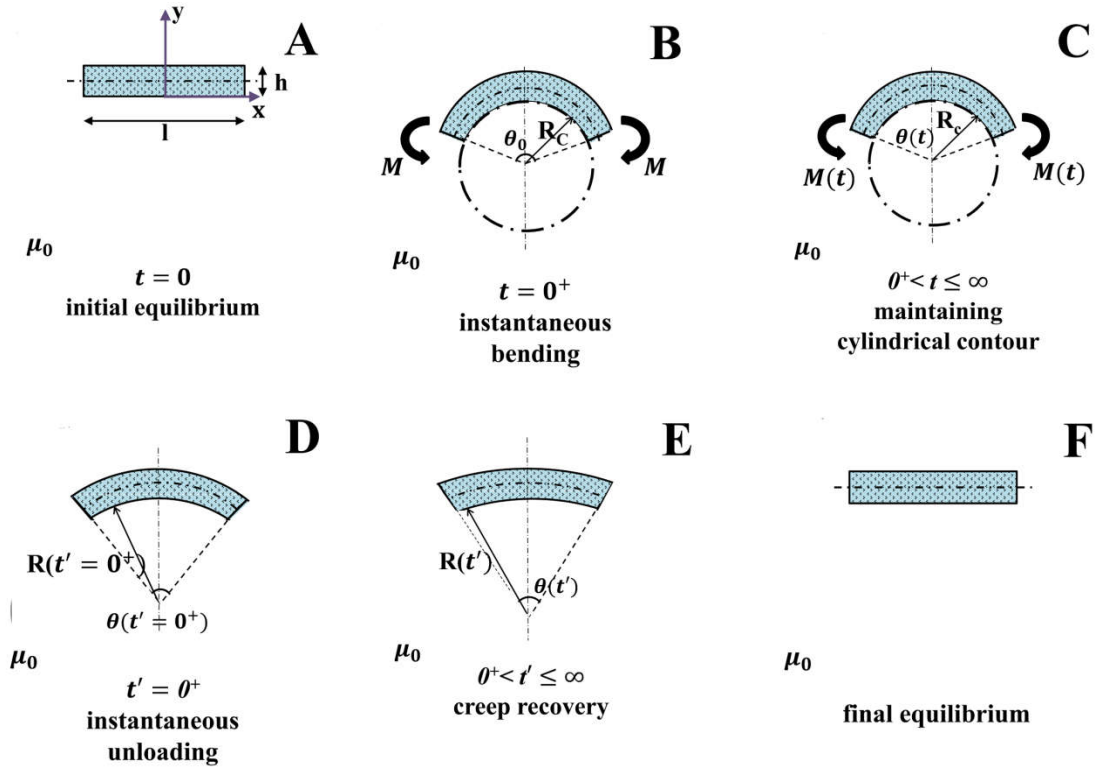


Figure 4.1: Schematics of stress relaxation and creep of a poroelastic sheet submerged in a solvent. (A) A free-standing poroelastic sheet is submerged in a solvent and in an equilibrium state. (B) The sheet is instantaneously bent such that the curvature of the bottom side is a constant everywhere. (C) The curvature of the sheet is subsequently fixed until it reaches equilibrium. The external moment M applied onto the sheet relaxes till a constant value (D) The load applied onto the sheet is removed suddenly, and the curvature of the sheet decreases instantaneously. (E) The curvature of the sheet gradually decreases. (F) After long enough time, the sheet recovers back to its original flat shape.

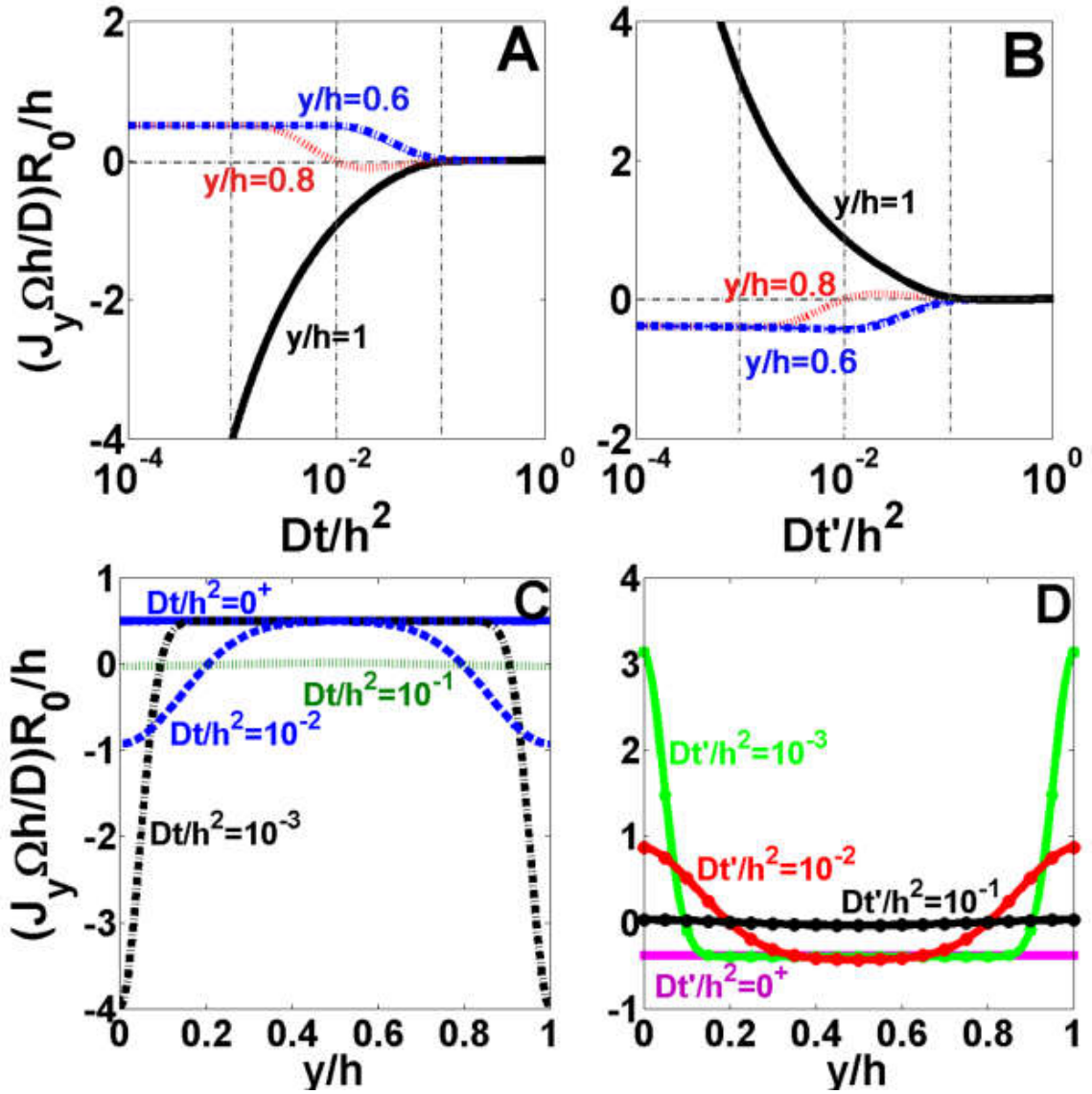


Figure 4.2: Temporal and spatial variation of the vertical flux of the solvent in a poroelastic sheet. (A) and (B) respectively show the temporal evolution of the vertical flux of the solvent at several different positions in the top half of the sheet, in the stress relaxation process ($0^+ \leq t \leq \infty$) and creep process ($0^+ \leq t' \leq \infty$). Since the flux is proportional to the gradient of the change of chemical potential, it is symmetric respect to the middle plane of the sheet. (C) and (D) respectively show a spatial variation of the vertical flux of the solvent in the sheet at a different time in the stress relaxation process ($0^+ \leq t \leq \infty$) and creep process ($0^+ \leq t' \leq \infty$).

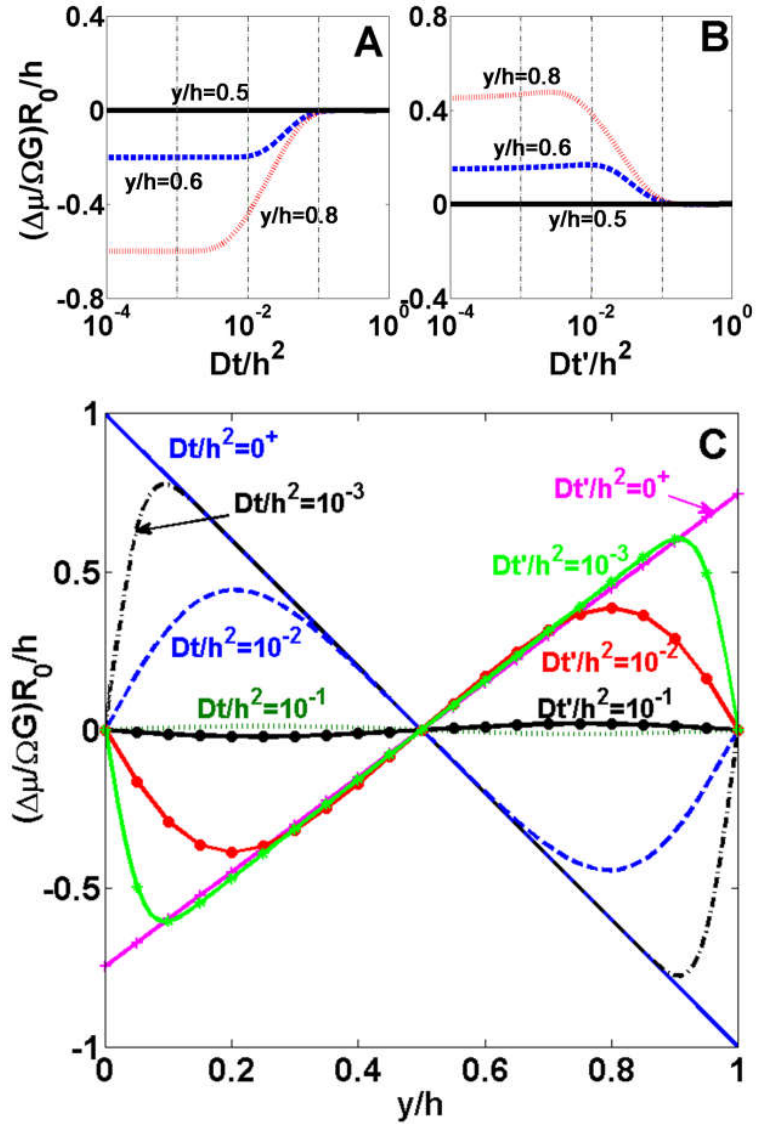


Figure 4.3: Temporal and spatial variation of the chemical potential of solvent in the poroelastic sheet. (A) and (B) respectively show temporal evolution of chemical potential of solvent at several different positions in the top half of the sheet, in stress relaxation process ($0^+ \leq t \leq \infty$) and creep process ($0^+ \leq t' \leq \infty$). (C) Spatial variation of the chemical potential of solvent at a different time in stress relaxation process ($0^+ \leq t \leq \infty$) and creep process ($0^+ \leq t' \leq \infty$). Distribution of change of the chemical potential is antisymmetric with respect to the neutral plane ($y=0.5$) for all time.

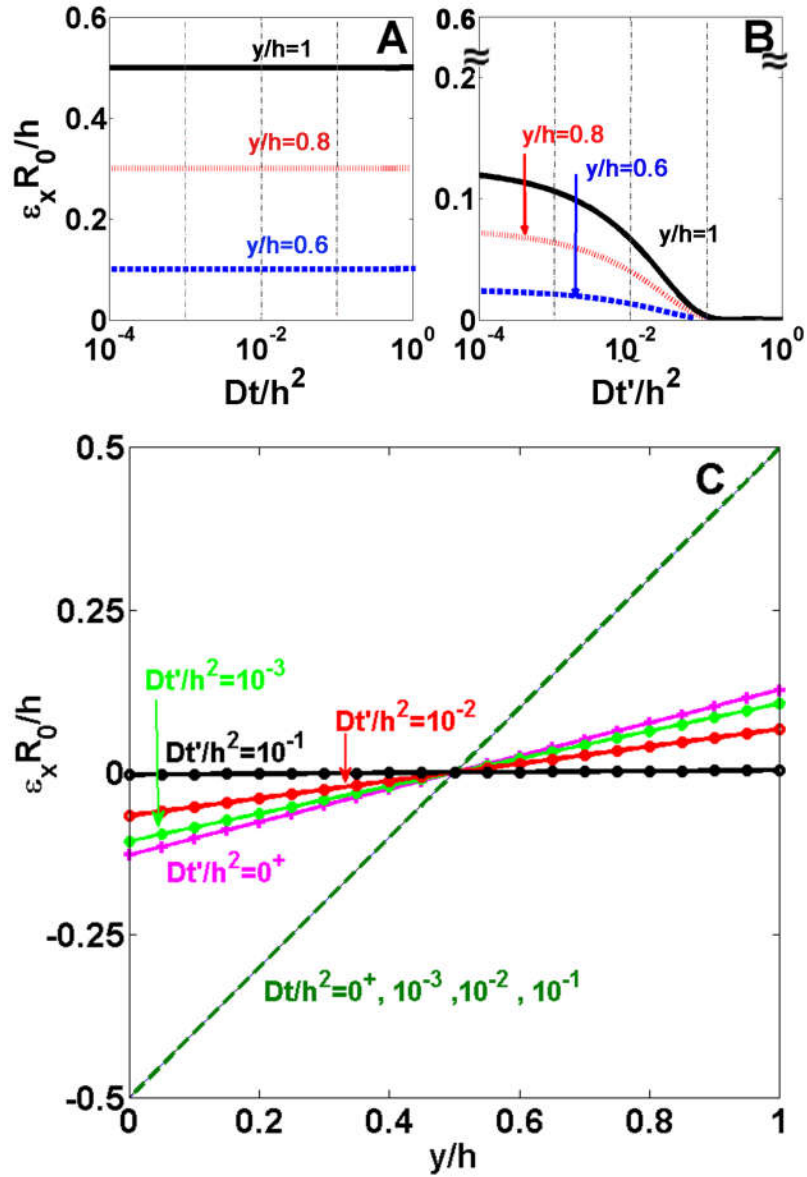


Figure 4.4: Temporal and spatial variation of ε_x in the poroelastic sheet. (A) and (B) respectively show a temporal evolution of ε_x in the sheet at several different positions in the top half of the sheet, in stress relaxation process ($0^+ \leq t \leq \infty$) and creep process ($0^+ \leq t' \leq \infty$). (C) Spatial variation of ε_x in the sheet at a different time in stress relaxation process ($0^+ \leq t \leq \infty$) and creep process ($0^+ \leq t' \leq \infty$). Distribution of ε_x is antisymmetric with respect to the neutral plane ($y=0.5$) for all time

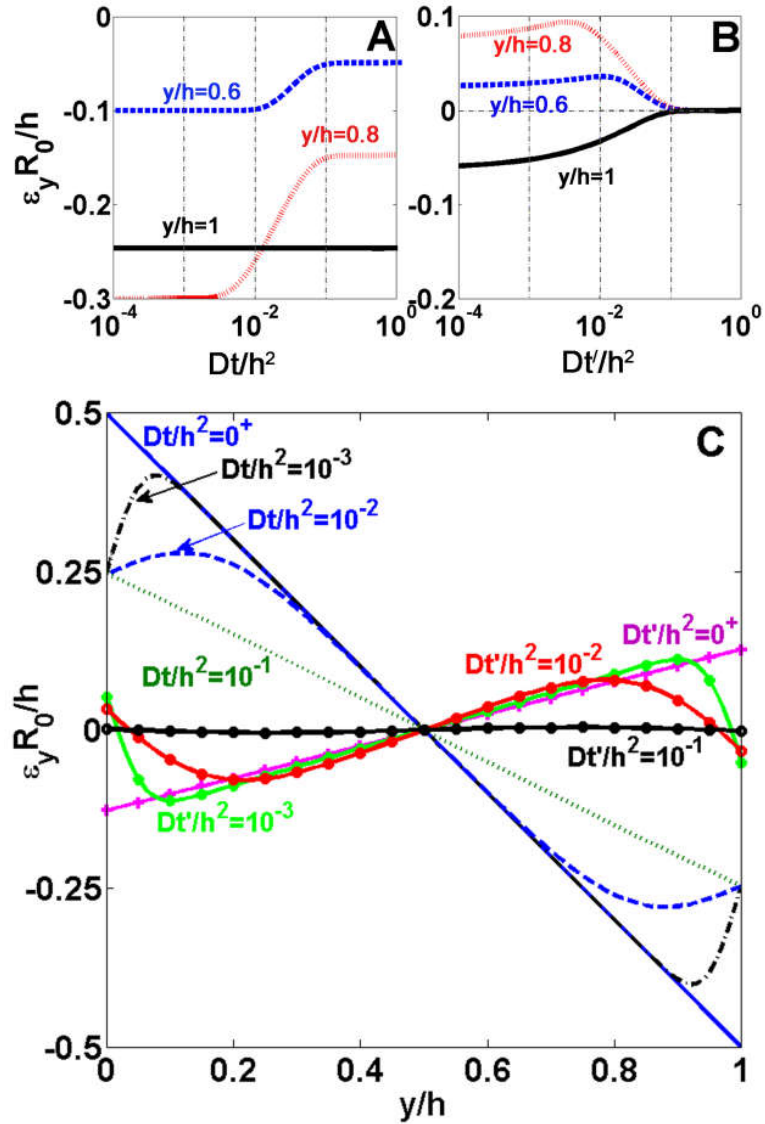


Figure 4.5: Temporal and spatial variation of ε_y in the poroelastic sheet. (A) and (B) respectively show a temporal evolution of ε_y in the sheet at several different positions in the top half of the sheet, in stress relaxation process ($0^+ \leq t \leq \infty$) and creep process ($0^+ \leq t' \leq \infty$). (C) Spatial variation of ε_y in the sheet at a different time in stress relaxation process ($0^+ \leq t \leq \infty$) and creep process ($0^+ \leq t' \leq \infty$). **Distribution of ε_y is antisymmetric with respect to the neutral plane ($y=0.5$) for all time.**

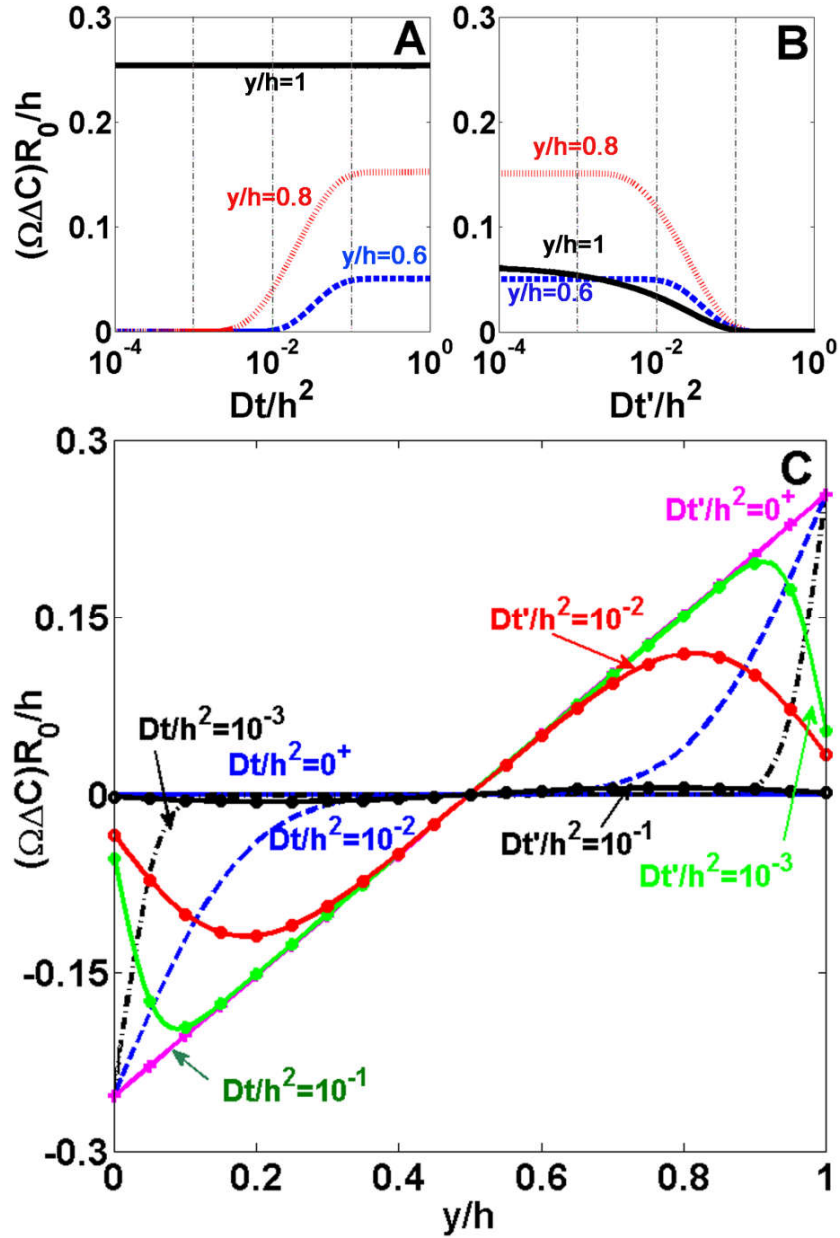


Figure 4.6: Temporal and spatial variation of the change of solvent concentration in the poroelastic sheet. (A) and (B) respectively show temporal evolution of change of solvent concentration in the sheet at several different positions in the top half of the sheet, in stress relaxation process ($0^+ \leq t \leq \infty$) and creep process ($0^+ \leq t' \leq \infty$). (C) Spatial variation of the change of solvent concentration in the sheet at a different time in stress relaxation process ($0^+ \leq t \leq \infty$) and creep process ($0^+ \leq t' \leq \infty$). Distribution of change of solvent concentration is antisymmetric with respect to the neutral plane ($y=0.5$) for all time.

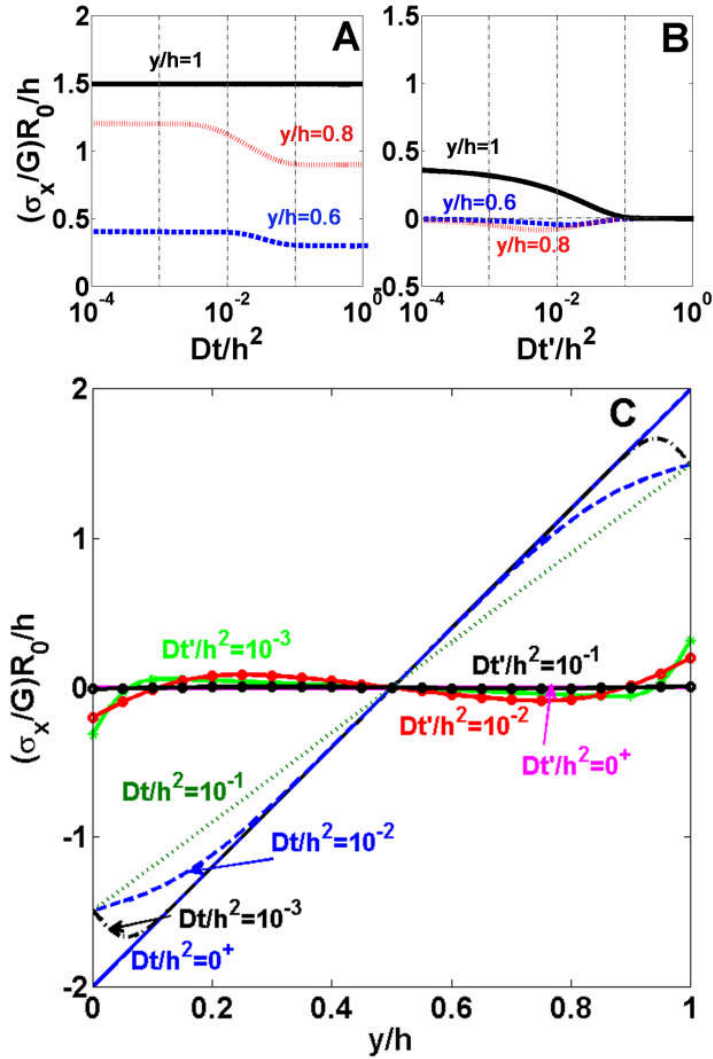


Figure 4.7: Temporal and spatial variation of σ_x in the poroelastic sheet. (A) and (B) respectively show a temporal evolution of σ_x in the sheet at several different positions in the top half of the sheet, in stress relaxation process ($0^+ \leq t \leq \infty$) and creep process ($0^+ \leq t' \leq \infty$). (C) Spatial variation of σ_x in the sheet at a different time in stress relaxation process ($0^+ \leq t \leq \infty$) and creep process ($0^+ \leq t' \leq \infty$). Distribution of σ_x is antisymmetric with respect to the neutral plane ($y=0.5$) for all time.

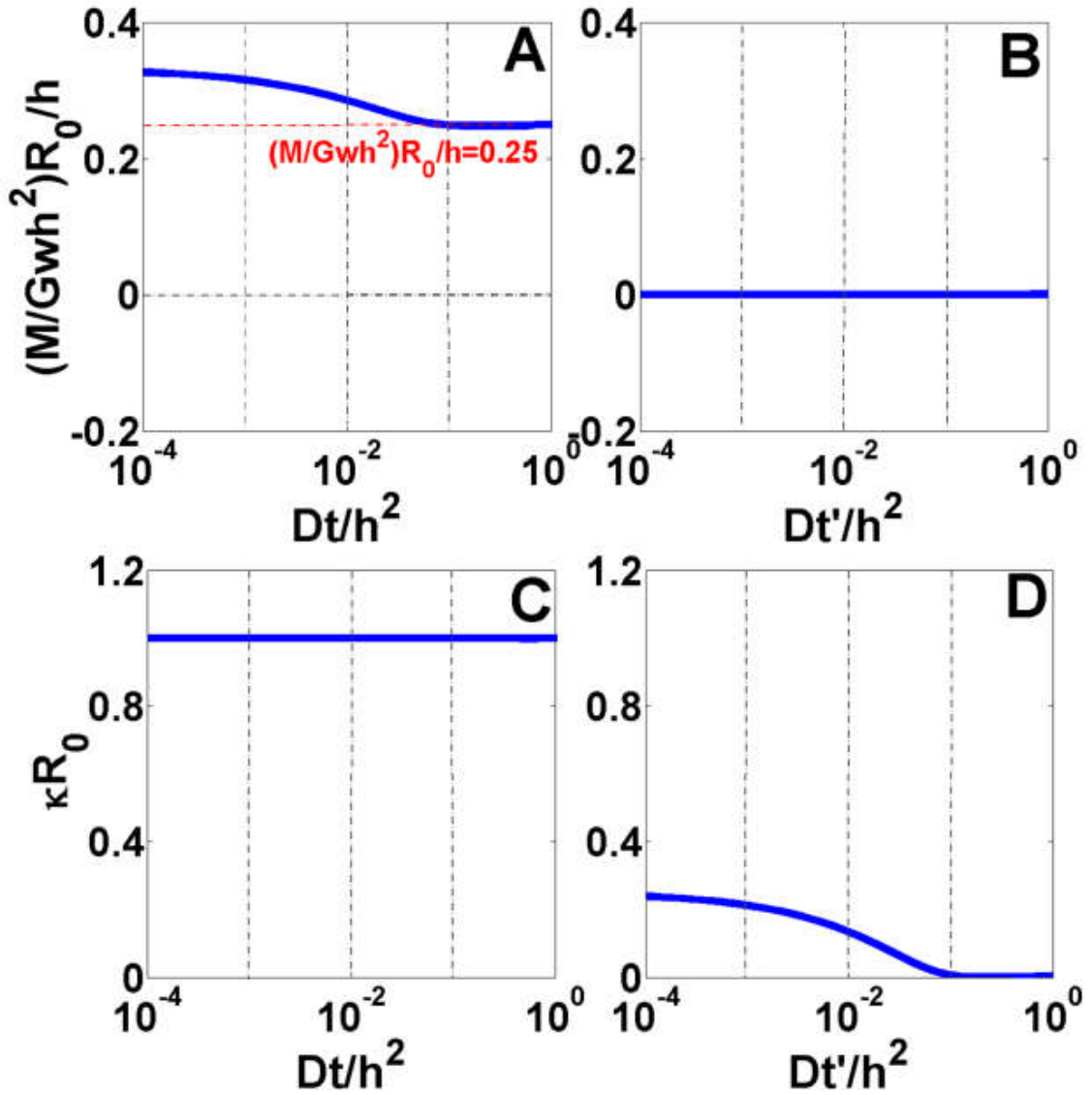


Figure 4.8: Temporal variation of moment and curvature of the neutral plane of the poroelastic sheet. (A) and (B) respectively show temporal evolution of moment, M applied on a poroelastic sheet, in stress relaxation process ($0^+ \leq t \leq \infty$) and creep process ($0^+ \leq t' \leq \infty$). (C) and (D) respectively show temporal evolution of the curvature of the neutral plane, κ of the poroelastic sheet, in stress relaxation process ($0^+ \leq t \leq \infty$) and creep process ($0^+ \leq t' \leq \infty$).

Table 4.1: Constant parameters of the poroelastic sheet and the solvent applied in this study

Symbol	Definition	Unit
C_0	fluid concentration at $t=0$	l/m^3
D	diffusivity	$\frac{m^2}{s}$
η	viscosity of the solvent	kPa
G	shear modulus of the saturated material	kPa
h	initial thickness of the strip in the Y-direction	mm
k	Permeability of the porous material	m^2
l	initial length of the strip in the X-direction	mm
ν	the Poisson's ratio of the strip	dimensionless
w	initial wide of the strip in the Z-direction	mm
Ω	volume per solvent molecules	m^3
R_c	radius of the cylinder	mm
R_0	radius of the neutral axis at $t=0^+$	mm
θ_0	angle of neutral axis bent around the cylinder at $t=0^+$	rad
t_1	equilibrium time during force relaxation procedure	s
t_2	equilibrium time during creep recovery procedure	s

Table 4.2: Process of mechanical loading and unloading of a poroelastic sheet submerged in a solvent including conditions, knowns, and unknowns

Time	Reference state	Initial conditions	Boundary conditions	Knowns	Unknowns
$t = 0$	C_0 μ_0 $\varepsilon_{ij} = 0$ $\sigma_{ij} = 0$				
$t = 0^+$				$C(y, t = 0^+) = C_0$ $\varepsilon_x(y, t = 0^+)$ $\sigma_y = 0$	$\mu(y, t = 0^+)$ $\varepsilon_y(y, t = 0^+)$ M $\sigma_x(y, t = 0^+)$
$0^+ < t \leq t_1$		At $t=0^+$: $C = C_0$ $\mu(y, t) = \mu(y, t = 0^+)$	At $r = 0$ & h , $\mu(y, t) = \mu_0$	The curvature of the bottom surface of the cylinder is constant. ($\kappa_0 = \frac{1}{R_c}$) $\sigma_y(y, t) = 0$	$\varepsilon_y(y, t)$ $\varepsilon_x(y, t)$ $\mu(y, t)$ $C(y, t)$ $\sigma_x(y, t)$
$t = t_1^+$				$C = C(y, t = t_1)$ M = 0 $F_x = 0$ $\sigma_y(y, t_1^+) = 0$ $\varepsilon_x(y, t = t_1^+)$	$\mu(y)$ $\varepsilon_y(y, t = t_1^+)$ $\sigma_x(y, t = t_1^+)$
$t_1^+ < t \rightarrow t_e$		At $t = t_1^+$, $C = C(y, t = t_1^+)$	At $y = 0$ & h , $\mu(y, t) = \mu_0$.	M(t)=0 $\sigma_y(y, t) = 0$ $F_x = 0$	$\varepsilon_y(y, t)$ $\varepsilon_x(y, t)$ $\mu(y, t)$ $C(y, t)$ $\sigma_x(y, t)$ $\kappa(t)$: the curvature of the bottom surface of the strip.
t_e			At $y = 0$ & h , $\mu(y, t) = \mu_0$.	M(t)=0 $\sigma_y(y, t) = 0$ $F_x = 0$	$\varepsilon_y(y, t)$ $\varepsilon_x(y, t)$ $\mu(y, t)$ $C(y, t)$ $\sigma_x(y, t)$ $\kappa(t)$: the curvature of the bottom surface of the strip.

Table 4. 3: Normalized symbols in terms of the constant parameters

Normalized Symbol	Definition
$\frac{J_y \Omega \eta R_0}{kG}$	Flux of the Solvent
$\frac{MR_0}{Gwh^3}$	Moment
$\frac{\mu R_0}{\Omega Gh}$	Chemical Potential of the Solvent
$\frac{\Delta \mu R_0}{\Omega Gh}$	Change of Chemical Potential of the Solvent
$\frac{\epsilon_x R_0}{h}$	Strain in x-direction
$\frac{\epsilon_y R_0}{h}$	Strain in y-direction
$\frac{\sigma_x R_0}{Gh}$	Stress in x-direction
$\frac{Dt}{h^2}$	Time
$\frac{y}{h}$	The location along the thickness
$\frac{R_0}{h}$	The radius of the neutral axis

4.7 References

1. Armstrong CG, Lai WM, Mow VC: An analysis of the unconfined compression of articular cartilage. *J Biomech Eng* 106:165-73, 1984.
2. Bingham JT, Papannagari R, Van de Velde SK, Gross C, Gill TJ, Felson DT, Rubash HE, Li G: In vivo cartilage contact deformation in the healthy human tibiofemoral joint. *Rheumatology (Oxford)* 47:1622-7, 2008.
3. Biot MA: General theory of three-dimensional consolidation. *J Appl Phys* 12:155-64, 1941.
4. Biot MA: Theory of elasticity and consolidation for a porous anisotropic solid. *J Appl Phys* 26:182-5., 1955.
5. Broom ND, Oloyede A: The importance of physicochemical swelling in cartilage illustrated with a model hydrogel system. *Biomaterials* 19:1179-88, 1998.
6. Cai SQ, Hu YH, H ZX, Suo ZG: Poroelasticity of a covalently crosslinked alginate hydrogel under compression *J Appl Phys* 108:113514, 2010.
7. Charras GT, Yarrow JC, Horton MA, Mahadevan L, Mitchison TJ: Non-equilibration of hydrostatic pressure in blebbing cells. *Nature* 435:365-9, 2005.
8. Detournay E, Cheng AH: Poroelastic response of a borehole in a non-hydrostatic stress field. *Int J Rock Mech Min Sci Geomech Abstr* 25:171-82, 1988.
9. Discacciati M, Quarteroni A: Navier-Stokes/Darcy coupling: modeling, analysis, and numerical approximation. *Rev Mat Complut* 22:315-426, 2009.
10. Eckstein F, Lemberger B, Gratzke C, Hudelmaier M, Glaser C, Englmeier KH, Reiser M: In vivo cartilage deformation after different types of activity and its dependence on physical training status. *Ann Rheum Dis* 64:291-5, 2005.
11. Engelder T, Fischer MP: Influence of poroelastic behavior on the magnitude of minimum horizontal stress, S_h in overpressured parts of sedimentary basins. *Geology* 22:949-52, 1994.
12. Frank EH, Grodzinsky AJ: Cartilage electromechanics--II. A continuum model of cartilage electrokinetics and correlation with experiments. *J Biomech* 20:629-39, 1987.
13. Gailani GB, Cowin SC: The unconfined compression of a poroelastic annular cylindrical disk. *Mech Mater* 40:507-23, 2008.
14. Gu WY, Yao H, Huang CY, Cheung HS: New insight into deformation-dependent hydraulic permeability of gels and cartilage, and dynamic behavior of agarose gels in confined compression. *J Biomech* 36:593-8, 2003.

15. Hong W, Zhao X, Zhou J, Suo Z: A theory of coupled diffusion and large deformation in polymeric gels. *J Mech Phys Solids* 56:1779-93, 2008.
16. Kameo Y, Adachi T, Hojo M: Fluid pressure response in poroelastic materials subjected to cyclic loading. *J Mech Phys Solids* 57:1815-27, 2009.
17. Kobayashi M, Oka M: Characterization of a polyvinyl alcohol-hydrogel artificial articular cartilage prepared by injection molding. *J Biomater Sci Polym Ed* 15:741-51, 2004.
18. Li LP, Cederbaum G, Schulgasser K: Theory of poroelastic plates with in-plane diffusion. *Int J Solids Struct* 34:4515-30, 1997.
19. Li LP, Cederbaum G, Schulgasser K: A finite element model for poroelastic beams with axial diffusion. *Comput Struct* 73:595-608, 1999.
20. Li LP, Schulgasser K, Cederbaum G: Theory of poroelastic beams with axial diffusion. *J Mech Phys Solids* 43:2023-42, 1995.
21. Maas SA, Ellis BJ, Ateshian GA, Weiss JA: FEBio: finite elements for biomechanics. *J Biomech Eng* 134:011005, 2012.
22. Mak AF, Lai WM, Mow VC: Biphasic indentation of articular cartilage--I. Theoretical analysis. *J Biomech* 20:703-14, 1987.
23. Melrose J, Chuang C, Whitelock J: Tissue engineering of cartilages using biomatrices. *J Chem Technol Biotechnol* 83:444-63, 2008.
24. Meng Q, Jin Z, Fisher J, Wilcox R: Comparison between FEBio and Abaqus for biphasic contact problems. *Proc Inst Mech Eng H* 227:1009-19, 2013.
25. Mow VC, Kuei SC, Lai WM, Armstrong CG: Biphasic creep and stress relaxation of articular cartilage in compression: theory and experiment. *J Biomech Eng* 102:73-84, 1980.
26. Noguchi T, Yamamuro T, Oka M, Kumar P, Kotoura Y, Hyon S, Ikada Y: Poly(vinyl alcohol) hydrogel as an artificial articular cartilage: evaluation of biocompatibility. *J Appl Biomater* 2:101-7, 1991.
27. Nowinski JL, Davis CF: The flexure and torsion of bones viewed as anisotropic poroelastic bodies. *Int J Eng Sci* 10:1063-79, 1972.
28. Scherer GW: Bending of gel beams: Method for characterizing elastic properties and permeability. *J Non-Cryst Solids* 142:18-35, 1992.
29. Scherer GW: Bending of gel beams: Effect of deflection rate and Hertzian indentation. *J Non-Cryst Solids* 201:1-25, 1996.

30. Scherer GW, Prévost JH, Wang ZH: Bending of a poroelastic beam with lateral diffusion. *Int J Solids Struct* 46:3451-62, 2009.
31. Selvadurai AP, Shirazi A: Mandel–Cryer effects in fluid inclusions in damage-susceptible poroelastic geologic media. *Comput Geotech* 31:285-300, 2004.
32. Shirazi R, Shirazi-Adl A: Computational biomechanics of articular cartilage of human knee joint: effect of osteochondral defects. *J Biomech* 42:2458-65, 2009.
33. Simon BR: Multiphase poroelastic finite element models for soft tissue structures. *Appl Mech Rev* 45:191-218, 1992.
34. Spiller KL, Maher SA, Lowman AM: Hydrogels for the repair of articular cartilage defects. *Tissue Eng Part B Rev* 17:281-99, 2011.
35. Stammen JA, Williams S, Ku DN, Guldborg RE: Mechanical properties of a novel PVA hydrogel in shear and unconfined compression. *Biomaterials* 22:799-806, 2001.
36. Taber LA: Axisymmetric deformation of poroelastic shells of revolution. *Int J Solids Struct* 29:3125-43, 1992.
37. Taber LA: A theory for transverse deflection of poroelastic plates. *J Appl Mech* 59:628-34, 1992.
38. Theodorakopoulos DD, Beskos DE: Flexural vibrations of poroelastic plates. *Acta Mechanica* 103:191-203, 1994.
39. Timoshenko S, Goodier N. *Theory of Elasticity*. 2nd ed. New York: McGraw Hill; 1951.
40. Torzilli PA, Grigiene R, Borrelli J, Jr., Helfet DL: Effect of impact load on articular cartilage: cell metabolism and viability, and matrix water content. *J Biomech Eng* 121:433-41, 1999.
41. Wang ZH, Prevost JH, Coussy O: Bending of fluid-saturated linear poroelastic beams with compressible constituents. *Int J Numer Anal Met Geomech* 33:425-47, 2009.
42. Williams GM, Gratz KR, Sah RL: Asymmetrical strain distributions and neutral axis location of cartilage in flexure. *J Biomech* 42:325-30, 2009.
43. Williams GM, Lin JW, Sah RL: Cartilage reshaping via in vitro mechanical loading. *Tissue Eng* 13:2903-11, 2007.
44. Wu JZ, Herzog W, Epstein M: Evaluation of the finite element software ABAQUS for biomechanical modelling of biphasic tissues. *J Biomech* 31:165-9, 1998.
45. Yang X, Wang C: A nonlinear mathematical model for large deflection of incompressible saturated poroelastic beams. *Appl Math Mech* 28:1587-95, 2007.

46. Yoon J, Cai S, Suo Z, Hayward RC: Poroelastic swelling kinetics of thin hydrogel layers: comparison of theory and experiment. *Soft Matter* 6:6004-12, 2010.
47. Zhang D, Cowin SC: Oscillatory bending of a poroelastic beam. *J Mech Phys Solids* 42:1575-99, 1994.

CHAPTER 5:

Conclusion

The overall objective of this dissertation was to understand the structural and biphasic response of articular cartilage and underlying bone at the synovial joint to the applied load or under cartilage degeneration developed by osteoarthritis or trauma.

To accomplish this, a variety of analytical and finite element methods, as well as novel image processing and statistical analyzes was used to acquire a multiscale view of the osteoarthritis synovial joint unit in 2D cross sections, and stress/strain field within cartilage subjected to different loading boundary conditions. In summary, these methodologies were:

(A) Development of advanced, automated methods of reducing 3-D imaging data of synovial joint sample into 2D cross-sections by using Digital Volumetric Imaging and assess the morphology of cartilage, ScP and interface structure in order to first: classify the canals according to the cap/uncap and the degree of penetration categories, second: evaluate coordinate and diameter of each open canal in NL and OA sample, and third: determine the spacing between open canals (Chapter 2).

(B) Development of a quantitative Finite Element Method (FEM) in order to analyze the effect of small, medium and large canal diameters as well as the small, medium and large spacing between canals on the biomechanics of articular cartilage (Chapter 3).

(C) Development a linear poroelastic analytical model in order to analyze bending a poroelastic sheet and mimic the mechanical behavior of articular cartilage under bending (Chapter 4)

The major findings related to the scientific objectives were:

1. According to the image processing done on 3D DVI data set:

- a. Canals embedded within ScP were classified based on capped/uncapped (C/O or G) and the degree of penetrations: not penetrating the cement line (N), penetrating the cement line (L), ending at tide mark (E) and penetrating tide mark (T). In total, from 12 categories, there were 2 non- realistic categories (ON and GN) and one OT category which was not found within the samples. The remained 9 classifications was simplified to two closed and open canals. From 6 NL samples, 16 ± 6 of the canals per mm^2 were closed, while only 2 ± 2 canals per mm^2 were open. Compared to the NL samples, in OA samples, 14 ± 7 canals per mm^2 were closed and 7 ± 4 canals per mm^2 were open. Thus, in OA joints, it is predicted that a higher number of the canals are open, ends at or penetrates through tidemark. These canals carry some cells and enzymes which may help trigger cartilage calcification and degeneration. Furthermore, a higher volume of solvent within cartilage may be carried out of cartilage which damages the solid matrix of cartilage.
- b. Coordinates of open canals for both NL and OA samples were specified as the center coordinates of the canals. In this study, only one vertical plane along with the horizontal plane was used in order to get the 3D coordinates of the canals.

However, using all three 2D cross-sectional images may help determine the canal coordinate in a more accurate way.

- c. Diameters of the open canals were determined for both NL and OA samples. Finally, three small, mean and large diameters were specified as critical diameters, by using statistical analyzes. In NL samples, the canal diameter was in the range of 27-46 μm (42-57 year-old samples) while in OA samples, it was 29-67 μm (54-78 year-old samples). It may be expected that in a range of younger synovial joint samples, the size of canal diameter decreases.
- d. The spacing between the open canals was determined for both NL and OA samples. Finally, three small, mean and large spaces were specified as critical spaces, by using statistical analyzes. In NL samples, the spacing between open canals was in the range of 359-809 μm , while in OA samples, it was 135-407 μm . It may be expected that in a range of younger synovial joint samples, the spacing between canals becomes even higher than 809 μm .
- e. With the increase of canal diameter and a decrease of the spacing between canals, it can be expected that cartilage may undergo early degeneration.

2. According to the ABAQUS simulation done on the synovial joint including open canals at the interface of cartilage and bone:

- a. With the increase of canal diameter and a decrease of the spacing between the canals, depressurization within cartilage occurs earlier. This depressurization is accompanied with the increase of stress and strain within cartilage, which may develop early cartilage degeneration.

- b. among five sets of diameter-spacing categories, in group 2(G2) in which the size of canal diameter was maximum (64 μm) and the spacing between the canals was minimum (128 μm), higher vertical fluid flux occurred along the entrance of the canal at the interface of the cartilage and bone. Higher fluid flux is resulted in carrying more solvent out of the cartilage which may develop cartilage degeneration over time.
- c. Cartilage degeneration and change in the cell metabolism may be a time-dependent procedure. Over time of loading, it was shown that stress and strain have fluctuation. Thus, we can not predict at what exact time, biomechanical effects of stress/strain within the cartilage is more significant.
- d. Each of biomechanical and biphasic fields could be as a quantity in order to analyze the cell apoptosis. Cell apoptosis may occur under a variety of geometry and loading boundary conditions. Although the boundary conditions of this study are not similar to the previous studies (**Table 3.1**), however, we can expect that in what range of stress, strain, and fluid pressure cells viability and metabolism are affected.

3. Under pure bending of poroelastic sheet:

- a. The poroelastic sheet is subjected to both stress relaxation and creep recovery. During stress relaxation, under constant curvature, there was a moment created within the sheet which was relaxed over time of loading. Once the curvature of the sheet was released, creep recovery occurred within the sheet and finally, the sheet got its original shape.

- b. During stress relaxation within cartilage, it was observed that axial strain is homogeneous within the sheet. However, other mechanical and biphasic fields were non-homogeneous.
- c. Spatial mechanical and biphasic responses to the pure bending were sinusoidal along the thickness of the sheet over stress relaxation and creep time showing an anti-symmetric pattern with respect to the neutral plane.